UNIVERSITY OF CALIFORNIA, MERCED

Experimental and Analytical Investigation of Transport Phenomena and Catalyst Layer Microstructure of Electrochemical Technologies

A dissertation submitted in partial satisfaction
of the requirements for the degree of

Doctor of Philosophy

in

Mechanical Engineering

by

Joy Marie R. Mora

Committee members:

Professor Po-Ya Abel Chuang, Advisor and Chair
Professor Min Hwan Lee
Professor Venkattraman Ayyaswamy
Professor James Palko

2024

This Ph.D. dissertation of Joy Marie R. Mora is approved, and it is acceptable in quality and form for any future publication on microfilm and electronically:

Po-Ya Abel Chuang, Advisor and Chair	Date
Min Hwan Lee	Date
Venkattraman Ayyaswamy	Date
James Palko	Date

University of California, Merced
2024

To my family and friends who have been my anchor and sail throughout the years.

ACKNOWLEDGMENT

I would like to express my deepest gratitude to my advisor, Prof. Abel Chuang. Professor, your mentorship, guidance, and unwavering support have been invaluable throughout my Ph.D. journey. Your wisdom has shaped my academic path in ways I cannot quantify, and I am truly grateful for your patience, support, and encouragement.

I am grateful to the CIPHER Program (IIID 2018-008) from the Commission on Higher Education – Philippine California Advanced Research Institutes (CHED-PCARI) of the Republic of the Philippines, and the Million Mile Fuel Cell Truck (M2FCT) consortium, funded by the Department of Energy (DoE), US, under contract No. DE-AC0205CH11231. Without the generous support from these funding institutions, this research would not have been possible.

A special thanks to my collaborators in the industry (Chemours and 1s1 Energy), national laboratories (NREL and LLNL), and academia (UP Diliman). Working with such brilliant minds has been a privilege, and your insights and contributions have enriched this research beyond measure. Your expertise and cooperation have been essential to the success of many projects.

I would also like to extend my heartfelt appreciation to the members of my dissertation committee, Prof. Min Hwan Lee, Prof. James Palko, and Prof. Venkatt Ayyaswamy. Your critical feedback, challenging questions, and encouragement pushed me to refine my work and strive for excellence. Your support has been vital to the completion of this dissertation.

To my labmates, both past and present, you have become my second family. I would like to express my gratitude to my former labmates, A. Rahman and S. Mehrazi, whose research laid the groundwork for this study. To my current labmates, thank you for your friendship, your readiness to share both knowledge and snacks, and for enduring my occasional bursts of nerdy enthusiasm. Special thanks to M. Sarker and Z. Najafianashrafi for their assistance with MEA testing of HOPI and rheo-EIS samples, and to N. Kakati and A. Karmakar for their help with MEA fabrication and characterization. The shared highs and lows, from late-night experiments to celebratory pizza parties, have made this journey truly unforgettable.

A huge thank you to my friends and family. Your unwavering support and belief in me kept me going when the going got tough. To my parents, thank you for instilling in me the values of hard work and perseverance. To my friends, thank you for pretending to understand my research and for being there to remind me that there's life outside the lab.

Finally, to anyone who has ever supported me with a kind word, a cup of coffee, or a much-needed laugh—thank you. Completing this dissertation has been a rollercoaster ride, and I couldn't have done it without each and every one of you. Here's to the next adventure, whatever that may be—hopefully with fewer sleepless nights and more celebrations.

CURRICULUM VITAE

Joy Marie Mora

Thermal and Electrochemical Energy Laboratory
University of California, Merced
jmora105@ucmerced.edu

EDUCATION

Ph.D. in Mechanical Engineering 2020 - 2024
University of California, Merced, CA, USA
Advisor: Po-Ya Abel Chuang, Ph.D.

M.S. in Energy Engineering 2011 - 2016
University of the Philippines - Diliman, QC, PH
Thesis: Heterogeneous Catalyst for Biodiesel Production from Soybean Oil

B.S. in Chemical Engineering 2005 - 2010
University of the Philippines - Diliman, QC, PH
Thesis: Ethanol Production from *Lemnaceae* using Enzymatic Hydrolysis

EMPLOYMENT HISTORY

MaCI Graduate Intern 05/2023 - 09/2023
Lawrence Livermore National Laboratory (LLNL)
Project: Designing GDEs for High Energy Efficiency CO_2 Electrolysis

Teaching & Graduate Research Assistant 01/2020 - 05/2024
University of California, Merced, CA, USA
Research: Fuel cells & Electrolyzer - Experiment and modeling & simulation studies
TA Courses: Thermodynamics, Heat & Mass Transfer, Fluid Mechanics, Fuel Cells & Batteries, Statics & Dynamics

Research Fellow & Specialist 06/2016 - 12/2019
University of the Philippines - Diliman, QC, PH
Research: PEMFC multiphysics simulation; OER systems; LNG projects

Process Development Engineer 01/2011 - 03/2014
Chiyoda Philippines Corporation, PH
Performed front-end engineering design, EPC work, and project coordination work for various LNG, refinery, and petrochemical plant projects

PUBLICATIONS & CONFERENCE PROCEEDINGS

1. **J.M. Mora** and P.A. Chuang, "Investigation and Characterization of Interfacial Transport Phenomena in the Catalyst Layer Using Rheo-Impedance Measurement," 245th ECS Meeting, San Francisco, USA, May 2024.

2. **J.M. Mora**, M.G. de Luna, et al. "Biodiesel production from soybean oil via LiOH-pumice catalytic transesterification and BBD-RSM optimization." Energy Reports 11 (2024): 4032-4043.

3. **J.M. Mora**, G. Li, and P.A. Chuang. "Ionomer-Dependent Oxygen Evolution Reaction in a Half-Cell and a Liquid Electrolyzer." Electrochemical Society Meeting Abstracts 244. No. 39. The Electrochemical Society, Inc., 2023.

4. **J.M. Mora**, M. Sarker, P.A. Chuang, et al. "Analytical-based simulation approach for an anion exchange membrane fuel cell." Energy Conversion and Management 273 (2022): 116382.

5. M. Castro, **J.M. Mora**, P.A. Chuang, et al. "A multiphysics model of a proton exchange membrane acid-alkaline electrolyzer." Energy Conversion and Management 267 (2022): 115829.

6. F. Mojica, M.A. Rahman, **J.M. Mora**, J. D. Ocon, and P. A. Chuang. "Experimental study of three channel designs with model comparison in a PEM fuel cell." Fuel Cells 20.5 (2020): 547-557.

7. R.M. Mendoza, **J.M. Mora**, R.B. Cervera, and P.A. Chuang. "Experimental and Analytical Study of an Anode-Supported Solid Oxide Electrolysis Cell." Chemical Engineering & Technology 43.12 (2020): 2350-2358.

8. **J.M. Mora**, F. Mojica, J.D. Ocon, and P.A. Chuang, "Effect of Different Flow Field Pattern on PEMFC Performance," European Fuel Cell Technology & Applications Piero Lunghi Conference & Exhibition, Naples, Italy, Dec. 2017.

9. M.A. Rahman, **J.M. Mora**, and P.A. Chuang. "A computational study of flow sensitivity of a PEM fuel cell with multi-parallel flow channels." COMSOL Conference in Boston. 2017.

10. **J.M. Mora**, J. Casero, M.L. Baynosa, and A.P. Rollon, "Enzymatic Hydrolysis of Starch from Duckweeds (Lemna SPP)," Philippine Engineering Journal. Vol. 32, No. 2, 13-18, Dec. 2011.

FELLOWSHIPS & AWARDS

Science of Scale-Up Strategic Initiative Award	Summer 2024
PBGA Professional Development Award	Spring 2024
GRAD-EXCEL Mentor Fellow	Fall 2023
Best Student Presentation, WFCC 2022, UC Irvine, CA	December 2022
SURETECH Summer Award	Summer 2022
Mech. Eng'g Graduate Student Summer Fellowship	Summers 2020, 2021, 2022
ERDT scholar, UP Diliman	2015 - 2016
University scholar, UP Diliman	2014 - 2015

AFFILIATIONS

Electrochemical Society (ECS) Member 05/2024 - present

Berkeley Lab Affiliate 10/2023 - 10/2024
National Center for Electron Microscopy, Molecular Foundry
Lawrence Berkeley National Laboratory (LBNL)

ESIF Lab Affiliate 05/2022 - 06/2022
Energy Systems Integration Facility
National Renewable Energy Laboratory (NREL)

ABSTRACT

Fuel cells, specifically Proton Exchange Membrane Fuel Cells (PEMFC) and Anion Exchange Membrane Fuel Cells (AEMFC), are pivotal in reducing greenhouse gas emissions and promoting clean, renewable energy. These technologies are critical for the protection and sustainability of the planet's resources. Despite their distinct applications, PEMFC and AEMFC devices share many similarities in terms of their components and the underlying physics that govern their operation. This commonality allows research findings from one type of fuel cell to be adapted to the other with minimal modifications.

Like PEMFCs, AEMFCs are characterized by their complex nature and the highly coupled multiphysics involved in their operation. This complexity makes it challenging to draw comparisons and conclusions from various experimental studies. Additionally, local conditions and transport phenomena within the fuel cell are difficult to probe experimentally. In this context, modeling serves as a powerful tool that complements experimental studies, offering clear and direct relationships between operating parameters, material properties, and overall performance. In the work discussed in Chapter 3, a one-dimensional (1-D) analytical model of an AEMFC has been developed. This model is capable of simulating the fuel cell's performance under both dry and wet conditions. The modeling approach for handling flooding in the gas diffusion media and the catalyst layer involves a combination of semi-empirical models and multilayer discretization of domains. This robust approach can be extended to other cell models as well.

At the heart of both PEMFC and AEMFC devices are the electrodes or catalyst layers (CLs). These are complex, heterogeneous porous structures made up of catalyst particles, ion-conducting polymers, and void spaces. These components come together to form the triple phase boundary, which is essential for the electrochemical reactions that occur within the fuel cell. Specifically, Pt/C particles facilitate electron transport, ion-conducting polymers enable ion conduction, and void spaces are crucial for the transport of gases and water. Catalyst inks are typically used to fabricate these catalyst layers. Therefore, understanding how various parameters of the catalyst ink (e.g., ionomer chemistry and loading, solvent formulation, carbon support type, etc.) affect its properties, the interactions between the components, and ultimately the formation of the CL microstructure and cell performance, is vital for optimizing electrode design.

The studies described in Chapters 4 to 6 use a combination of rheological and electrical measurements in addition to established characterization tools to investigate the effects of catalyst ink parameters and shear on the properties of the ink. The simultaneous measurements of rheology and impedance will provide unique insights into the evolution of the microstructure of the catalyst layers. The proposed rheo-EIS measurement tool takes advantage of the dynamic nature of catalyst inks, where rheological and electrical behaviors are coupled to the material's microstructure. These coupled behaviors are typically difficult to measure using traditional optical or scattering techniques. This tool will be used to study catalyst inks for PEMFC applications, providing detailed insights into their microstructural development and resulting electrode performance.

TABLE OF CONTENTS

LIST OF FIGURES

LIST OF TABLES

LIST OF SYMBOLS

The list describes the mathematical symbols that have been used in this dissertation.

Chapter 1

INTRODUCTION

1.1 Background and Motivation

The Paris Agreement, which set the threshold for 'safe' global average temperature at 1.5°C to 2°C above pre-industrial levels, was adopted at a time when climate projections for this century could only be described as catastrophic. Most scientists argued that with the 'business as usual' approach, the planet could warm by 4°C or even 5°C. Such events would lead to food and water crises, significant heat stress, economic conflicts, displacement of populations, and, in some areas, warnings about the end of civilization [1].

At present, climate change has led to roughly 1.2°C of warming [1]. In order to meet the climate goals articulated in the Paris Agreement, governments need to take rapid action to curb emissions and completely transform how societies consume and produce energy. The solution includes advancing the transition to renewable energy technologies, developing sustainable transportation systems, and an overall reduction in carbon emissions across all sectors. Currently, about 80% of the world's energy is produced using fossil fuels [2, 3]. To limit the temperature rise to within 'safe' levels, this percentage would have to fall all the way to zero in the next five decades - if not faster. Fuel cell technology represents a crucial component and a promising solution towards achieving the 1.5°C target.

Nations around the world are implementing policies towards achieving the 1.5°C target. These initiatives include China's green deal that strives to peak carbon emissions in 2030 and achieve carbon neutrality by 2060 [4] and the European Green Deal (EGD) that targets carbon neutrality for Europe by 2050 [5]. In 2022, the US Senate passed legislation, which includes the largest single American investment in history to slow down global warming [6]. The bill provides billions of dollars of investments in the development of clean energy technologies that could help reach the goal of cutting global warming emissions in half by 2030 [7]. In line with this mission, researchers and energy developers deem building sustainable and green energy technologies and infrastructure as critical in the current era, where climate change and energy security are primary concerns. To this end, focus is given to energy-conversion devices that not only curtail greenhouse gas emissions but also use

renewable energy sources and produce value-added products. Among the different energy conversion and storage devices, fuel cells are one of the most attractive and promising technologies.

The United States is at the forefront of developing fuel cell technology, with several projects underway. For example, in California, efforts are being made to expand hydrogen fueling stations and promote hydrogen fuel cell electric vehicles (FCEVs) in order to achieve a carbon-neutral economy by 2045. In line with this goal, California has recently launched ARCHES, a public-private partnership that aims to fund and build hydrogen hubs across the state [8]. Another prominent project in the U.S. funded by the Department of Energy (DOE) is the Million Mile Fuel Cell Truck (M^2FCT) research consortium that aims to develop a hydrogen fuel cell system that can power a heavy-duty truck for 1 million miles of operation [9].

1.1.1 PEM and AEM Fuel Cell Operation

Fuel cells are electrochemical devices that convert chemical energy from fuel, typically hydrogen, directly into electricity. From all fuel cell types, proton exchange membrane fuel cells (PEMFCs) have been studied extensively for the last few decades due to their zero/low emission, high energy density, fast start-up, and outstanding stability and durability [10–12]. In PEMFC, hydrogen and air are fed through the gas flow channels. These reactant gases are distributed throughout the cross-sectional area of the cell and transported further into the cell through gas diffusion layers (GDLs). After the GDL, gases enter the catalyst layers (CLs) or electrodes where reactions take place. At anode CL, hydrogen is oxidized to generate protons and electrons. At cathode CL, oxygen from the air reacts with protons and electrons to form water.

Anion exchange membrane fuel cell (AEMFC) has the same operating principle as PEMFC. The key difference is that AEMFC uses an anion-conducting membrane which allows for operation under alkaline environment. Fuel cells operated under alkaline environments have significantly improved oxygen reduction reaction (ORR) kinetics [13]. Aside from superior ORR kinetics, advantages of an AEMFC include the use of low-cost, non-precious catalysts, no CO poisoning of electrocatalyst when operating at low temperatures [13], low fuel crossover [14, 15], and potentially low cost of membrane material compared to PEMFC [16].

Even though an AEMFC differs from a PEMFC, they share many similar materials and designs. For instance, transport properties of different channel designs for PEMFC is applicable to AEMFC [11]. The requirement and specifications of the diffusion media materials and properties are also similar [17] as well as the analytical multiphysics simulation approach [18, 19]. A schematic illustration of AEMFC and PEMFC operation is illustrated in Figure 1.1.

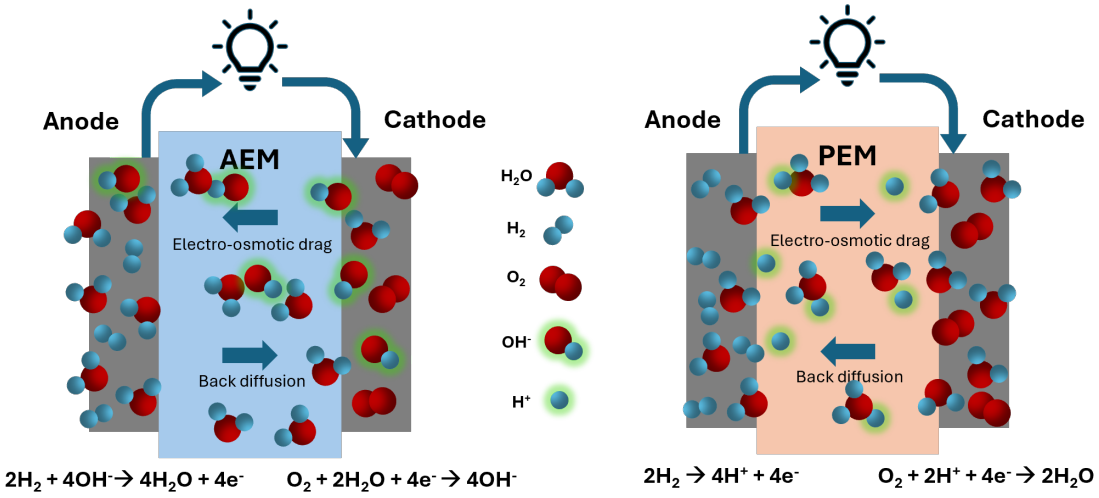

Figure 1.1: Schematic diagram showing AEMFC and PEMFC operation and electrode reactions. Adapted from Ref. [20]

1.1.2 Technological Challenges and Current State of Research

1.1.2.1 PEMFC Technology

PEMFC is a relatively mature technology compared to AEMFC. However, performance limitations still arise due to its sluggish ORR kinetics, high mass transport loss, and CO poisoning of Pt-based catalysts [21–23]. To date, there are extensive studies and published research related to enhancing the ORR kinetics of PEMFCs [24].

In the U.S., the research and development related to PEMFC technology primarily focus on improving efficiency and durability for long-term operation. This effort is supported by numerous initiatives and funding opportunities, such as the U.S. DOE-funded M^2FCT consortium. To this end, there are systematic studies on how structures of electrodes or CLs affect the performance and long-term durability of PEMFCs [25, 26]. In addition, several studies have also been published discussing degradation mechanisms of the membrane, GDL, and electrode component through accelerated stress tests [27, 28]. Development of fuel cell components and integration have also been proposed geared toward fuel-cell electric vehicle applications [29].

1.1.2.2 AEMFC Technology

While there are benefits of AEMFC technology such as faster ORR and fuel flexibility, it suffers from slow hydrogen oxidation reaction (HOR) kinetics, complicated water management, and lower intrinsic conductivity for hydroxide compared

to proton transport [30, 31]. In addition, low concentration of CO_2 in the air can react with hydroxide ions to form bicarbonate and carbonate ions causing the reduction of hydroxide conductivity [32].

Currently, the research and development of AEMFCs are still in its early stages and most studies are experimental and material-driven. Numerous work focused on membrane synthesis and characterization [33, 34], development and design of non-Pt catalyst [35, 36], and analysis of cell performance [37, 38]. In addition to material development, AEMFC operation involves complicated water transport due to its intrinsic imbalance in the cell. In an AEMFC, water is generated at the anode and consumed at the cathode, which often causes a significant water gradient through the membrane. As a result, AEMFC often suffers from anode flooding and cathode drying, which is exacerbated at high current densities [39]. Therefore, a new fundamental understanding of water transport as a function of various operating conditions, materials properties and catalyst design need to be established. Considering the complexity and difficulty of experimental study, modeling is viewed to be a more effective and low-cost approach to gain a deep insight into the water transport and performance of an AEMFC [40].

1.2 Fuel Cell Modeling and Simulation

Experimentally probing the multiphysics processes and phenomena in an electrochemical device, such as fuel cells, while in operation is challenging. Spatial variations in species distribution, local conditions like pressure and temperature, and current densities are nearly impossible to observe with currently available experimental tools. For this reason, simulation and modeling tools have proven to be an invaluable complement to experimental investigations and a crucial resource for designers and decision-makers. Modeling can provide insights into the effects of component design and material properties on performance, aiding in the optimization of design and operating conditions. This ultimately leads to increased efficiency and reduced overall costs.

Modeling approaches can be classified in various ways: in terms of spatial dimensions of domain considered (0-D, 1-D, 2-D, or 3-D), single-phase or multiphase, physics included, isothermal or non-isothermal, numerical or analytical, static or dynamic, and so on. A map illustrating the scope of electrochemical modeling is presented in Figure 1.2.

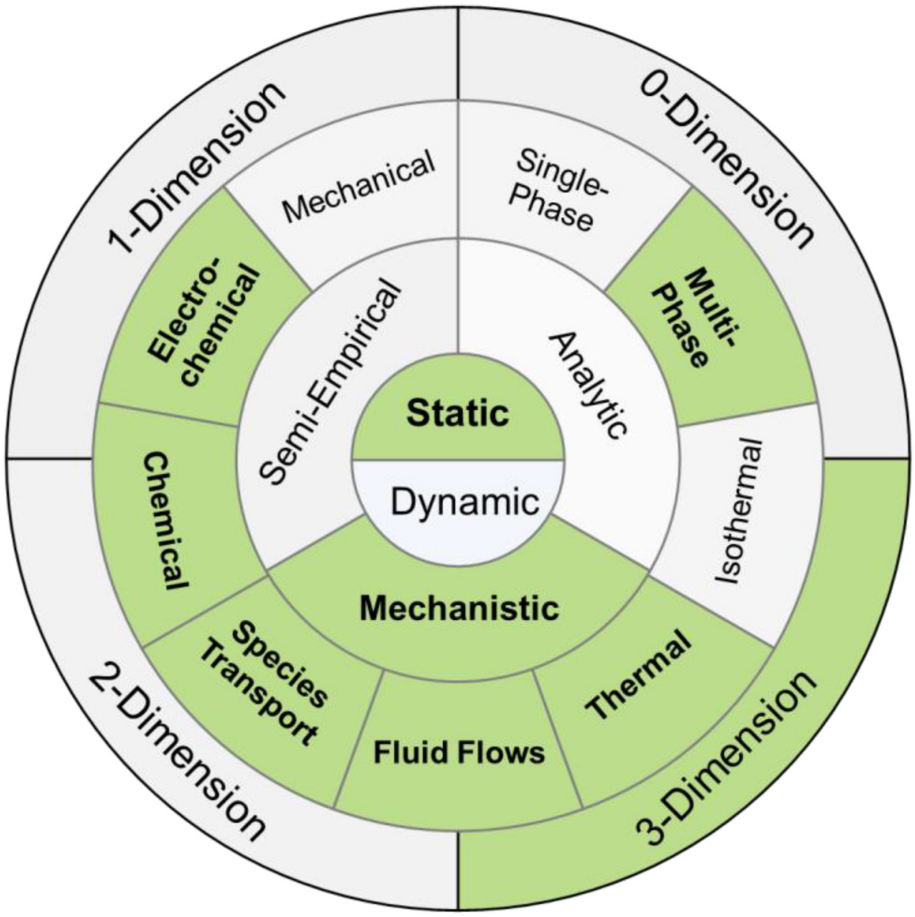

Figure 1.2: Different types of modeling scope and scale applicable for fuel cell simulation studies [41].

Several modeling studies related to PEMFC and AEMFC have been published to date. These types of studies span optimization of CL design [25, 42], understanding of water transport [43], investigating degradation mechanisms [44], performance modeling and parameter sensitivity studies [18], and so on.

1.3 Catalyst Layer and Ink Multicomponent Interaction

The catalyst layer (CL) is vital as the site where electrochemical reactions take place, making it a crucial component of any electrochemical cell. In PEMFCs, the CL features a heterogeneous porous electrode composed of platinum (Pt) catalyst particles supported on carbon, embedded within an ionomer matrix, and interspersed with void spaces defining the triple-phase boundary (TPB). The solid

phase acts as an electron conductor, the ionomer functions as a binder and facilitates ion transport, and the gas-phase voids serve as channels for species transport. Optimizing the microstructure of the CL to enhance TPB density is essential for maximizing catalyst utilization and improving overall cell performance.

CL is usually prepared using catalyst ink, which consists of Pt catalyst on carbon material, ionomer dispersion, and a solvent mixture of alcohol and water. The microstructure of the CL is dependent on several factors including ink formulation, carbon support, ionomer chemistry, solvent ratio, fabrication technique, and many others [45]. In addition, catalyst ink interactions play an important role in determining electrochemical properties, such as double layer capacitance (DLC), charge-transfer resistance, and electrochemical surface area (ECSA) as shown by previous studies on proton exchange membrane fuel cells (PEMFC) [46, 47]. Figure 1.3 illustrates the ink properties and catalyst layer structure and associated parameters that determine final electrode microstructure.

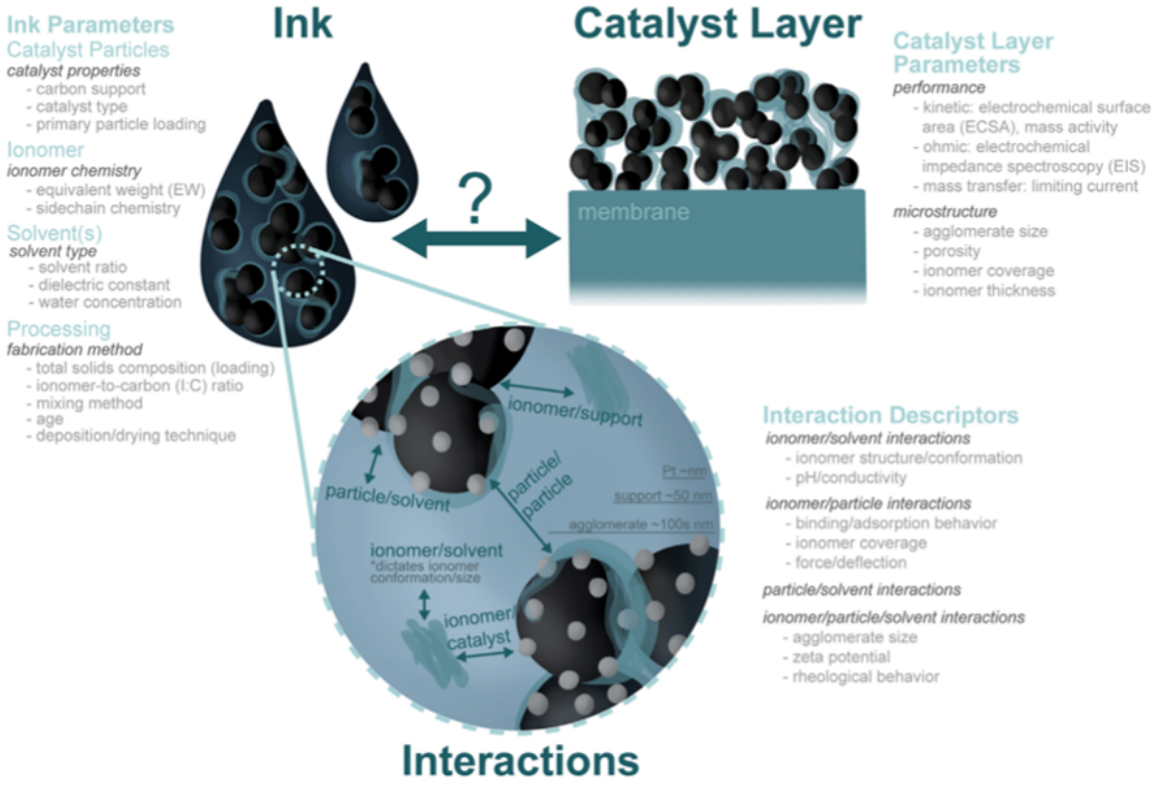

Figure 1.3: Illustration of the catalyst ink and catalyst layer and the relevant parameters that determine CL microstructure [45].

Understanding how catalyst ink parameters influence ink properties and the

interactions among its components is crucial for comprehending their impact on CL microstructure formation and overall cell performance. This knowledge is essential for designing electrodes as it provides guidance on achieving specific CL microstructures without relying solely on time-consuming optimization and empirical studies.

1.4 Research Objectives and Dissertation Outline

This dissertation integrates both modeling and experimental approaches to investigate transport phenomena and the microstructure of electrode components in fuel cells. The modeling and simulation work aims to develop a one-dimensional (1-D) analytical model of an anion exchange membrane fuel cell (AEMFC), while the experimental work focuses on investigating the impact of catalyst ink properties on catalyst layer (CL) microstructure and membrane electrode assembly (MEA) performance.

Chapter 2 provides a review of the current literature. This includes topics on AEMFC modeling and catalyst ink parameter study. Subjects related to catalyst ink study comprise the different experimental tools and methods used to characterize ink properties.

Chapter 3 delves into the development of a 1-D analytical model for AEMFCs. This chapter outlines the model's formulation, detailing the electrochemical, kinetic, and transport equations, along with the coupled physics incorporated into the model. It also presents the experimental validation of the model. Furthermore, the chapter introduces an empirically-based local flooding model designed to simulate cell performance under flooding conditions.

Chapter 4 introduces the rheo-impedance tool for studying catalyst ink microstructure. This chapter explains the theory and working principle underlying rheo-impedance measurement. It also details the developed protocols for standard rheology and simultaneous rheo-impedance tests. Furthermore, the chapter explores the application of this tool to platinum on carbon (Pt/C) catalyst inks with various types of carbon supports and solvent formulations.

Chapter 5 further explores the application of rheo-impedance measurements in investigating catalyst ink microstructure, specifically examining the impact of different ionomer chemistries on catalyst ink and electrode properties. Additionally, this chapter investigates the influence of carbon loading on the rheology of the ink. The insights gained from the rheo-impedance tool are complemented by zeta-potential and dynamic light scattering (DLS) measurements, providing a comprehensive understanding of the evolution of CL microstructure and its effect on cell performance.

Chapter 6 builds upon the findings from Chapters 4 and 5 by examining how ionomer loading and solvent formulation impact the properties of catalyst inks, the resulting CL microstructure, and ultimately, cell performance. This study comprehensively explores the multicomponent interactions within catalyst inks by evaluating formulations at three different levels for each parameter. The chapter offers a detailed insight into the formation of CL microstructure and its interplay with catalyst ink properties.

Finally, Chapter 7 summarizes the dissertation and outlines the main findings from the work. In addition, it gives directions an identifies avenues for future work.

Chapter 2

LITERATURE REVIEW

2.1 AEMFC Modeling

In recent years, there have been a few modeling studies pertaining to hydrogen-fueled AEMFC and most of them are numerical in nature [14, 30, 48–51]. Shiau et al. [30] developed a steady-state model to investigate the effect of humidification on cell performance and found that anode inlet relative humidity (RH) is particularly critical given a membrane having low water-transport resistance. Dekel et al. [14] developed a model that explored the impact of varying RH and time-dependent cell performance. A subsequent study from the same group examined the influence of anion-exchange ionomer (AEI) on performance and stability, revealing that ionomer conductivity significantly affects long-term stability [52]. Additionally, Yassin et al. [53] studied the effect of AEM thickness on performance and found that reduced thickness markedly improves performance by minimizing anode flooding and cathode dehydration. While these 2-D and 3-D computational models give insights into the local distribution in a fuel cell, they usually have non-physical-based adjusting factors, require high computational power, and are very sensitive to grid structure, input values, and boundary conditions. Some of the key advantages and disadvantages of analytical and numerical modeling approach are listed in Table 2.1.

Table 2.1: Comparison of Analytical vs. Numerical/Computational Models for Fuel Cell Analysis

MODEL TYPE	**PROs**	**CONs**
Analytical Model	Simplicity Speed Insight Benchmarking	Limitations Applicability
Computational/Numerical Model	Detail Accuracy Scalability Flexibility	Complexity Computationally-intensive Stability and convergence Cost

Analytical-based physical models have been recognized as an effective tool for water management of fuel cells [18, 54, 55]. If implemented appropriately, the analytical model can provide direct and clear relations between the results and model parameters. However, only a few studies have used this approach in AEMFC study and none of them fully capture all important multiphysics [56, 57]. Huo et al. [40] developed a steady-state, isothermal model that explored water transport and revealed that water permeation from anode to cathode is the critical factor affecting cell performance. A previous analytical model from the same research group was developed to examine the effect of the MPL and the electrode wettability on water transport [56]. For the analytical model to be accurate, all the pertinent physics must be included. The fundamental physics in an AEMFC include (1) electrochemical reaction kinetics, (2) membrane water and ion transports, (3) non-isothermal heat transfer with multiple location-specific heat sources, (4) electron transport with electrical contact resistances, (5) mass transport with geometrical effect, and (6) two-phase water transport phenomena.

2.2 Catalyst Ink Parameters

Studies have shown that the composition or formulation of catalyst ink greatly impacts CL microstructure [45, 58–61]. Depending on the composition, type of ionomer, solvent formulation, and various other factors in the catalyst ink, different interactions can lead to diverse CL microstructures. The following subsections will discuss the ink parameters in detail and explain how each parameter influences the macroscopic properties and microstructure of the ink.

2.2.1 Ionomer Chemistry and Loading

The ionomer is a crucial component in catalyst inks. It not only binds the catalyst particles together but also provides pathways for proton conduction and helps promote TPB sites. The most extensively studied ionomer in relation to PEMFCs is perfluorosulfonic acid (PFSA). PFSA ionomers feature a polytetrafluoroethylene (PTFE) backbone with side chains terminating in negatively charged sulfonic acid functional groups. The properties of PFSA ionomers can be modified by altering the backbone structure, side chain length, or equivalent weight (EW), which is measured in terms of grams of ionomer per mole of sulfonic acid group. These properties affect the microstructure of the ink by impacting the interaction with the catalyst particle or solvent.

Recent studies have demonstrated performance improvements using highly oxygen-permeable ionomers (HOPIs). [62–64]. Unlike the straight PTFE chain of

Nafion ionomers, HOPIs possess an oxygen-permeable ring matrix backbone facilitating gas transport. Studies have shown that using HOPIs reduced the oxygen transport resistance in the CL and increased the power density of the MEA. Jinnouchi et al. [62] studied the effect of adding a ring-structured backbone matrix, perfluoro-(2,2-dimethyl-1,3-dioxole), into ionomers and found that oxygen solubility of the ionomer improved and catalyst poisoning due to sulfonic acid group minimized. The molecular structures of Nafion and two different HOPI materials are shown in Figure 2.1. To optimize the design of CL, a deeper understanding of how these relatively new ionomers influence the interfacial structure is essential. In the case of HOPI, the permeability is informed by several parameters such as interfacial properties and ionomer distribution in the CL [62].

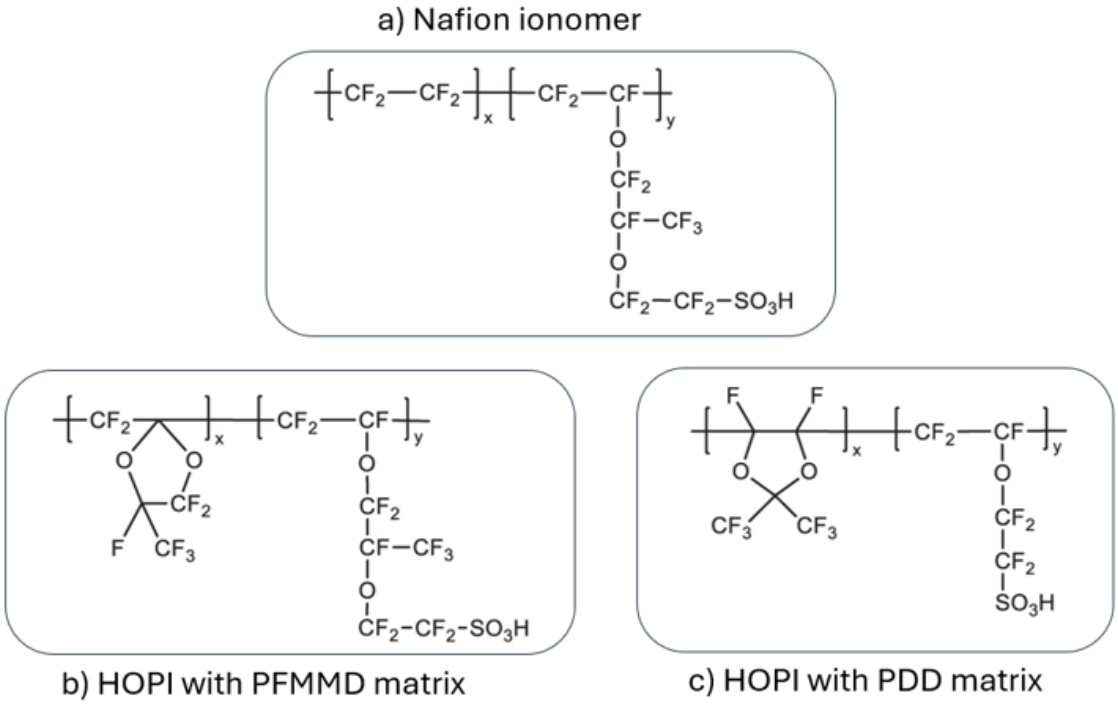

Figure 2.1: Molecular structure of (a) Nafion ionomer, (b) HOPI with PMFMMD backbone, and (c) HOPI with PDD backbone. Adapted from Ref. [62]

Furthermore, ionomer loading, commonly referred to as the ionomer-to-carbon (I/C) ratio, plays a crucial role in the performance and durability of PEMFCs. This ratio is generally optimized to increase Pt catalyst utilization and minimize mass transport resistance. The I/C ratio provides a measure of continuous ionic pathways for effective proton transport across the CL. At high I/C levels, an excess of ionomer can lead to catalyst agglomeration, reducing the electrical conductivity of the CL. It has also been reported that ionomer adsorption on carbon follows a Langmuir

isotherm [65], meaning the ionomer adsorbs as a monolayer. Therefore, above an optimal I/C ratio, increasing ionomer loading barely increases the adsorbed ionomer, while the nonadsorbed ionomer contributes to polymer bridging. If the I/C ratio is too high, the pores of the CL become blocked, hindering species transport and resulting in increased local and bulk gas transport resistance and/or flooding. Conversely, at very low I/C ratios, there is insufficient ionomer to form a network for proton transport, reducing the number of accessible Pt catalytic sites or TPB.

2.2.2 Solvent Formulation

The type of solvent and formulation used in catalyst inks are important. Although the solvent completely evaporates and is not present in the CL final form, its properties (i.e., dielectric constant, solubility parameter, viscosity, surface tension, boiling point, and surface tension) inform the microstructure and the macroscopic properties of the ink and therefore the final CL microstructure [59, 66, 67]. Figure 2.2(a) lists these properties and the corresponding catalyst ink macroscopic properties they influence.

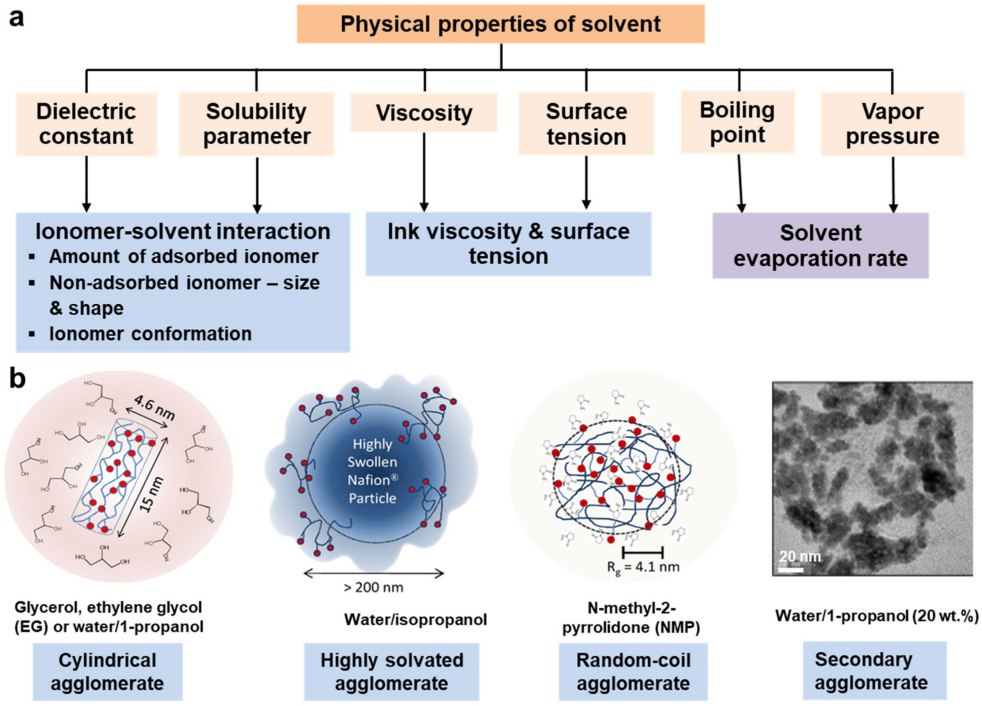

Figure 2.2: (a) Physical properties of solvent and their effects on the microstructure and macroscopic properties of catalyst ink, (b) size and morphology of Nafion ionomer in different solvents [61]

The dielectric constant of a solvent refers to its ability to separate opposing charges and is related to its polarity. Similarly, the solubility parameter measures the interaction behavior of an ionomer in a given solvent and is directly related to the degree of ionomer conformation [68]. Both the dielectric constant and the solubility parameter primarily influence the dispersion of the catalyst and the conformation of the ionomer.

The solvent viscosity affects the viscosity and stability of the catalyst ink. It also impacts the ink coating and drying processes. Catalyst ink with a viscous solvent is generally more stable than ink made with a thin solvent, as the Brownian motion of agglomerates is typically reduced [61]. Additionally, catalyst ink for rod coating is relatively more viscous than ink for spray coating.

The boiling point and vapor pressure of the solvent influence the choice of coating and drying process. A higher boiling point results in a slower evaporation rate, which increases ink stability during the drying process by prolonging the drying time. In contrast, fast evaporation can make the ink unstable and may contribute to CL surface cracking [61] upon drying. Therefore, it is important to select a solvent that ensures the resulting ink is stable enough while also allowing for complete evaporation of the solvent during the drying process.

Finally, the surface tension of the solvent affects the surface tension of the ink to some degree with contributions from catalyst and ionomer [61].

2.2.3 Type of Carbon Support and Loading

In this study, catalyst refers to platinum supported on carbon (Pt/C). The structure and surface properties of the catalyst, in particular the carbon, and the catalyst loading, which is informed by the carbon-to-solvent (C/S) ratio parameter in catalyst ink greatly influence the microstructure and macroscopic properties of the ink. These include the size of catalyst agglomerates, ionomer coverage, ink viscosity, and optimal I/C.

In general, carbon supports are classified into low surface area (e.g., Vulcan carbon black) and high surface area carbon (e.g., Ketjen carbon black). A previous study presented a comparison of the BET-surface area of different carbon [69]. This is shown in Figure 2.3.

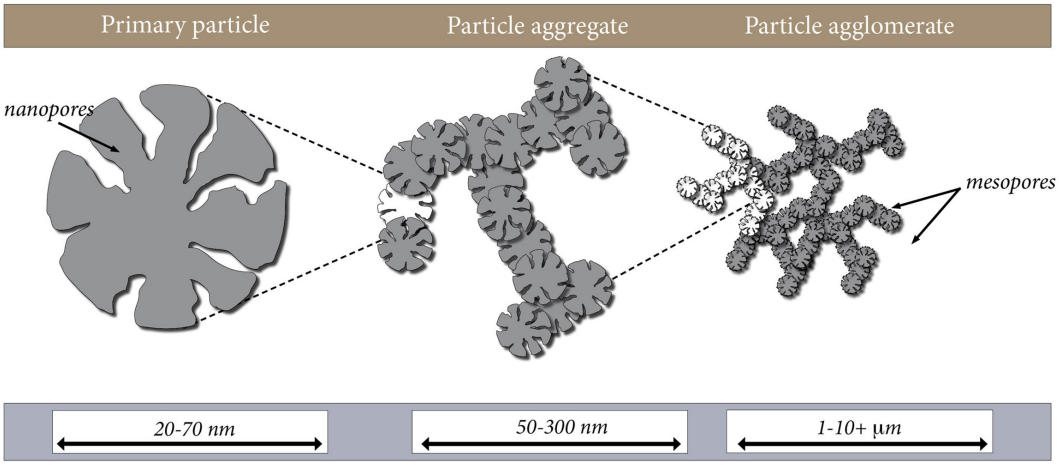

	BET total surface area, m^2g^{-1}	Micropore surface area < 2 nm, m^2g^{-1}	External surface area > 2 nm, m^2g^{-1}
Ketjenblack EC-600JD	1448.7	278.6	1170.1
Ketjenblack EC-300J	775.6	359.6	416.0
Vulcan XC72R	224	68	154

Figure 2.3: Schematic sketch of the carbon structure and their experimentally determined BET-surface area properties [69]

According to the literature, Ketjen carbon black has a significant surface area and is highly porous. Consequently, most of the Pt nanoparticles reside in the internal pores, with only about 50% or fewer on the external surface. Additionally, ionomer preferentially interacts with Pt rather than carbon. As a result, Pt/Vulcan has a higher Pt surface density, leading to more uniform ionomer coverage [61].

Additionally, if the catalyst content in the ink is increased, the amount and size of agglomerates increase, and the distance between agglomerates decreases, increasing the viscosity of ink [70]. In PEMFC, the catalyst content is normally related to the amount of carbon in the ink and controlled by the carbon-to-solvent (C/S) ratio parameter in ink preparation.

2.3 Catalyst Ink Macroscopic Properties and Microstructure

The heart of an electrochemical cell is the catalyst layer (CL). As previously discussed, CLs are typically fabricated from inks composed of a mixture of ionomer, catalyst particles, and solvent. The intrinsic properties of each material and the resulting interactions between these components make characterizing ink microstructure inherently complex.

2.3.1 Catalyst Ink Component Interaction

The composition and type of ionomer or solvent in the catalyst ink lead to different interactions and, consequently, different microstructures. Ionomer/solvent interactions inform the conformation of ionomer in a solution which in turn affects the formation of TPBs. For instance, the ionomer (Nafion) can present as an agglomerated structure in an IPA-rich solvent or as a rod-like structure in a water-rich solvent [71]. This is illustrated in Figure 2.4(a-b). This variation in ionomer behavior affects the interactions between catalyst particles, influenced by the resulting surface energies due to the adsorbed ionomers on the surface as shown in Figure 2.4(c-d).

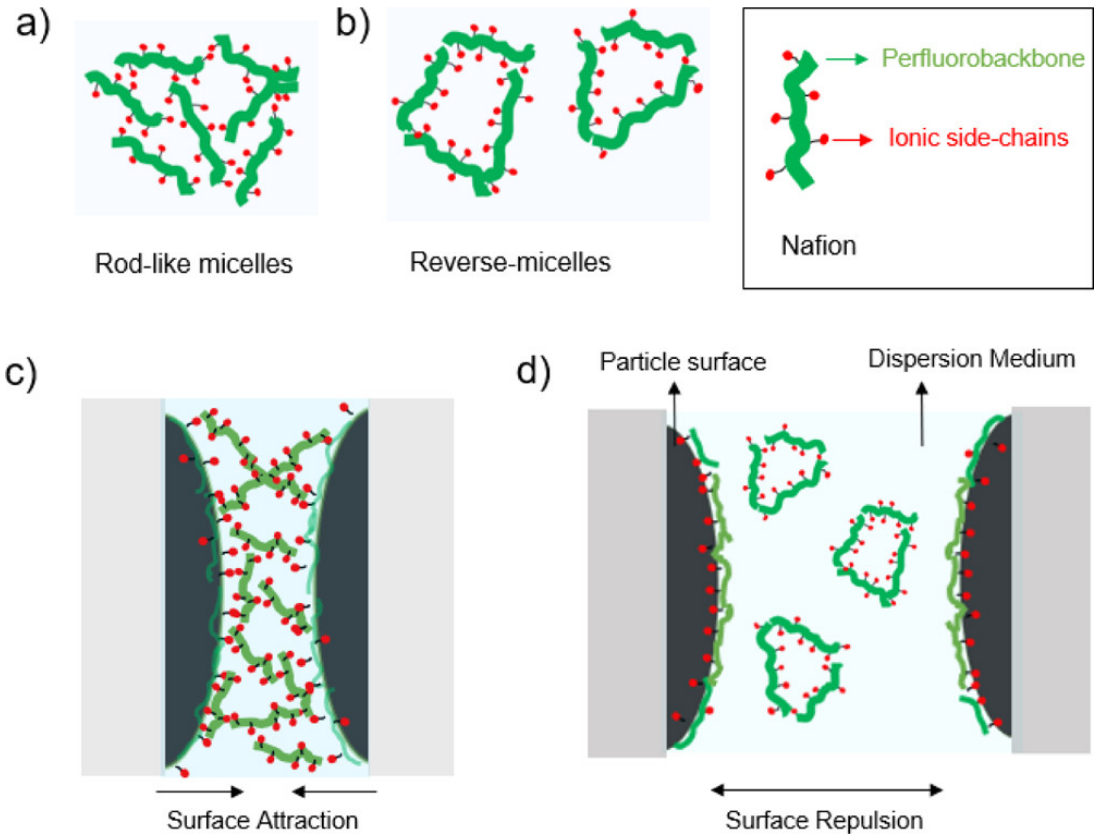

Figure 2.4: Structure of ionomer under different solvent: (a) and (c) water-rich; (b) and (d) nPA-rich catalyst inks [71].

The ionomer/particle interactions govern the agglomeration behavior and the size and distribution of agglomerates. Researchers have shown that ionomer distribution and coverage on catalyst particles directly influence the electrochemically active surface area (ECSA) and influence the mass transport resistance [68, 72].

Particle/solvent interaction also determines the degree of agglomeration in the ink. When the interfacial energy between catalyst particles and solvent is high, in the absence of ionomer, it leads to greater agglomeration. This occurs because the particles tend to cluster together to minimize the interfacial energy. The presence of ionomer can significantly reduce this interfacial energy, thereby decreasing the extent of agglomeration and promoting a more uniform dispersion of catalyst particles within the solvent [68]. Altering the solvent formulation, such as adjusting the IPA-to-water ratio, directly impacts the dielectric constant and solubility, thereby affecting the hydrophobicity of the system and potentially inducing aggregation [45]. This adjustment can lead to changes in how catalyst particles interact with each other and with the ionomer, influencing the ink's macroscopic property and microstructure.

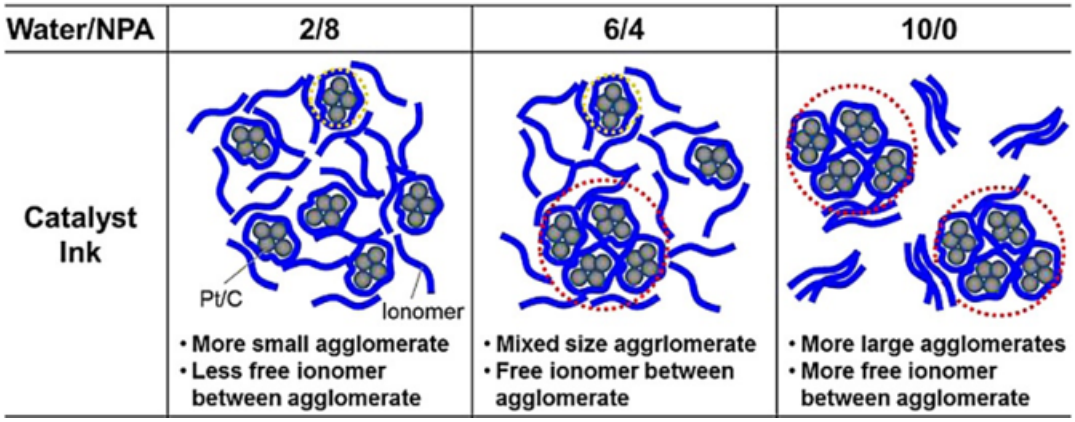

Figure 2.5: Proposed catalyst microstructure based on water/NPA ratios [73].

2.3.2 Techniques for Characterizing Catalyst Ink

To establish a clear material-performance relationship, it is crucial to analyze several key factors. These include the morphological structure of the CL, the size and distribution of particles and formed agglomerates, the interactions between different components, the stability of the ink, and the characteristics of the final coating. For instance, the morphological structure can significantly influence the electrochemical surface area and, consequently, the overall performance of the cell. Particle size and distribution affect the efficiency of catalytic reactions, while component interactions can impact the overall stability and durability of the electrode. Additionally, ink stability is vital for ensuring consistent application and performance, and coating characteristics such as thickness and uniformity are critical for optimizing the cell's performance. Figure 2.6 represents the evolution of catalyst ink to catalyst layer and its relationship to MEA performance.

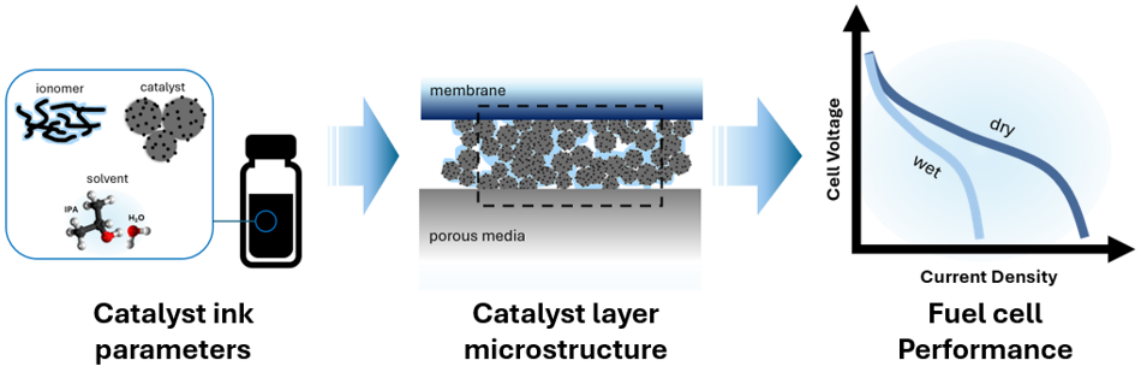

Figure 2.6: Schematic showing the progression of catalyst ink to catalyst layer and into its effect on fuel cell performance.

It is essential to develop a systematic understanding of how electrode structure, properties and performance are affected by catalyst ink component interaction. Such knowledge would also help in validating any proposed structure-property relationships that could be key in understanding stability and performance of electrodes.

2.3.2.1 Dynamic Light Scattering (DLS)

Dynamic light scattering (DLS) is a convenient, fast, and non-destructive technique for characterizing ink properties. It evaluates ink stability by measuring particle size distribution, which indicates the extent of catalyst agglomeration and the formation of ionomer aggregates. The technique captures the Brownian motion of particles in solution, analyzing the scattered light signal received by the detector. The particle (hydrodynamic) size is calculated using the Stoke-Einstein equation, which depends on the overall viscosity and refractive index of the solvent and the temperature of the sample [66]. In addition, polydispersity is calculated from DLS data as the standard deviation of the size distribution of particles in a dispersion. The polydispersity index (PDI) provides a quantitative representation of the extent of particle size distribution. Values between 0.1 and 0.4 indicate moderate to high dispersity, while PDI > 0.1 suggests significant polydispersity. A PDI < 0.1 indicates a highly monodisperse sample [68].

DLS measurement is suitable for the characterization of colloidal particles from a few nanometers to a few microns. However, since multiple scattering greatly affects the quality and accuracy of data, measurement requires dilution of inks. This, in turn, prevents the measurement of the true ink structure [74].

2.3.2.2 Zeta Potential

The interaction between charged particles can be quantified to a certain degree by measuring zeta potential (ζ). Zeta potential is an important parameter that provides a measure of the stability of colloidal dispersions, such as catalyst inks. It represents the degree of repulsion between adjacent, similarly charged particles in ink dispersions and is also closely related to particle size [74]. In particular, high zeta potential values (positive or negative) indicate strong repulsion and thus greater stability, while low zeta potential values suggest a tendency for particles to aggregate.

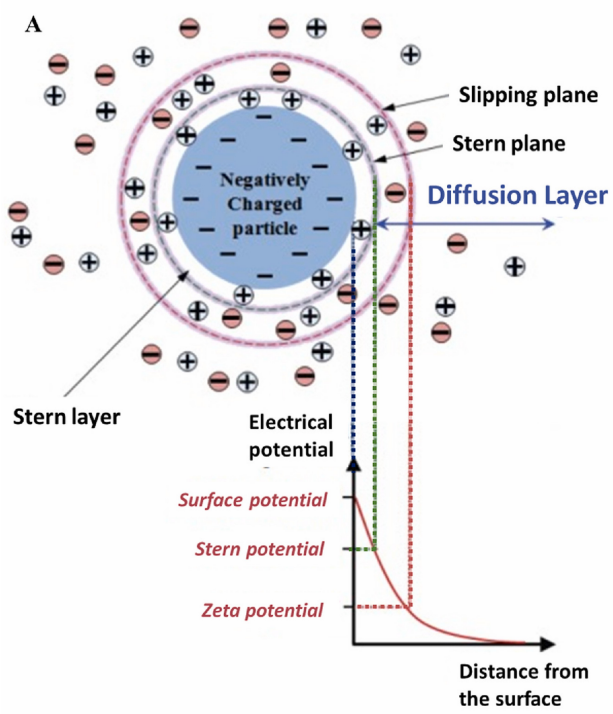

Figure 2.7: Illustration of Stern and Zeta potential of a particle [68]

The charge density surrounding a particle can be described by the potential at two layers: the Stern and diffusion layer (Figure 2.7). The Stern potential is opposite that of the particle surface due to electrostatic forces. In the same regard, the counterions from the bulk exert electrostatic force at the Stern layer to the diffusion layer. Effectively, the charge along the sliding plane is considered the zeta potential.

2.3.2.3 Rheology

The characterization of ink processing performance is also important, and in general, resulting surface tension and rheology are good indicators of ink deposition method suitability. In particular, rheological measurements or viscosity studies pertain to the ink's fluidity when subjected to shear forces. They yield valuable insights into microscopic properties, interactions among components, coating characteristics, homogeneity, morphology of the CL during drying, and ink stability [68].

Achieving optimal viscosity is paramount in the ink coating process to ensure high-quality, continuous, and defect-free coatings. The required viscosity varies depending on the specific coating technique employed; for instance, rod coating typically necessitates a higher ink viscosity. Catalyst ink viscosity is influenced by factors such as processing temperature, solvent viscosity, solid fraction, and shear rate. At low shear rates, catalyst inks demonstrate shear-thinning behavior as hydrodynamic forces disperse catalyst agglomerates. Furthermore, the extent of shear-thinning behavior provides insights into the structural reassembly and interaction of these agglomerates. This specific rheological behavior of catalyst inks provides a correlation between apparent ink viscosity and the interaction between agglomerates which can be used to characterize the evolution of CL microstructure.

2.3.2.4 Rheo-impedance measurement as tool for studying catalyst ink component interaction

There are numerous studies on rheological investigation of the properties of catalyst ink [75, 76]. This usually involves the measurement of viscosities and shearing behavior at different shear or strain rates and provides valuable insights about the microstructure evolution under shear. Under shear, the microstructure can evolve and rearrange, thereby changing the overall properties of the material. Another tool that could help in the investigation of properties under shear is electrochemical response measurement or electrochemical impedance spectroscopy (EIS). Coupled with rheological measurement, this can provide information on the evolution of material microstructure under flow. In addition, rheo-impedance measurements take advantage of the fact that rheological and electrical behaviors are coupled to the dynamic microstructure of material which is usually difficult to measure using optical or scattering techniques [77]. Several studies focusing on dielectric materials under rheo-impedance measurement are enumerated by Helal et al. [78]. A representation of the combined capabilities of rheo-impedance tool is presented in Figure 2.8.

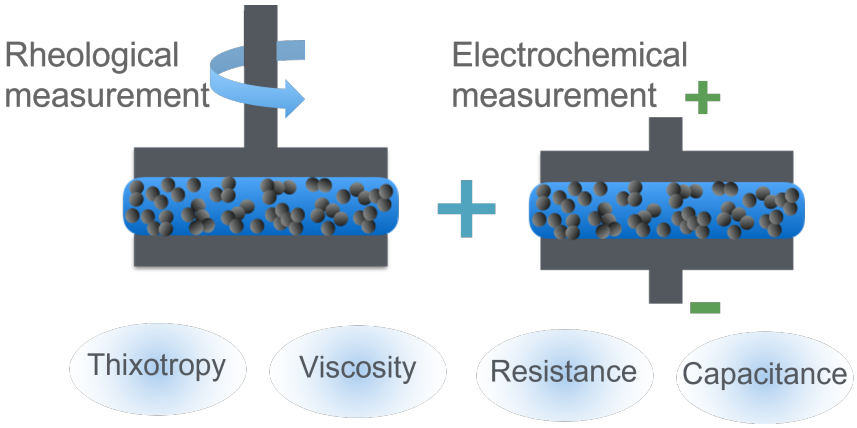

Figure 2.8: Representation of the combined capabilities of rheological and electrochemical measurement

Rheo-impedance measurement tool combines the capability of a typical rheometer that can measure thixotropy and viscosity at different shear rates and an electrical measuring tool that can measure impedance response simultaneously.

To date, there has been no studies combining rheological and electrical measurements on Pt/C catalyst ink materials. In the proposed work, an in-house rheo-impedance measurement tool is developed in order to measure viscosities and electrical properties at different shear rates. This would allow for understanding of how catalyst microstructure is affected by catalyst ink parameters such as ionomer-to-carbon ratio, type of solvent, and processing method as are factors considered in this study.

Chapter 3

AEMFC MODELING AND SENSITIVITY STUDY*

In this study, a steady-state, analytical 1-D AEMFC model is developed to include all of the fundamental physics. The newly developed model introduces a new approach to capture the transport properties of a gas diffusion electrode (GDE) through multilayer discretization of diffusion media (DM) and catalyst layer (CL), which allows for better representation of GDE architecture. Two-phase water transport in the diffusion media (DM) and catalyst layer (CL) are simulated using proposed empirical correlations as functions of local water activities. Aside from the inherent robustness of the 1-D model, the simulation approach and physics in this study can be readily adapted and validated using different materials and design parameters. Therefore, the proposed model provides a universal platform for simulating AEMFC with different materials, designs, and architecture. The model predictions are validated by the experimental results. Further sensitivity studies investigating the effect of membrane and ionomer properties as well as the operating conditions are also presented. Overall, this analytical-based model can be used as a powerful platform for investigating transport phenomena and performance of an AEMFC under various operating conditions.

3.1 Model Formulation

The AEMFC model consists of the electrochemical reaction, mass, heat, and charge transport. A schematic of the 1-D steady state, non-isothermal AEMFC model domain and transport processes is shown in Figure 3.1. This study aims to present a framework with which all the relevant physics can be incorporated into a 1-D analytical model for predicting the AEMFC performance at different operating conditions. While many modeling parameters are material- or design-specific, the governing physics, coupling behaviors, and computational strategies used in this model are applicable to general AEMFC operation. A detailed insight of each physics and important cell parameters are presented in the succeeding subsections.

---

* Portions of this chapter were previously published as "Mora, J. M., et al. "Analytical-based Simulation Approach for an Anion Exchange Membrane Fuel Cell." *Energy Conversion and Management*, vol. 273, **2022**, 116382," and are adapted with permission from all co-authors.

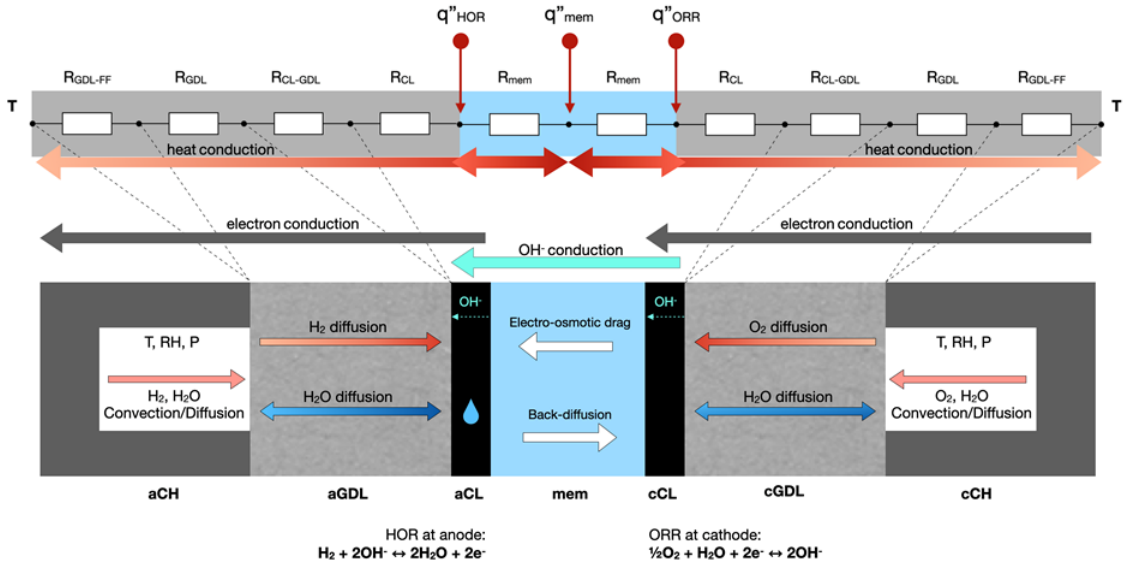

Figure 3.1: A schematic diagram illustrating the AEMFC model domain, transport processes, and equivalent thermal resistance network with heat sources.

3.1.1 Cell Voltage and Overpotentials

The overall objective of this analytical model is to accurately predict the electrochemical performance of the cell as reflected by the cell voltage, V_{cell}, which can be calculated by:

$$V_{cell} = E_{rev} - \sum_i \eta_i \tag{3.1}$$

where E_{rev} is the thermodynamic reversible cell potential, and η_i represents voltage losses due to electrochemical activation, ohmic overpotential, mass transport losses.

The Nernst equation is used to calculate the thermodynamic reversible cell potential, E_{rev} [18]:

$$E_{rev} = \frac{\Delta G}{2F} + \frac{\Delta S}{2F}(T - T_{ref}) - \frac{RT}{2F} ln\left(\frac{a_{H_2O}}{a_{H_2} \times {a_{O_2}}^{0.5}}\right) \tag{3.2}$$

where ΔG and ΔS are the changes in Gibbs free energy and entropy, respectively, T is the operating temperature at the catalyst layer, and T_{ref} (298 K) is the reference temperature. R is the universal gas constant, and F is the Faraday's constant. a_{H_2O}, a_{H_2}, and a_{O_2} represent the activities for H_2O, H_2 and O_2, respectively, in the

catalyst layer. Assuming ideality, the activities are equal to the partial pressures of each species (a_{H_2O}=p_{H_2O}, a_{H_2}=p_{H_2}, a_{O_2}=p_{O_2}).

The Butler-Volmer equation is used to relate the reaction rate to the activation overpotential for both anode HOR and cathode ORR [18]:

$$i = i_{0,a}\left[\left(\frac{p_{H_2}}{P_{ref}}\right) exp\left(\frac{2\alpha_a F\eta_{HOR}}{RT}\right) - \left(\frac{p_{H_2O}}{P_{ref}}\right)^2 exp\left(\frac{-2(1-\alpha_a)F\eta_{HOR}}{RT}\right)\right] \quad (3.3)$$

$$i = i_{0,c}\left[\left(\frac{p_{O_2}}{P_{ref}}\right)^{0.5}\left(\frac{p_{H_2O}}{P_{ref}}\right) exp\left(\frac{2\alpha_c F\eta_{ORR}}{RT}\right) - exp\left(\frac{-2(1-\alpha_c)F\eta_{ORR}}{RT}\right)\right] \quad (3.4)$$

where $i_{0,a}$ and $i_{0,c}$ are the effective exchange current densities for HOR and ORR, α_a and α_c are the anodic and cathodic charge transfer coefficients, η_{HOR} and η_{ORR} are the HOR and ORR activation overpotentials, respectively. P_{ref} (1 atm) is the reference pressure. Water vapor is a product in HOR and a reactant in ORR, therefore, the water partial pressure is explicitly included in Eqs. 3.3 and 3.4. The effective exchange current density can be calculated as:

$$i_{0,m} = i_{0,m}^{ref} \times (\chi \times rf) \times \ exp\left[\frac{-E_{A,m}}{R}\left(\frac{1}{T} - \frac{1}{T_{ref}}\right)\right] \quad (3.5)$$

where the subscript m represents either anode or cathode reaction, χ is the catalyst utilization factor and is equal to 1 for the base model, rf is the electrode roughness factor, E_A is the activation barrier, and i_0^{ref} is the reference exchange current density.

3.1.2 Heat Transport

Thermal energy generated from an electrochemical system includes entropic heat of reactions, irreversibility of electrochemical reactions, and Joule heating [79]. For an AEMFC, the total heat generated per unit area, q''_{total}, can be calculated as:

$$q''_{total} = \left(\frac{|\Delta H|}{2F} - V_{cell}\right) \times i \quad (3.6)$$

where ΔH is the enthalpy of the overall reaction. Since the reactions are present in both electrodes, heat is generated in anode and cathode according to the overpotentials. In addition, Joule heating due to both electrical and ionic transport resistances are considered. The heat generation due to ionic conduction through the electrode and membrane may become significant especially under dry conditions

due to increasing resistance [79]. Since the diffusion media and flowfield are highly conductive, heat can be assumed to be dissipated from three point sources: anode, cathode, and membrane. Lastly, the additional entropic heating effect is lumped with the heat generation in the cathode since the majority of the overpotential is resulted from the ORR loss.

Heat transport in the fuel cell is dominated by conduction and the heat transfer rate is dictated by the geometry and thermal conductivity of each component. The final equivalent thermal resistance network with illustration of the point sources are shown in Figure 3.1. The local temperature at the membrane-electrode interfaces (T_a and T_c) and at the center of the membrane (T_m) can be solved using the matrix inversion:

$$\begin{bmatrix} T_a \\ T_c \\ T_m \end{bmatrix} = \begin{bmatrix} \frac{1}{R_{th,a}} + \frac{2}{R_m} & 0 & -\frac{2}{R_m} \\ -\frac{2}{R_m} & -\frac{2}{R_m} & \frac{4}{R_{mem}} \\ 0 & \frac{2}{R_m} + \frac{1}{R_{th,c}} & -\frac{2}{R_m} \end{bmatrix}^{-1} \begin{bmatrix} q''_{HOR} + \frac{T}{R_{th,a}} \\ q''_{mem} \\ q''_{ORR} + \frac{T}{R_{th,c}} \end{bmatrix} \tag{3.7}$$

where R_i is the thermal resistance and $q^{"}$ is the heat source. Knowing the local temperature at anode, cathode, and membrane, heat fluxes across all components in the cell can be calculated through iterative process and the non-isothermal temperature distribution in the AEMFC can be solved. The detailed calculation flow chart of the local temperature distribution is shown in Figure A.1 in the Appendix.

3.1.3 Mass Transport

In an AEMFC, humidified hydrogen and air are supplied to the anode and cathode flowfield, respectively. In this section, mass transport of the reaction species are considered in the through-plane direction between the flow channel and catalyst layer. In the flow channel, mass transport is governed by both diffusion and convection, which can be quantified using Sherwood number (Sh) to calculate the channel mass transport resistance for species i [18]:

$$R_i^{ch} = \frac{D_h}{Sh \times D_{i,mix}} \tag{3.8}$$

where D_h is the hydraulic diameter and $D_{\mathrm{i,mix}}$ is the diffusivity of species i in a mixture.

In the gas diffusion media, mass transport is mostly governed by Fick's diffusion [18]. The steady-state molar flux of each species, $N_i^{''}$, can be calculated as:

$$N_i^{''} = -D_{i,mix}^{eff} \frac{dC_i}{dx} \tag{3.9}$$

where C_{i} is the molar concentration of species i and $D_{i,mix}^{eff}$ is the effective diffusivity of gas species i in the porous medium. The effective diffusivity can be correlated by the porosity (ϵ) and tortuosity ((τ) of the porous medium as [18]:

$$D_{i,mix}^{eff} = D_{i,mix} \times \frac{\varepsilon}{\tau} \tag{3.10}$$

The effective diffusivity of the gas diffusion can be measured using the limiting current experiment in a PEMFC [80]. Therefore, the diffusive mass transport resistance of species i in the diffusion media can be calculated as:

$$R_i^{GDL} = \sum_{k=1}^{N} \frac{f_{geom}\delta_k^{GDL}}{D_{i,mix}^{eff}} \tag{3.11}$$

where N presents the total number of the segmented diffusion layer, δ_k^{GDL} is the thickness of each discretized layer in the domain, and f_{geom} is the geometric factor accounting for the increased diffusion length from flow channel to electrode surface due to land/channel design. Detailed calculation method and discussion of f_{geom} can be found in our previous study [18].

In addition to Fick's diffusion, there are other non-pressure dependent transport mechanisms occurring in the cell including Knudsen diffusion through small pores and oxygen permeation through liquid water/ionomer films [81]. For simplicity, the non-Fickian transport resistance in the electrode can be represented by R^{NF} as a function of roughness factor [82]:

$$R^{NF} = \frac{11.2}{rf} + 0.053 \tag{3.12}$$

With the cell components arranged in series, the total transport resistance can be calculated by the sum of the resistance of each component. Therefore, the local concentration of species i can be solved using the following equations:

$$C_i^{CL} = C_i^{ch} - \frac{i}{nF}\left(R_i^{ch} + R_i^{GDL} + R_i^{NF}\right) \tag{3.13}$$

$$C_{H_2O,a}^{CL} = C_{H_2O,a}^{ch} + (2 - f_{H_2O})\frac{i}{2F}\left(R_{H_2O}^{ch} + R_{H_2O}^{GDL} + R_{H_2O}^{NF}\right) \tag{3.14}$$

$$C_{H_2O,c}^{CL} = C_{H_2O,c}^{ch} + (f_{H_2O} - 1)\frac{i}{2F}\left(R_{H_2O}^{ch} + R_{H_2O}^{GDL} + R_{H_2O}^{NF}\right) \tag{3.15}$$

Liquid water in the cell would block diffusion pathways for gas reactants and product, which in turn, resulted in additional transport resistance. From an experimental study by Sarker et al. [80], they reported a value of 4.70 for τ/ε of Toray TGP-H-060 GDL with 5 wt.% PTFE wetproofing under dry condition and 22% compression strain rate, but the transport resistance increases drastically under saturated conditions. To account for this phenomenon, a two-phase transport correlation is proposed where the τ/ε parameter varies as a function of local water activity:

$$\frac{\tau}{\varepsilon} = \begin{cases} 4.70 & for\ a_w < 1.0 \\ 4.70 \times \psi & for\ a_w \geq 1.0 \end{cases} \tag{3.16}$$

where ψ is a multiplier value due to liquid water and is specific to GDL material and structure, and a_w is the water activity defined as water partial pressure divided by the saturation pressure. For the base model of this study with Toray 060 with 5% PTFE, ψ is estimated to be equal to 2.25 based on the experimental results by Chuang et al. for cells with around 40-45% water saturation level [83]. The saturation pressure, p^{sat}, can be obtained as [84]:

$$\begin{aligned} \log p^{sat} = -2.1794 + 0.02953\,(T - 273.15) - 9.1837 \times 10^{-5}\,(T - 273.15)^2 \\ +1.4454 \times 10^{-7}\,(T - 273.15)^3 \end{aligned} \tag{3.17}$$

where T is the local temperature in Kelvin and p^{sat} is in atm.

In the catalyst layer domain, liquid water tends to cover the active reaction sites and therefore results in a decrease in roughness factor. Based on the experimental results, we propose an empirical-based correlation between the local water activity and electrode roughness factor for predicting performance under wet condition. The main goal of this two-phase model, beyond its simplicity, is to provide a reasonable estimate of cell performance using local water activity without considering complicated phase changes and two-phase flows within the cell.

3.1.4 Membrane water transport

Similar to a PEMFC, water transport through the alkaline exchange membrane is primarily driven by back diffusion and electro-osmotic drag. Therefore, the net water molar flux through the membrane (N''_{H_2O}) from anode to cathode can be represented by:

$$N''_{H_2O} = f_{H_2O}\frac{i}{2F} = N''_{H_2O,diff} - N''_{H_2O,drag} \tag{3.18}$$

wherein the water back diffusion flux through the membrane is governed by water content in the membrane and can be calculated as:

$$N''_{H_2O,diff} = -\frac{\rho_m}{EW} D_w \frac{d\lambda}{dz} \tag{3.19}$$

where ρ_{m} and EW are the dry density (g cm^{-3}) and equivalent weight (g mol^{-1}) of the membrane, respectively, λ is the water content in the membrane and is defined as the mole of H_2O per mole of functional group in the membrane, and D_{w} is the membrane water diffusivity (cm^2 s^{-1}). The water flux by electro-osmotic drag is given by:

$$N''_{H_2O,drag} = n_d \frac{i}{F} \tag{3.20}$$

where n_{d} is the electro-osmotic water drag coefficient in the membrane. The water transport parameters D_{w} and n_{d} are strongly dependent on the type of membrane and operating conditions. These parameters along with other membrane properties and their correlations are described in detail in Section 3.1.6.

Combining Eqs. (3.18) to (3.20) forms a first order differential equation which is then solved with an initial guess value of $f_{\mathrm{H_2O}}$ to obtain the steady-state membrane water content as a function of membrane thickness, $\lambda(z)$. The initial guess for $f_{\mathrm{H_2O}}$ must be properly chosen, otherwise, the calculation may diverge and the water molar flux balance of Eq. 3.18 is not satisfied. Detailed iterative calculation procedure for the water flux balance is presented in Figure A.2 in the Appendix. The water balance calculation loop as well as non-isothermal heat transfer calculation are included in the mass balance loop presented in Figure A.3 in the Appendix.

3.1.5 Charge transport

There are two charged species, electrons and hydroxide ions, transporting in an AEMFC between the anode and cathode. The voltage losses in the cell resulting from charge transport generally follows Ohm's law and can be calculated as:

$$\eta_{Ohmic} = i \times (R_{e-} + R_{OH^-}) \tag{3.21}$$

where $R_{\mathrm{e^-}}$ is the electrical resistance of the circuit. For the membrane, the area-specific resistance for ionic transport can be derived by integrating the local resistance over the membrane thickness:

$$R_{OH^-} = \int_0^{\delta_{mem}} \frac{dz}{\sigma\left[\lambda\left(z\right)\right]} \tag{3.22}$$

where σ is the ionic membrane conductivity (S cm^{-1}), which is strongly dependent on membrane hydration. Experimental studies of AEM show that, similar to PEM, the ionic membrane conductivity increases with cell temperature and water content [85]. A detailed discussion of this parameter and correlation used in the model are described in Section 3.1.6.

In the porous catalyst layer, there are both ionic and electron charge transfer as shown in Figure 3.1. The ionic transport resistances in the electrodes are not strictly Ohmic and have a non-linear dependence on the operating current density. In particular, the ionic transport loss can be significant when the catalyst layer is relatively dry [86]. From the studies of a PEMFC, analytical solutions of the effective ionic resistance were obtained in the cathode [86] and anode [87]. Since there are no available correlations for an AEMFC, similar approaches obtained from PEMFC are adopted in this model. Assuming Tafel kinetics for the electrochemical reaction, the effective ionic transport resistance can be written as [86]:

$$R_{ionic}^{eff} = \frac{R_{sheet}}{3+\zeta} \tag{3.23}$$

where $R_{\text{sheet}} = \delta_{CL}/\kappa_{eff}$ is the area-specific ionic conduction resistance through the entire electrode thickness (δ_{CL}) and ζ is a correction factor that accounts for the influence of catalyst utilization on the effective length of ionic transport in the catalyst layer. κ_{eff} is the effective ionic conductivity and can be calculated as [86]:

$$\kappa_{eff} = \kappa \times \frac{\varepsilon_i}{\tau} \tag{3.24}$$

where κ is the ionic conductivity of the ionomer, ε_{i} is the ionomer volume fraction, and τ is the tortuosity of electrode. The ionomer volume fraction is dependent on RH and is given by [88]:

$$\varepsilon_i = \left(\frac{I}{C}\right)\left(\frac{10}{f_t \rho_{i,dry}}\right) \times \left(1 + \frac{M_w \rho_{i,dry} \lambda}{\rho_w EW}\right) \tag{3.25}$$

where I/C is the ionomer-to-carbon weight ratio, EW is the equivalent weight, $\rho_{\text{i,dry}}$ is the dry density of ionomer, M_{w} is the molecular weight of water, ρ_{w} is the water density, and f_{t} is a factor for electrode thickness calculation. The values for these parameters are given in Table 3.1.

In the linear region of the Butler-Volmer kinetics, the effective ionic transport resistance can be calculated as [87]:

$$R_{ionic}^{eff} = \frac{1}{\kappa_{eff} S}\left(\frac{e^{S\delta_{CL}} + e^{-S\delta_{CL}}}{e^{S\delta_{CL}} - e^{-S\delta_{CL}}} - \frac{1}{S\delta_{CL}}\right) \tag{3.26}$$

where S is a kinetic parameter (cm^{-1}) that can be calculated as:

$$S = \left[\frac{ECSA \times Pt\ loading \times i_0}{\kappa_{eff} \delta_{CL}} \times \frac{(\alpha_a + \alpha_c) F}{RT} \right]^{1/2} \tag{3.27}$$

The equation above is further explained in Ref. [87].

Even though the HOR and ORR in an AEMFC typically fall in the Tafel approximation region, both Eqs. (3.23) and (3.26) are used to investigate the sensitivity of ionic transport resistance in the electrode. In addition, the effective ion transport thickness in the catalyst layer is adjusted according to the local current density distribution to account for catalyst utilization and slowness of reaction.

3.1.6 Model assumptions and input parameters

In this 1-D steady-state, non-isothermal model, the following assumptions are made:

1. The flow is assumed to be fully developed, laminar, and steady.
2. Ideal gas law is followed.
3. The membrane is assumed to be impermeable to gas phase (no crossover of gases).
4. Material properties are isotropic.
5. Land/channel effect on gas transport resistance is accurately accounted for by f_{geom} (Section 3.1.3).
6. Liquid water is stationary and water vapor diffusion is the dominant water transport mechanism.
7. Membrane water diffusivity and electro-osmotic drag coefficient are constant throughout the membrane thickness

For water transport in the membrane, it is imperative to obtain and input accurate membrane properties in the model. Li et al. [89] and Duan et al. [85] provided the groundwork for measuring and providing correlations for water content and transport properties of the Tokuyama A201 hydrocarbon-based membrane. Those correlations have been instrumental in succeeding modelling studies [13, 56, 57]. In this work, correlations for membrane properties are expanded to include perfluorinated anion exchange membrane (PF AEM), referred to as Gen 2 [90]. This AEM has methylated sulfonamide linkages to the 3M backbone with six methylene

groups tethered to a trimethyl ammonium cation. The structure of PF AEM Gen 2 membrane is in Figure A.4 in the Appendix and more details can be found in Ref. [90].

The water content of the PF AEM Gen 2 membrane can be shown as a function of water activity measured by Divekar et al. [91]:

$$\lambda = \begin{cases} -0.0338 + 13.15a_w - 19.13a_w^2 + 20.82a_w^3 & for\ a_w < 1.0 \\ -0.3787 + 15.19a_w & for\ a_w \geq 1.0 \end{cases} \tag{3.28}$$

Comparing with A201 and Nafion, the water content of Gen 2 membrane is found to be the highest for all applicable ranges of a_w as shown in Figure A.5 in the Appendix. Gen 2 membrane ionic conductivity, σ (mS cm^{-1}), is provided by Divekar et al. [91] and Park et al. [90] as a function of water content and temperature:

$$\sigma = (0.0176T - 4.826)\,\lambda + (0.0083T - 2.312)\lambda^2 \tag{3.29}$$

Gen 2 membrane exhibits high conductivity with reasonable water content, which is comparable to PEM counterpart. Based on the derived correlation, Gen 2 membrane conductivity is significantly higher than that of A201 membrane as shown in Figure A.6 in the Appendix.

Observing from Eqs. (3.19) and (3.20), membrane water diffusivity and electro-osmotic drag coefficient are critical for predicting water transfer in the membrane accurately. Currently, there is no available data for these two properties for Gen 2 membrane. Therefore, correlations available from literature for A201 membrane are used in the model. Similar to the rest of the membrane properties, the correlations for D_{w} and n_{d} used in this model are presented in Figures A.7 and A.8 in the Appendix.

It should be noted that the effects of CO_2 contamination and bicarbonate formation are not considered in this model due to their complexity in degradation. The current model is primarily focusing on the effect of material properties and operating conditions on cell performance. While CO_2 contamination has a strong effect on ionic conductivity due to reduced active cites for hydroxide transport, this effect can be simulated by scaling the ionomer conductivity as demonstrated later in Section 3.3.4.3.

Table 3.1: Parameters used in the AEMFC analytical model

Parameter	Symbol	Value
Geometric parameters		
Channel hydraulic diameter	D_h	723 μm
Sherwood number	Sh	2.4
Gas diffusion layer thickness	δ_{GDL}	190 μm
Catalyst layer thickness	δ_{CL}	20 μm
Membrane thickness	δ_{mem}	45 μm
Thermodynamic parameters		
Gibb's free energy [92]	ΔG	-237.13 kJ mol^{-1}
Entropy or reaction [93]	ΔS	-163.46 J mol^{-1} K^{-1}
Enthalpy of reaction [93]	ΔH	-285.83 kJ mol^{-1}
Kinetic parameters		
HOR activation energy [94]	$E_{A,HOR}$	18 kJ mol^{-1}
ORR activation energy [95]	$E_{A,ORR}$	66 kJ mol^{-1}
HOR exchange current density [30]	$i_{0,a}^{ref}$	1×10^{-5} A cm$_{Pt}^{-2}$
ORR exchange current density [Fitted]	$i_{0,c}^{ref}$	1×10^{-7} A cm$_{Pt}^{-2}$
HOR charge transfer coefficient [30]	α_a	0.5
ORR charge transfer coefficient [30]	α_c	0.5
Electrochemically active surface area	$ECSA$	26 m^2 g$_{Pt}^{-1}$
Pt loading		0.64 mg$_{Pt}$ cm^{-2}
Thermal transport parameters		
Bipolar plate thermal conductivity [96]	k_{FF}	0.55 W cm^{-1} K^{-1}
GDL thermal conductivity [96]	k_{GDL}	1.7×10^{-2} W cm^{-1} K^{-1}
CL thermal conductivity [96]	k_{CL}	2.7×10^{-3} W cm^{-1} K^{-1}
Membrane thermal conductivity [96]	k_{mem}	1.2×10^{-3} W cm^{-1} K^{-1}
GDL-CL contact thermal resistance [96]	R_{GDL-CL}	1 cm^2 K W^{-1}
BPP-CL contact thermal resistance [96]	R_{FF-GDL}	2 cm^2 K W^{-1}
Other parameters		
Ionomer-to-carbon ratio	I/C	0.625
Ionomer tortuosity in CL	τ	1.0
Factor for electrode thickness	f_t	20.83 μm mg$_C^{-1}$ cm^2
Ionomer density	$\rho_{i,dry}$	1.97 g cm^{-3}
Equivalent weight of ionomer	EW	0.975 g cm^{-3}
Water density	ρ_w	1108 g mol^{-1}
Molecular weight of water	M_w	18.015 g mol^{-1}

3.2 Experiments

Fuel cell tests were performed using a Greenlight G20 test station, which precisely controlled and monitored electronic load, gas flow rates, temperature, relative humidity, and backpressure. The high frequency resistance (HFR) of the cell was measured at 10 kHz by electrochemical impedance spectroscopy (EIS) using a Gamry Reference 3000 [80]. Membrane electrode assemblies (MEAs) were prepared with perfluorinated anion exchange polymer as both membrane and ionomer material. Synthesis and characterization of Gen 2 polymer were discussed in detail by Park et al. [90] and Divekar et al. [91]. The gas diffusion electrode (GDE) was prepared by spray coating the catalyst ink material onto Toray TGP-H-060 GDL with 5 wt.% PTFE loading. Details of catalyst ink preparation was reported by Omasta et al. [97]. The Pt catalyst loading was 0.64 $mg\ cm^{-2}$ for both the anode and cathode. The testing AEM fuel cell hardware consisted of graphite flow fields with straight parallel flow channels and an active area of 2 cm^2, gold-plated copper current collector plates, and aluminum alloy end plates. PTFE gaskets were used to seal the cell and control the GDE to have a target strain rate of 25%. Prior to fuel cell testing, the GDE and AEM material were immersed in aqueous KOH solution (1 M, Fisher Chemical) for 60 min to enable hydroxide ion-exchange.

Before polarization testing, a break-in procedure was performed to activate the cell and ensure proper ion transport by holding the cell at 0.50 V until a plateau in current density is reached. During the break-in process, the cell temperature was increased gradually from room temperature to 70°C under fully humidified conditions. The steady-state polarization tests were conducted by holding each voltage step for 30 minutes. For baseline condition, pure H_2 and O_2 were fed into the anode and cathode, respectively, at the flow rate of 0.40 NLPM for both, to achieve differential cell conditions under high stoichiometric flow operation. The inlet relative humidity, cell temperature, and exit pressure were controlled to be 92%, 70°C, and 131 kPa abs., respectively. Pressure values discussed in succeeding sections are all in absolute values. For dynamic conditions, the polarization curve was measured using linear sweep voltammetry (LSV) method by sweeping voltage from OCV to 0.10 V at a scan rate of 10 mV s^{-1} under different humidification levels: 73%, 80%, and 90% RH.

3.3 Results and discussion

3.3.1 Baseline model predictions with experimental validation

This newly developed 1-D analytical AEMFC model is used to predict the performance at baseline operating conditions and the results are compared to the experimental data as shown in Figure 3.2(a). All model predictions agree relatively well with the cell performance at the given operating conditions. Note that the

base model consists of all physics discussed previously. To further analyze the cell performance, each component contributing to the overall polarization loss of the base model is shown in Figure 3.2(b). The concentration loss and anode ionic transport loss are minimal under the baseline operating conditions. Significant kinetic losses from HOR and ORR can be observed throughout the entire current density, while the ohmic loss increases with increasing current density. The ionic transport loss in the cathode CL is also significant at high current density indicating cathode drying. As previously discussed, there is an inherent water imbalance in an AEMFC since water is generated at the anode twice as much as it is consumed in the cathode. This is further exacerbated at high current density since more water is being transported through the membrane from cathode to anode via electro-osmotic drag resulting in an even drier cathode CL. As a result, the membrane water content at the cathode side as a function of current density reduces with increasing current density as shown in Figure 3.2(c). For the sensitivity study of water transport across the membrane, the model prediction assuming no net water flux through the membrane (i.e., $f_{H_2O} = 0$) is also presented in Figure 3.2(a) and (c). The case of no net water flux across the membrane slightly underpredicts the cell performance due to high ionic loss in the cathode CL resulting from reduced water content as shown in Figure 3.2(c). While the overall cell performance at zero net water flux does not vary significantly from the base model, its effect on cathode hydration due to water transport is clear as can be seen in Figure 3.2(c). Therefore, modeling water transport across the membrane accurately is critically important, especially for cases where cathode drying is likely to happen as later demonstrated in Sections 3.3.4.2 and 3.3.4.3.

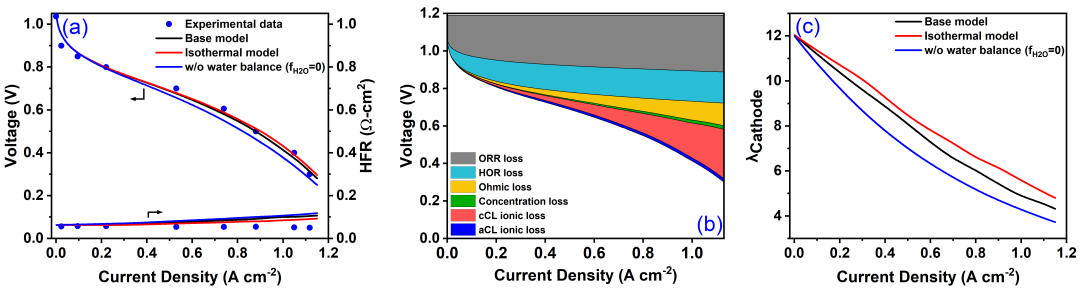

Figure 3.2: (a) Comparison of experimental data with simulation results based on the inclusion of different physics; (b) breakdown of various overpotentials calculated using the base model at 100% H_2/100% O_2, 70°C, 131 kPa, and 92% RH, and (c) water content at membrane/cathode catalyst layer interface.

Since temperature has a significant effect on local RH, isothermal model results are also compared with the base model in Figure 3.2(a) and (c). Under the

baseline operating conditions, the case with isothermal condition in the cell shows almost identical results compared to the base model. To illustrate the non-isothermal effect, local distribution of temperature, RH, and membrane water content at 0.8 $A\ cm^{-2}$ are shown in Figure 3.3. Because of the increase in local temperature, the non-isothermal model predicts lower RH and membrane water content in the cell resulting in increased ionic loss, but is compensated with less mass transport loss. Even though the performance difference under baseline conditions is minimal, it is expected that the effect of non-isothermal condition would be significant when the cell is operating at high current density, low reactant concentration, and under more extreme wet or dry conditions. Therefore, including the non-isothermal model is essential for capturing the operating physics and predicting cell performance accurately under a wide range of operating conditions.

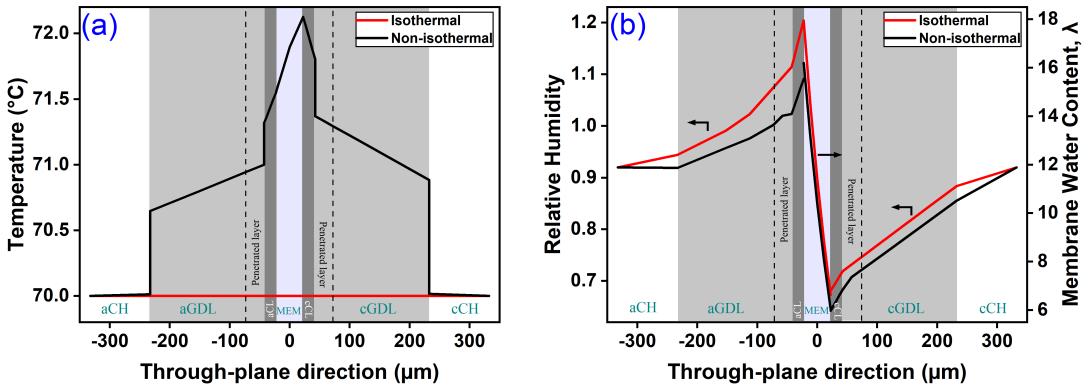

Figure 3.3: Profiles of (a) temperature in the cell and (b) RH in the GDL and CL, and water content in the membrane at 100% H_2/100% O_2, 70°C, 131 kPa, 92% RH, and 0.8 A cm^{-2}.

3.3.2 Empirical-based local flooding model

To test the reliability of the base model, an extreme operating condition of 10% H_2 is simulated and compared with the experimental data as shown in Figure 3.4(a). The experimental conditions were selected due to the clear observation of limiting current behavior. Observing from Figure 3.4(a), it is evident that the base model with two-phase function in the GDL discussed in Section 3.1.3 is not sufficient in accurately predicting the hydrogen mass transport loss observed from the experimental data, which exhibited limiting current behavior. Comparing the RH profile and membrane hydration predicted by the base model between 100% and 10% H_2 cases at 0.4 $A\ cm^{-2}$, a significant portion of the GDL and CL on the anode side exceed 100% RH for the 10% H_2 case as illustrated in Figure 3.4(b) while the cell stayed completely dry for the 100% H_2 case. Upon further analysis,

the diffusion resistance in the anode side is much greater due to high concentration of N_2. Therefore, water cannot be quickly diffused from the anode CL to channel, resulting in higher water retention and relatively humidity at the anode side. This difference in RH profiles is indicative of the performance sensitivity to local water activity. Therefore, additional two-phase functions to correlate CL and GDL mass transport losses with local water activity are needed to enhance the accuracy of the performance prediction of the base model.

In the base model, the CL is assumed to be dry and all of the active sites are available regardless of the local relative humidity. This assumption is clearly incorrect since liquid water in the CL not only incurs additional transport loss but also blocks active reaction sites [98]. Therefore, it is essential to model catalyst utilization factor, χ, in Eq. (3.5) as a function of local water activity. The proposed correlation for the catalyst utilization factor can be expressed in the form of:

$$\chi = (1 - L) + \frac{L}{1 + e^{[-k(a_w - x_m)]}} \tag{3.30}$$

where parameters L, k, and x_m are determined based on the empirical results and are estimated to be 200, -26.9, and 1.4, respectively, in our experiments. The empirical-based correlation of the catalyst utilization factor as a function of water activity is presented in Figure A.11 in the Appendix. The predictions of the base model with modified CL flooding correlation are plotted as red line in Figure 3.4(a). While significant improvement is observed and limiting current behavior is captured for 10% H_2, the modified model still overpredicts the performance. Therefore, the diffusion media between the catalyst layer and the flow channel need to be further examined to investigate this additional transport loss.

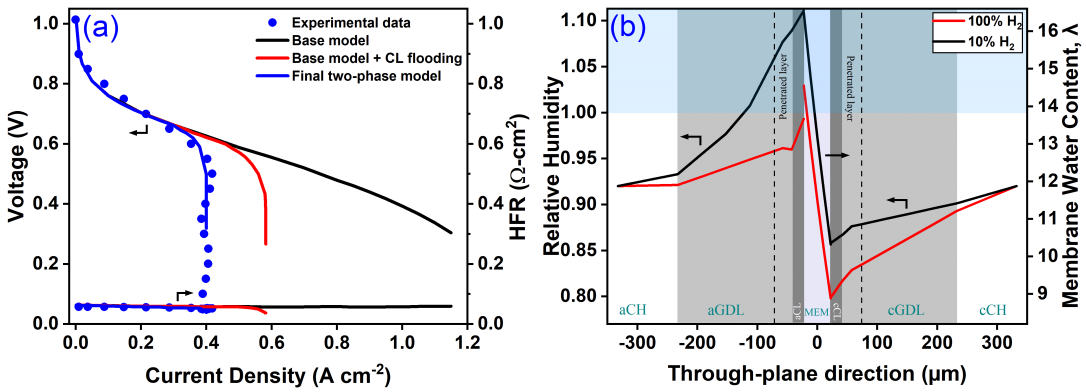

Figure 3.4: (a) Comparison of fuel cell simulations and experimental data at 10% H_2 using base and modified models; (b) profiles of RH in the GDL and CL, and water content in the membrane for 100% H_2 and 10% H_2 at current density of 0.4 A cm^{-2}. Cell conditions: 100% O_2, 70°C, 131 kPa, and 92% RH.

Fuel cell durability and performance are known to be very sensitive to its catalyst ink mixing, coating processes, and cell architecture [99–101]. In this study, the catalyst and ionomer are directly sprayed onto the porous GDL to form a gas diffusion electrode (GDE). Figure 3.5 shows the catalyst layer surface and cross-sectional SEM images of the GDL used in this study. Since the GDL has large pores in the order of 100 µm [12], the catalyst ink not only forms a catalyst layer on the surface but also shows significant penetration into the GDL depth. Therefore, the GDE can be characterized into three sublayers: bare GDL, catalyst-penetrated GDL, and the dense catalyst layer as shown in Figure 3.5(b). The transport properties of bare GDL can be measured using limiting current method and are discussed in Section 3.1.3. The dense catalyst layer is in direct contact with the membrane, and it is where most, if not all, of the electrochemical reactions occur. On the other hand, the catalyst-penetrated GDL is farther away from the membrane, which is expected to produce minimal reaction current, but incurs significant transport resistance due to reduced porosity and increased tortuosity. The estimated thickness of the catalyst-penetrated GDL is around 30 µm as observed from Figure 3.5(b).

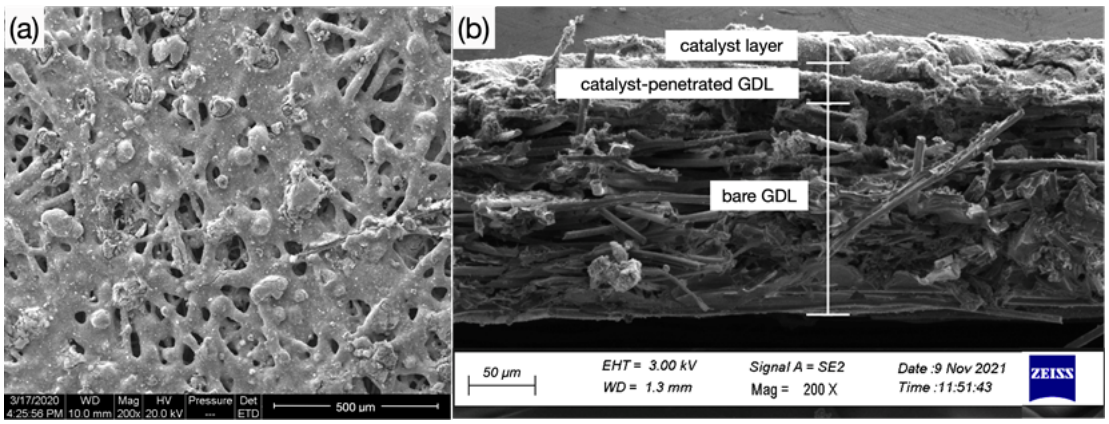

Figure 3.5: SEM images of GDE used in this study: (a) surface and (b) cross-section with estimates of the three sublayers.
Images courtesy of M. Sarker, S. Mehrazi, and M. Labata from TEEL.

From Figure 3.5(a), there are large agglomerates formed on the surface of the GDE, which also contribute to higher local gas transport resistance. As previously discussed, gas transport resistance in the GDE includes Fick's diffusion, Knudsen diffusion, and diffusion through water or ionomer film. However, isolation of these sources is extremely challenging and requires in-depth analysis and characterization of the nanoscale pore structure. In this study, an empirical approach is taken to correlate the additional performance loss to the increase of the transport resistance represented by τ/ε. Due to the blockage of catalyst materials, the τ/ε ratio of the catalyst-penetrated sublayer under dry condition is much higher than that of the base GDL and is estimated to be around 20 for our experiment. In addition, under fully humidified conditions, an empirical-based correlation of the two-phase multiplier, ψ, in Eq. (3.16) as a function of local water activity (a_w) in the catalyst-penetrated sublayer is proposed:

$$\psi = 1 + \frac{a}{1 + e^{[-b(a_w - c)]}} \tag{3.31}$$

where a, b, and c are fitted parameters based on the empirical results and are estimated to be 3.0, 300, and 1.01, respectively, in our experiments. The empirical-based correlation of the two-phase multiplier as a function of water activity is presented in Figure A.11 in the Appendix.

With the addition of both catalyst utilization and additional transport resistance in the catalyst-penetrated GDL, the final two-phase model is able to accurately predict the cell performance for 10% H_2 as shown by the blue line in Figure 3.4(a). After the modification, the final two-phase model is validated by the 100% H_2 to ensure good agreement as shown in Figure S9 in the Appendix. Besides hydrogen

sensitivity, the simulation results from the final model are also validated and agreed well with 50% O_2 case as shown in Figure A.10 in the Appendix. In conclusion, the base model is only limited to predict cell performance at high H_2/O_2 concentration under dry conditions. The newly proposed two-phase functions in the catalyst-penetrated sublayer and the catalyst layer can be applied to account for additional transport loss due to local flooding in the catalyst-penetrated GDL and reduction in catalyst utilization. Therefore, the final two-phase model is capable of predicting AEMFC performance for a wide range of operating conditions. However, the accuracy of the final model is highly sensitive to the two-phase fitted values in Eqs. (3.30) and (3.31), which depend strongly on catalyst composition and deposition method and can only be obtained empirically.

3.3.3 Modeling of dynamic behavior

The polarization curves obtained from LSV measurements can be described as having two distinct linear regions and represented by two lines with different slopes seen in Figure 3.6(a) and Figure A.12. For 92% inlet RH, the transition between these two regions is at around 1.3 A cm^{-2}. This apparent transition point moves to higher current density as inlet RH is decreased, i.e., for 80% RH, it is around 1.9 A cm^{-2}, and for 73% RH, the value is at 2.2 A cm^{-2}. These dual linear regions are also observed in previous studies utilizing voltage sweeps [102, 103]. These dynamic scans of AEMFC performance, while advantageous in terms of measurement speed, do not accurately capture the performance of the cell at steady-state that is why there is no limiting current observed in the polarization curve, only a gradual increase in current density as voltage is decreased. At high scan rates, there may not be enough time for the slow transport phenomena such as the mass transport of gases, and more so, water movement across the cell to reach steady state.

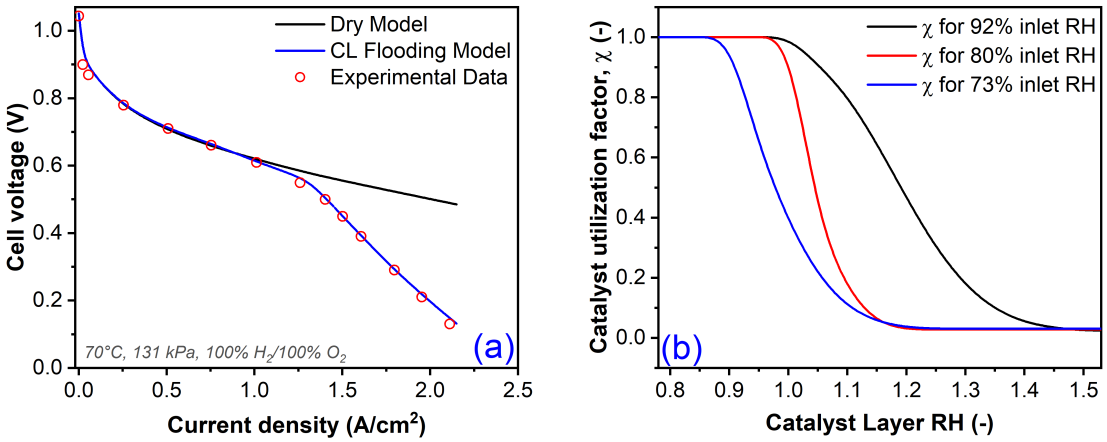

Figure 3.6: (a) Comparison of experimental and modeling results of cell at 92% RH 70°C, 131 kPaa, and 0.40/0.40 NLPM H_2/O_2 showing modeling results using Dry Model and CL Flooding Model; (b) Catalyst utilization factor used for different inlet RH conditions.

To model this behavior, the available active reaction sites in the CL is varied depending on local conditions. Accordingly, Equation 3.30 is modified and used with appropriate parameters to determine the catalyst utilization during flooding for each inlet RH. The modified equation is as follows:

$$\chi_{mod} = \frac{K}{1 + e^{[-G(a_w - x_m)]}} \tag{3.32}$$

where parameters K, G, and x_m are determined based on the empirical results from our experiments. The modeling result for 92% inlet RH condition as well as the empirical-based correlation of the catalyst utilization factor as a function of water activity are presented in Figure 3.6(a) and 3.6(b), respectively. The values for each parameter used in Eq. 3.32 are listed in Table A.1 in the Appendix. The modeling result for the 92% inlet RH case shows that using the Dry Model (i.e., $\chi_{mod} = 1.0$) represented by the black line, accurately predicts the performance of the cell until the end of the first linear (ohmic) region at current densities below 1.3 A cm^{-2}. However, as current density is increased further and more water is produced at the anode CL, the performance starts to gradually decline at a faster rate. In contrast with PEMFC, anode CL flooding is an issue in the high current density region for AEMFC since water is generated in the anode twice as much as it is consumed in the cathode. Studies also show that while the cathode seems always in drier conditions than the anode, flooding is also a concern at cathode CL at high current densities [103]. This observation dominates the second linear region which is mainly attributed to flooding

in the anode catalyst layer. By implementing a CL Flooding Model that utilizes χ as a function of local a_w for both anode and cathode CL, the predicted results have better agreement with the experimental data as represented by the blue line. The modeling results for the 80% and 73% inlet RH cases are presented in Figure A.12. For the lower inlet RH cases, the onset of CL flooding is assumed to be at lower local water activities and the extent of catalyst utilization is also different as illustrated by the different curves in Figure 3.6(b). The dependence of onset of flooding at different inlet RH is demonstrated in a previous study emphasizing the delicate balance between the need for high humidification for high OH^- conductivity and avoiding anode flooding [103]. These observations further reinforce how water accumulation in an AEMFC is more complex and dynamic than in a PEMFC and also opens more opportunities to control through a combination of operating conditions and material properties.

3.3.4 Sensitivity analysis

Based on our experimental observations, the performance of an AEMFC is highly sensitive to its material properties and operating conditions, especially the parameters that influence water transport through the membrane. The newly developed final two-phase model has robust algorithm, so the AEMFC performance results can be obtained using various membrane properties and correlations as presented in Figures A.5 to A.8 in the Appendix. In addition, the same modeling approach can be adapted to elucidate transport properties of different porous material and electrode morphologies by multilayer discretization in order to predict performance under dry and wet conditions. In this section, sensitivity analyses of the key parameters including relative humidity, electro-osmotic drag, and membrane water diffusivity, are carried out to investigate their effect on overall fuel cell performance.

3.3.4.1 RH sensitivity

Local RH conditions strongly affect AEMFC performance since mass transport and ionic conductivity are highly dependent on water content. In addition, ORR kinetics is also a strong function of water activity since water is a reactant of ORR in the cathode. Therefore, cell performance at different inlet RH is simulated using the final two-phase model and the results are shown in Figure 3.7(a). It can be observed that the cell performance is extremely sensitive to inlet RH conditions and the peak performance is near 92% RH for the input parameters and materials used in this study. When the RH is above 92%, limiting current behavior due to mass transport loss can be observed resulting from anode flooding. When the cell is operating at high RH and current density conditions, water tends to accumulate in the anode due to high electro-osmotic drag from cathode to anode and low back diffusion from anode to cathode, which results in anode flooding. In contrast, the cell

experiences high ionic transport losses in the membrane, as evident from the high HFR values, and cathode catalyst layer when the RH is less than 92% because of cathode drying. The result from this study demonstrates the narrow window of RH, balancing between anode CL flooding and cathode CL drying, to achieve a healthy performance of an AEMFC. To further evaluate the inherent water imbalance, the ionic transport loss in anode and cathode CLs are shown in Figure 3.7(b-c). As discussed in Section 3.3.1, the cathode CL ionic loss is significantly higher than that in the anode CL due to its lower water content.

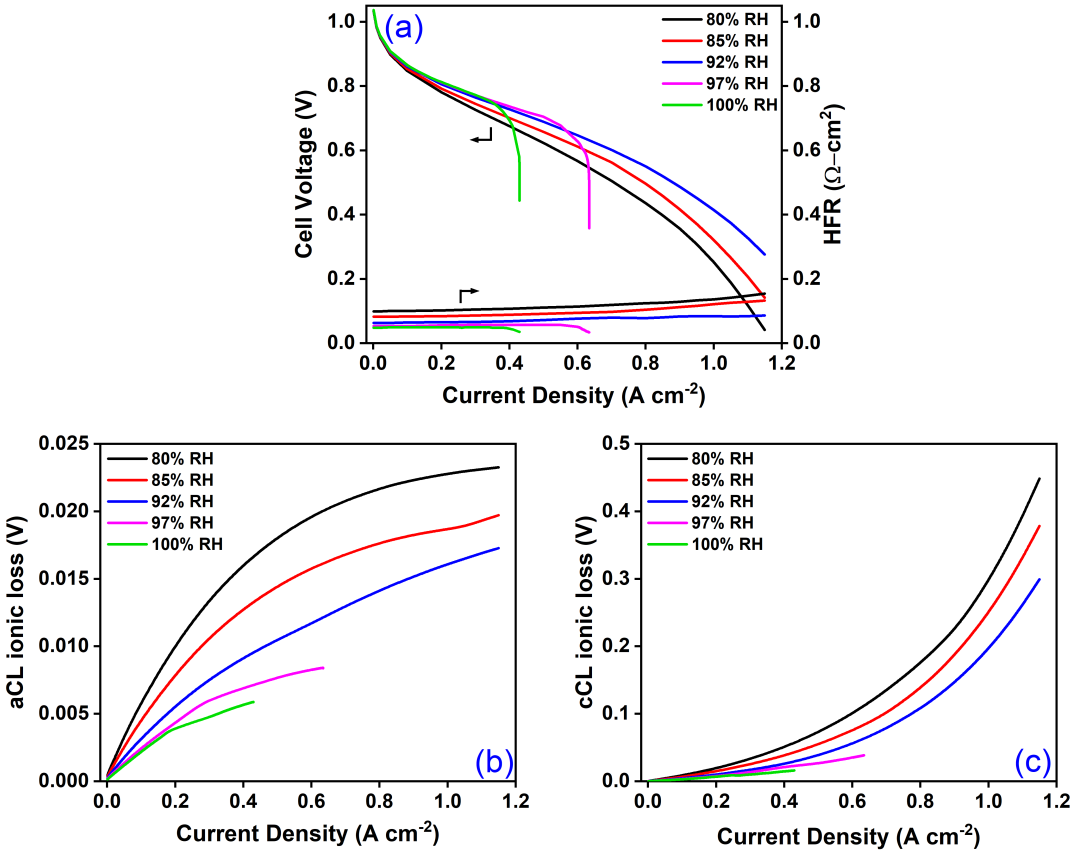

Figure 3.7: (a) Comparison of cell performance and HFR of an AEMFC at different inlet RH conditions predicted by the final two-phase model and the corresponding (b) anode and (c) cathode CL ionic loss. Cell conditions: 100% H_2/100% O_2, 70°C, and 131 kPa.

Asymmetric inlet RH is also studied to investigate the dominating effect between the anode and cathode, which can provide insight into the optimal water management strategies. As shown in Figure 3.8(a), similar performance behavior is observed compared with symmetric RH as shown in Figure 3.7(a) for varying the

anode RH. In contrast, varying cathode RH while keeping the anode RH at 92% mitigates anode flooding and the performance increases with increasing cathode RH due to reduced ionic transport loss as shown in Figure 3.8(b). The results indicate that anode RH is the dominating parameter.

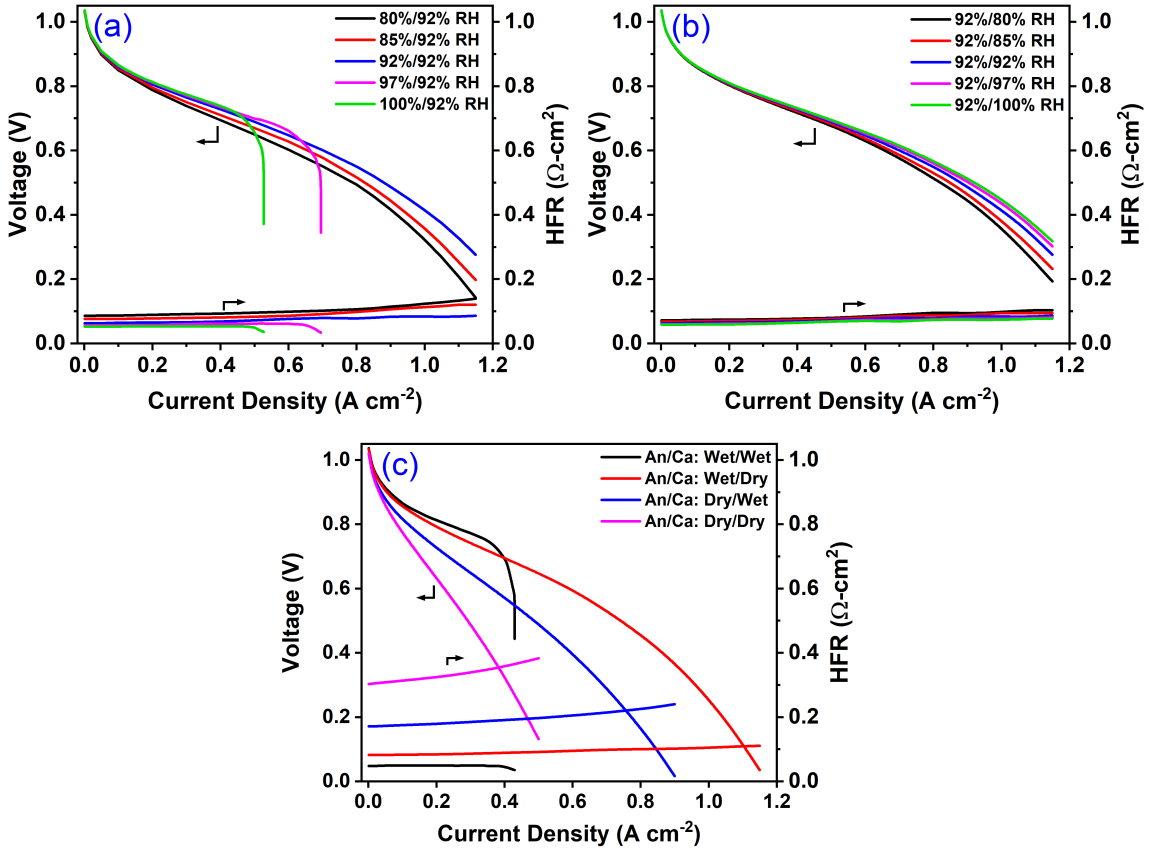

Figure 3.8: Cell performance predicted by the final two-phase model at (a) varying anode RH, (b) varying cathode RH, and (c) asymmetric RH using wet (100% RH) and dry (50% RH) conditions. Cell conditions: 100% H_2/100% O_2, 70°C, and 131 kPa.

To further highlight the effect of inlet RH, wet (100% RH) and dry (50% RH) conditions are used to model asymmetric humidification. The predicted cell performance is presented in Figure 3.8(c). Under wet conditions (black curve), the cell experiences anode flooding and quickly approaches limiting current. On the other hand, the cell suffers significant ionic transport loss under dry conditions (magenta curve). Comparing between the two asymmetric cases, the performance of dry anode/wet cathode (blue curve) is worse than that of wet anode/dry cathode (red curve) mainly due to the increase in ohmic and CL ionic losses. Initially, this

result seems to conflict with our earlier analysis aiming to improve the performance by preventing anode flooding and cathode drying. Upon further review, hydrogen diffusivity is more than three times higher than that of oxygen. For this reason, water diffusion at the cathode side is much lower, resulting in higher mass transport resistance. Therefore, under asymmetric inlet RH conditions, the water content of the membrane is much closer to the anode channel RH which, in turn, resulted in lower HFR for the case of wet anode/dry cathode. Since the cathode RH is at 50%, diffusion from anode to cathode is sufficiently active to prevent anode flooding, thus yielding the best performance for wet anode/dry cathode among the four cases. It is worth reiterating that the predicted results are strong functions of material properties, which may yield different conclusions as demonstrated in Section 3.3.4.2. The result from this sensitivity study fully demonstrates the delicacy and importance of water balance in an AEMFC.

3.3.4.2 Membrane water transport sensitivity

While correlation for water content (λ) and membrane conductivity (σ) are available for Gen 2 membrane material from Ref. [91], the electro-osmotic drag (EOD) coefficient (n_d) and membrane water diffusivity (D_w) data are not available at present. For the EOD coefficient, Huo et al. [49] proposed the following widely used correlation for A201 membrane:

$$n_d = 1.3 + 0.183\lambda \tag{3.33}$$

For the sensitivity study, we studied three cases ranging from half to doubling the EOD coefficient obtained from Eq. (3.33) and the predicted performances are shown in Figure 3.9(a). In addition, the corresponding predictions of membrane water content throughout the membrane are shown in Figure 3.9(b) and (c) for current density of 0.2 and 0.6 $A\ cm^{-2}$, respectively. Since the electro-osmotic drag follows the transport of the hydroxide ion, increasing the EOD coefficient would result in higher water flux from the cathode to the anode. Consequently, limiting current behavior caused by anode flooding can be observed for the case of doubling the EOD coefficient. This is indicative of significant hydration gradient between the anode and cathode side as shown in Figure 3.9(b) and (c). As shown in Figure 3.9, reducing EOD coefficient alleviates the extent of cathode drying, which in turn, enhances the performance due to lower cathode CL ionic loss. In conclusion, EOD coefficient is a critical parameter of an alkaline membrane and materials with a lower EOD coefficient would have improved cell performance and durability [14].

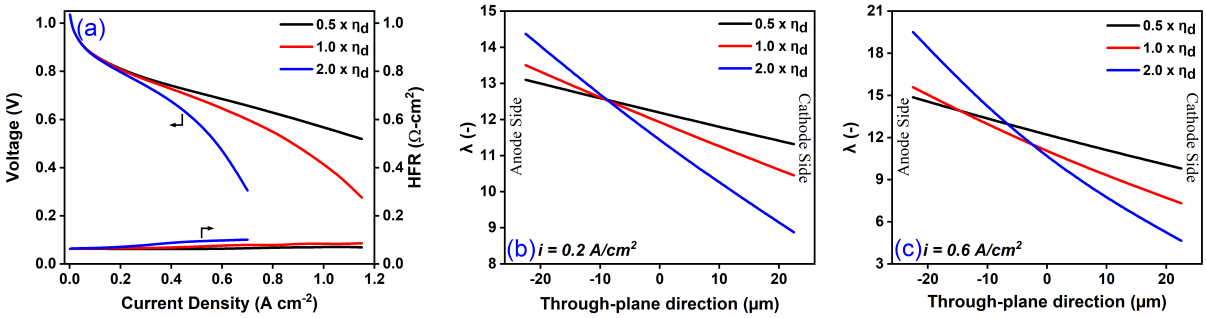

Figure 3.9: (a) Cell performance predicted by the final two-phase model of three scale factors for EOD coefficient and the calculated membrane water content at a current density of (b) 0.2 A cm^{-2} and (c) 0.6 A cm^{-2}. Cell conditions: 100% H_2/100% O_2, 70°C, 131 kPa, and 92% RH.

Another important parameter in membrane water transport is the water diffusion coefficient (D_w). Similar to the EOD coefficient, a sensitivity analysis by scaling D_w by 0.5 and 2 is done and the results are presented in Figure A.13. As mentioned previously, there is no correlation for D_w at present for the Gen 2 membrane. In this study, a correlation for D_w (m^2 s^{-1}) is proposed as:

$$D_w = 0.000555 \times \ e^{\left(\frac{\lambda}{2.02}\right)} + e^{\left[4800 \times \left(\frac{1}{303} - \frac{1}{T}\right)\right]} \tag{3.34}$$

Whereas high n_d promotes water transport from cathode to anode, higher D_w enhances water transport from anode to cathode via back-diffusion. Increase in water back-diffusion results to a more uniform cell hydration throughout the membrane thickness. This generates a lower rate of increase in cathode catalyst layer ionic loss and ORR activation loss with current density.

3.3.4.3 Sensitivity to cathode ionomer conductivity

Based on the results in Section 3.3.1, it is observed that the ionic loss in the cathode catalyst layer can be significant due to drying, especially at high current densities. The ionic loss in the anode catalyst layer is minimal in comparison. To investigate the effect of cathode ionomer conductivity to overall cell performance, a sensitivity analysis is performed by multiplying the cathode ionomer conductivity (σ) parameter with a scaling factor, 0.5 and 2.0. The ionic conductivity in the anode catalyst layer and membrane remain the same.

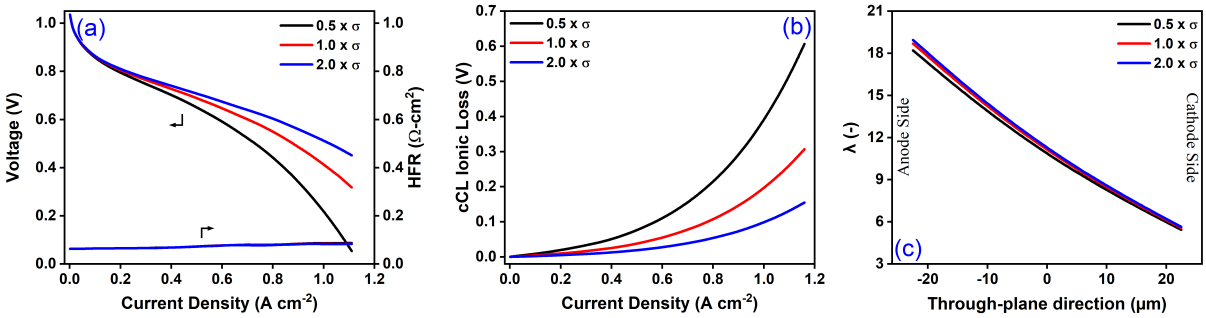

Figure 3.10: (a) Cell performance predicted by the final two-phase model at different cathode CL ionomer conductivity, (b) cathode CL ionic loss using different scale factors, and (c) calculated membrane water content at current density of 1.0 A cm^{-2}. Cell conditions: 100% H_2/100% O_2, 70°C, 131 kPa, and 92% RH.

As shown in Figure 3.10(a) and (b), increasing the ionomer conductivity in the cathode catalyst layer enhances the cell performance due to the reduction of the ionic loss in the cathode CL. In addition, the change of cathode ionomer conductivity does not have a significant effect on water content in the membrane as shown in Figure 3.10(c) under the baseline operating conditions. Therefore, increasing the cathode ionomer conductivity can play a crucial role in improving cell performance.

3.4 Conclusion

A 1-D analytical and empirical-based model of AEMFC incorporating all relevant physics is developed to predict cell performance. The model successfully predicts performance for dry and wet conditions using a multilayer material-specific approach that can be tailored for different catalyst and gas diffusion layer structures and transport properties. Apart from the newly introduced modeling approach, the following key findings from this study are listed below:

1. From the simulation results shown in Figure 3.2, substantial ORR and HOR kinetic losses can be observed throughout the range of the operating current densities. The ionic transport loss in the cathode catalyst layer is also significant due to cathode drying at high current density, which is a commonly observed in an AEMFC.

2. Location-specific multiple heat sources are incorporated in the model to accurately predict temperature and RH profiles inside the cell through non-isothermal calculations, which are essential to accurately predict performance under wet condition and/or low fuel concentration as illustrated in Figure 3.3.

3. The final two-phase model accounts for the additional losses resulting from the GDE and catalyst layer as a function of local water activity. This enables accurate prediction of AEMFC performance under both dry condition and wet conditions.

4. RH sensitivity analyses illustrate the delicate water balance on an AEMFC. The study shows that performance of wet anode/dry cathode is better than that of dry anode/wet cathode, which contradicts with the inherent water balance strategy. This is mainly due to high hydrogen diffusivity, which is three times greater than that of oxygen. Therefore, water diffusion rate at the cathode side is much lower contributing to higher mass transport resistance. As a result, membrane resistance is much lower when the anode is wet compared to that when the anode is dry.

5. Water transport at dynamic condition results in a secondary linear region in the polarization curve that can be modeled by varying the catalyst utilization factor at different RH conditions.

6. Sensitivity analyses of different membrane properties show that reducing the electro-osmotic drag coefficient or increasing the membrane water diffusivity can prevent significant cathode drying, thus, contributing to a more uniform water distribution in the membrane.

7. Lastly, increasing cathode CL ionic conductivity yields lower hydroxide transport loss and enhanced cell performance at high current densities.

The observations from these sensitivity studies provide valuable insights on the crucial parameters in designing and operating an AEMFC. This model provides a universal platform and is a useful tool to optimize material properties and tune operating conditions for achieving robust AEMFC operation.

Chapter 4

DEVELOPMENT OF RHEO-IMPEDANCE TOOL FOR ANALYZING CATALYST INK PROPERTIES AND MICROSTRUCTURE

4.1 Theory and Development of Rheo-Impedance Tool

Understanding how catalyst ink parameters affect ink properties and how ink components interact, and ultimately, their relationship with CL microstructure formation and cell performance, are essential to designing electrodes. There are a number of catalyst ink parameters that affect CL structure, namely, ionomer-to-carbon ratio (I/C), type and composition of solvent used, fabrication method, ionomer chemistry, type of catalyst and carbon support, and so on. This study proposes a new technique in investigating the interactions of ink components and the effect of processing on catalyst ink properties. The evaluation tool involves the combination of rheological and electrical measurements on the ink. The measurement data from simultaneous rheology and impedance measurements could provide insights into how the ink components interact and their effect on CL microstructure formation.

Catalyst ink slurry commonly prepared for rod coating has deformable and reconfigurable microstructure and can display mechanical properties between liquids and solids. Thus, it can exhibit nonlinear behaviors such as wall slip, macroscopic fractures, shear local dependencies, etc. [78]. The complex rheology of this type of fluid has been investigated using complementary local measurement tools like x-ray scattering [71, 104] and neutron scattering [105, 106] to gain insights on their microstructure evolution under shear.

Another tool used in studying microstructure is electrochemical impedance spectroscopy (EIS). EIS allows for the measurement of the electrical properties of the fluid such as conductivity and permittivity. When combined with rheological measurements (rheo-EIS), it can explain how the fluid microstructure evolves and rearranges with flow. Most studies using combined rheology and EIS measurement have been focused on fluids with carbon material additives and polymeric fluids [78, 107]. To date, regarding Pt/C catalyst inks for PEMFC application, rheo-EIS has only been used in one previous study from our group [108].

4.1.1 Rheo-EIS experimental set-up

There are different configurations in rheo-EIS electrode design. For a wired upper plate design, this allows for accurate impedance measurement, but since the upper shaft is directly wired, it limits the rotation of the equipment. Another configuration is through the use of a spring that connects the top shaft to the potentiostat. This allows the rheometer to rotate, however, the resulting friction due to the spring and inconsistent contact cause variation in the impedance signal. Another configuration uses in-plane electrode design [109]. This allows for full rotation of the equipment and the wired impedance measurement gives good data quality. However, since the bottom geometry is made up of two different materials, issues arise from differences in thermal conductivity, mechanical properties, chemical interactions, thermal expansion, and the ability to achieve uniform stress and strain distribution.

For this study, an in-house set-up is developed to simultaneously measure the rheology and impedance of catalyst ink samples. A schematic of the set-up is illustrated in Figure 4.1. The set-up is based on a modified NETZSCH Instrument standard rotational rheometer which consists of a top and bottom geometry that are electrically insulated from the rest of the rheometer body. The upper geometry is electrically connected to the bottom geometry through a liquid metal (Gallium Indium Eutectic, Sigma Aldrich) contained in the solvent trap attached to the shaft of the top geometry and a copper wire connected to the stationary bottom geometry. Electrical response is measured through the use of a potentiostat (CH Instrument 750E) connected to the top and bottom geometries. This setup allows for through-plane measurement of the electrical properties of fluid while allowing unlimited rotational range capability and full torque sensitivity of the rheometer.

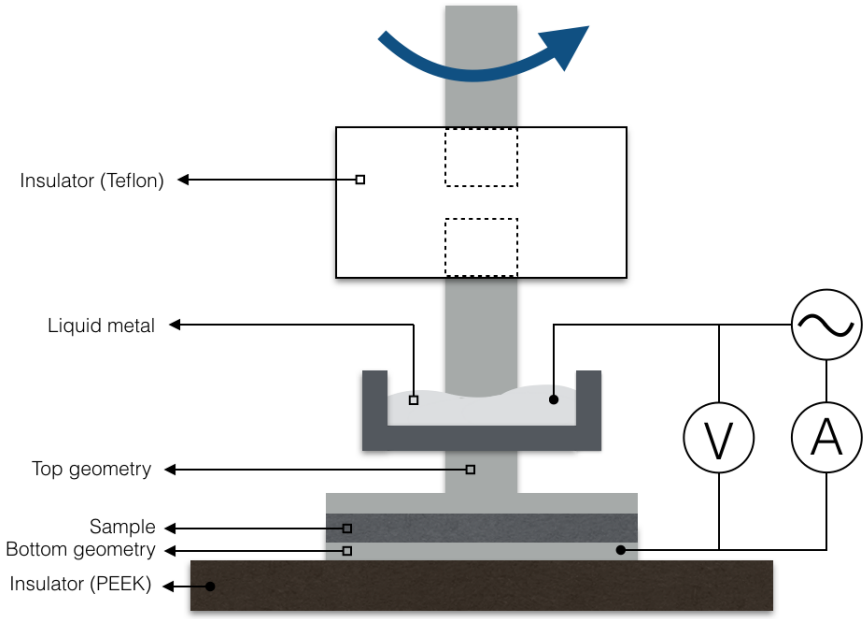

Figure 4.1: Schematic diagram of the rheo-EIS measurement set-up. The catalyst ink sample is sandwiched between parallel plates (dia = 4 cm) that serve as electrodes forming a closed circuit. The working gap is 0.25 mm. The solvent trap attached to the rotating shaft of the top plate contains liquid metal (EGaIn) to provide electrical contact. Adapted from Ref. [108]

4.1.2 Rheological and Electrical Calibrations

Before starting measurements, the instrument is calibrated to ensure the accuracy and precision of measurement data. First, the viscosity measurement of the set-up is calibrated using a standard calibration oil. The viscosity is measured for the desired range of shear rates. For comparison, the viscosity measured from the rheo-EIS parallel plate is compared to the measurement using a standard rheology parallel plate geometry (PLS40 S3901 SS). As observed in Figure 4.2, the rheo-EIS set-up provides a precise viscosity measurement for the tested range of shear rates and within acceptable deviation from the measurement using the standard rheometer geometry.

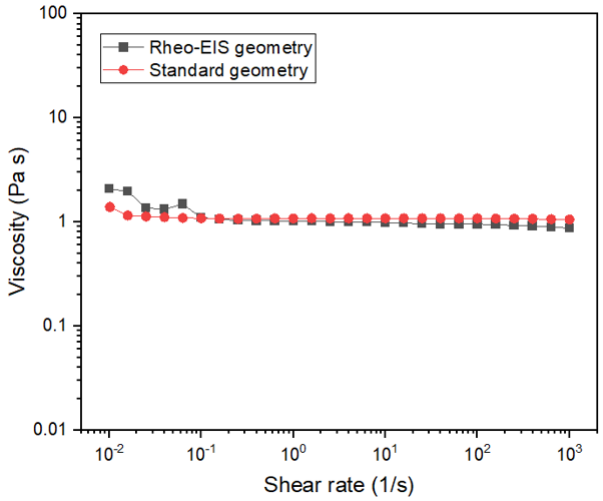

Figure 4.2: Result of viscosity measurement calibration for the in-house rheo-EIS set-up compared to measurement using the standard rheometer geometry. The standard oil used has 1.045 Pa s viscosity at 25 °C.

Next, the electrical measurements are calibrated by measuring the electrical response at closed and open circuit. The set-up impedance is measured from 0.1 Hz to 100 kHz at an amplitude of 50 mV. The result of the calibration is presented in Figure 4.3.

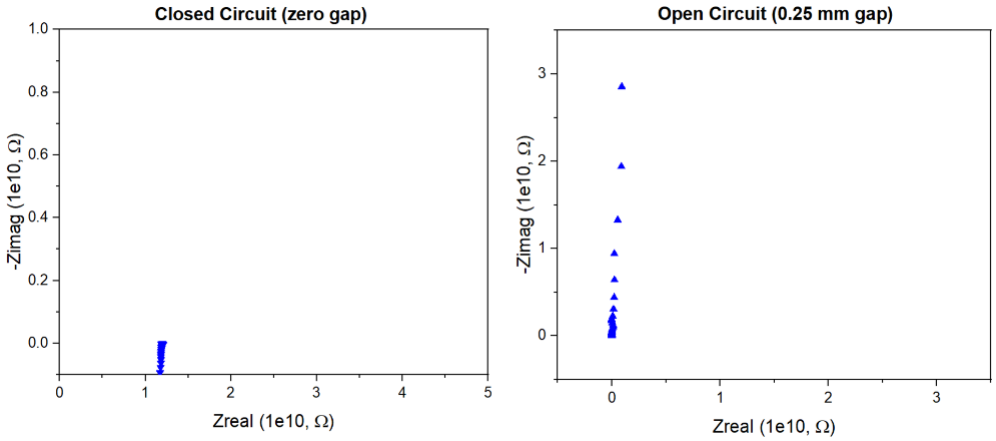

Figure 4.3: Open and closed circuit calibration of the rheo-EIS set-up. The AC impedance measurement is conducted without the sample. For closed circuit measurement, the gap is closed while reading the impedance response. For open circuit measurement, the gap is set to 0.25 mm.

Considering the instrument response can be characterized by a resistor element in series with the sample and a capacitor in parallel [110], the impedance measurement can be corrected using the following equation:

$$Z_{corr} = \frac{Z_s - Z_c}{1 - (Z_s - Z_c)/Z_o} \tag{4.1}$$

where Z_{corr} is the corrected impedance measurement, Z_s is the sample impedance, Z_c is the closed circuit measured impedance, and Z_o is the open-circuit measured impedance.

4.1.3 Rheo-EIS and Standard Rheological Measurement Protocols

To characterize the microstructure evolution of catalyst ink under shear, both rheo-EIS and standard rheological measurements were conducted. Prior to any measurement, the sample is pre-sheared at 1 s^{-1} followed by 1 minute of rest to allow for the removal of any shearing history. The type of tests employed and their corresponding rheometer and potentiostat settings are presented in Figure 4.4.

Seq.	Test	Rheometer setting	Potentiostat setting	Purpose
Rheo-EIS: Working gap = 250 µm, roughened parallel plate (dia. = 4 cm), solvent trap = EGaIn, 4-pt probe electrode measurement				
1	**Before shear**	Shear rate = 1 s^{-1}, 30 s Rest for 1 min	**AC impedance:** - 0.01 to 1e5 Hz - 50 mV amplitude - 0 Vdc	Steady-state ink properties at **pre-coating** condition
2	**After shear**	Shear rate = 500 s^{-1}, 100 s Rest for 1 min		Steady-state ink properties at **wet-film** (after coating) condition
3	**3 Phase Rebuilt @ 0.1 Hz**	Pre-shear: 1 s^{-1}, 30 s; Rest for 1 min **3 Phase Rebuilt sequence:** - 0.1 s^{-1}, 200 s - 500 s^{-1}, 100 s - 0.1 s^{-1}, 200 s	**Impedance – Time:** - 0.1 Hz - 50 mV amplitude - 0 Vdc	Dynamic ink properties **Before-during-after coating** Electrical resistance (low freq.)
4	**3 Phase Rebuilt @ 5k Hz**	Pre-shear: 1 s^{-1}, 30 s; Rest for 1 min **3 Phase Rebuilt sequence:** - 0.1 s^{-1}, 200 s - 500 s^{-1}, 100 s - 0.1 s^{-1}, 200 s	**Impedance – Time:** - 5000 Hz - 50 mV amplitude - 0 Vdc	Dynamic ink properties **Before-during-after coating** Ionic resistance (high freq.)
Standard rheology: Working gap = 250 µm, std. roughened parallel plate PLS40 S3901 SS (dia. = 4 cm), solvent trap = DI water				
5	**Standard Rheology**	Pre-shear: 1 s^{-1}, 30 s; Rest for 1 min Ramp-up: 0.01 to 1000 s^{-1}	N.A.	Catalyst ink flow behavior
6	**Amplitude sweep**	Oscillation at 1 Hz: 0.01 to 4000 shear strain	N.A.	Linear viscoelastic region (LVER)

Figure 4.4: Benchmark protocol for evaluating catalyst ink property using rheo-EIS measuring technique.

In order to get reliable and reproducible measurements, it is important to consider the material and colloidal stability of the catalyst ink. Material stability refers to the oxidation of the component due to Pt catalysis while colloidal stability

refers to the rearrangement of agglomerates due to Brownian motion [61]. Between the two, colloidal stability is more of a concern in this work due to the required measurement time frame. As such, it is critical to perform all measurements following the sequence outlined in Figure 4.4.

4.1.3.1 Before and After Shear Measurements

A full range frequency sweep from 0.01 Hz to 100 kHz EIS measurement is conducted after subjecting the sample to different shears. For the 'before' shear measurement, the sample is pre-sheared at 1 s^{-1} followed by 1 minute of rest. Then EIS measurements are collected at full frequency and at 50 mV amplitude and DC potential of 0 V. For the 'after' shear measurements, the sample is sheared at 500 s^{-1} followed by 1 minute of rest, then proceeded by EIS measurement using the same frequency range, amplitude, and DC potential. The resulting impedance spectra is fitted using the equivalent circuit model (ECM) in Figure 4.5. This ECM is the mechanical analog of the Jeffreys model in rheology used to describe the behavior of viscoelastic fluids [78].

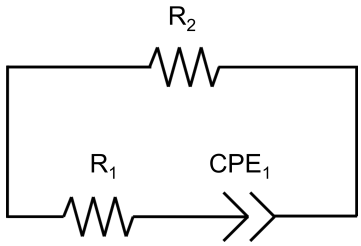

Figure 4.5: Equivalent circuit model used to represent the resistive and capacitive element of the catalyst ink.

In Figure 4.5, the resistive and capacitive elements, R_1 and CPE_1, represent the contribution of the ionic resistance of the ink, while the resistive element R_2 represent the electrical resistance of the ink. The ionic resistance refers to the dissolved H^+ in the sample while the electrical resistance is governed by the carbon agglomerate network.

4.1.3.2 Simultaneous Three-Phase Rebuilt

In order to study ink properties while simulating the coating process, a three-phase rebuilt test (3PRT) is conducted wherein the catalyst ink sample is sheared at different rates while simultaneous viscosity and electrical response are measured. The first phase of measurement involved shearing at 0.1 s^{-1} for 200 seconds to correspond to the pre-coating condition of the ink. The second phase involved shearing of

sample at 500 s^{-1} for 100 seconds to simulate the actual coating condition. Finally, the third phase which corresponds to the condition of the ink as wet film after coating, involved shearing at 0.1 s^{-1} for 200 seconds. All the while, the impedance of the sample is being measured under 50 mV amplitude, DC potential of 0 V, and at a single frequency. There are two (2) sets of three-phase rebuilt measurements conducted: one is at impedance measurement at 0.1 Hz and another at 5 kHz. The low frequency impedance measurement primarily probes the electrical resistance of the sample, while ionic resistance of the sample can be derived using the high frequency impedance measurement.

4.1.3.3 Standard Rheology and Amplitude Sweep

The standard rheological measurements were conducted using a standard roughened parallel plate geometry (40 mm diameter) with a 250 μm gap. A solvent saturation trap was used in order to minimize any solvent evaporation during measurements. To eliminate the effect of mechanical history from all the samples during measurements, all ink samples were sheared at 1 s^{-1} for 30 s and allowed to rest for 1 min. After the pre-shear process, the viscosity and shear stress were measured as shear rate was increased logarithmically from 0.01 to 1000 s^{-1}. For amplitude sweep tests, the shear strain was varied logarithmically from 0.1% to 100% at a fixed frequency of 1 Hz to measure the elasticity of samples.

4.2 Impact of Carbon Support Structure and Ionomer Loading on Pt/C Ink Properties

Carbon supports play a crucial role in CL structure. Apart from supporting the Pt nanoparticles, carbon supports can also affect overall performance. For example, supports with high specific area and porosity can promote uniform dispersion of Pt catalyst and increase proton transfer [58]. In addition, the characteristic porosity of carbon support and the location of Pt catalyst with respect to the pores affect gas transport, kinetics, and ECSA loss due to inhibited particle agglomeration [29]. Table 4.1 provides two types of Pt/C catalysts using different types of carbon support.

Table 4.1: Properties of different Pt/C catalyst

Parameter	TKK 46.8 wt% TEC10E50E	JM 40 wt% HiSPEC 4000
Carbon support type	Ketjen Black EC300J	Vulcan XC72R
Carbon support surface area (BET) [111]	800 m^2 g^{-1}	250 m^2 g^{-1}
Average pore size [112]	34 nm	50 nm
Platinum wt%	46.8 - 49.3	38.0 - 41.0
Pt particle size (XRD)	20 - 27 Å	max 45 Å

Ketjen black (KB) and Vulcan carbon (VC) are two of the most common commercially available carbon supports. KB is a high surface area carbon (HSAC) and has significant internal porosity compared to VC. As a result, most of the platinum on KB-supported catalysts reside in the internal pores, about 50% or more [61]. In contrast, platinum on VC-supported catalysts are mainly located on the external surface. Zhang et al. presented TEM images of Pt/C using different carbon supports at the same Pt loading (Figure 4.6) and they show that Pt particles on HSAC are slightly smaller than those on Vulcan [113]. This is consistent with the findings from Moriau et al. [111].

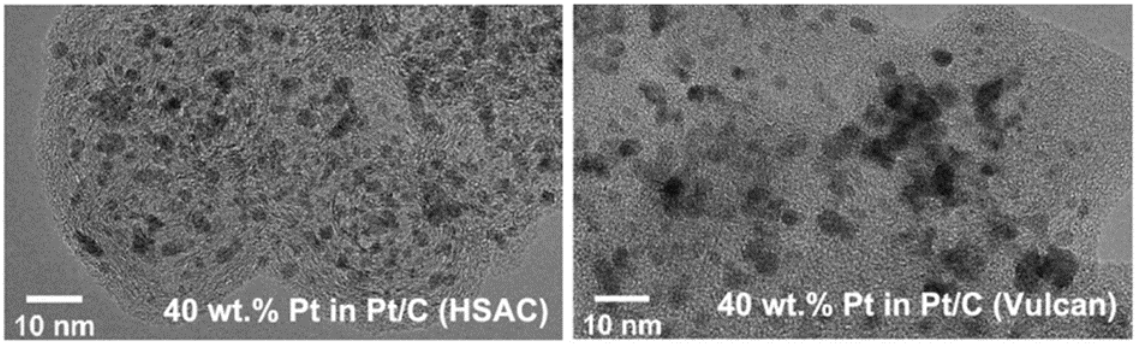

Figure 4.6: TEM images of 40 wt% Pt in Pt/HSAC and Pt/Vulcan from Ref [113].

4.2.1 Experimental Methods

4.2.1.1 Catalyst Ink Sample Preparation

Catalyst inks were prepared using previously reported procedure [108]. Specifically, 46.8 wt% Pt/C (TKK, TEC10E50E) catalyst powder and ionomer dispersion (20 wt% Nafion D2020, Ion Power Inc.) were dispersed in a mixture of 2-propanol (IPA) and deionized (DI) water. To study the impact of carbon support type, another batch of ink samples were prepared using 40 wt% Pt/C (Johnson Matthey, JM HiSPEC 4000) catalyst powder in place of TKK Pt/C powder. In addition, ionomer-to-carbon (I/C) were varied between 0.25 and 1.0. The prepared catalyst ink samples have a fixed carbon-to-solvent (C/S) mass ratio of 0.06 and IPA/W ratio of 0.30. The liquid and solid components were mixed in a container with eight 5-mm diameter Zirconia beads and loaded to a centrifugal mixer (AR-100 Thinky) at 2000 rpm for 3 minutes. Figure 4.7 shows the schematic representation of the different I/C and carbon support types that were investigated.

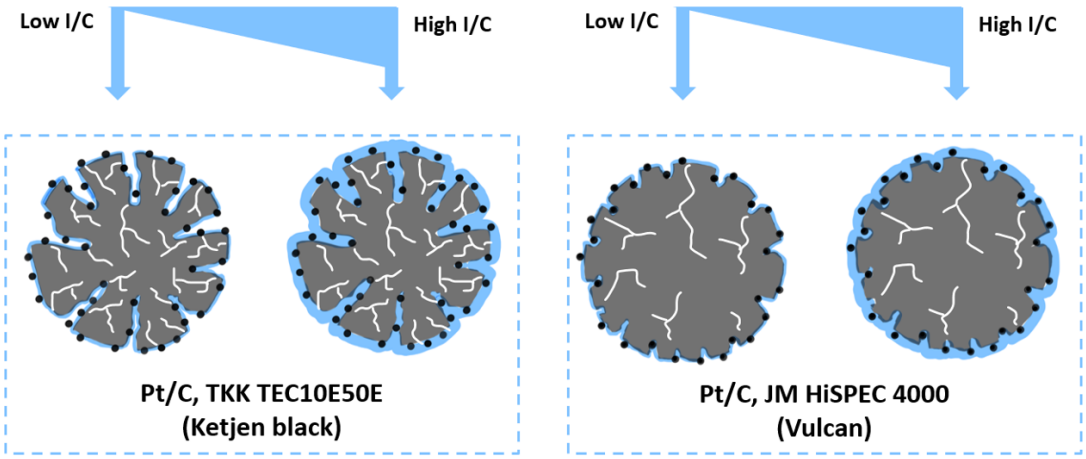

Figure 4.7: A representation of the different carbon support types and ionomer loading investigated.

4.2.1.2 Rheology and Rheo-EIS Measurement

Standard rheological and simultaneous rheo-EIS measurements were conducted to evaluate the macroscopic properties and get insights on the microstructure of the catalyst ink. The detailed procedure is outlined in Section 4.1.3. The measurements were conducted as soon as possible after preparing the catalyst inks to minimize measurement uncertainties due to the mechanical and colloidal instability of the inks.

4.2.2 Results and Discussion

4.2.2.1 Flow Curves

One way to study the mechanical properties of catalyst ink materials in flow is to examine their flow curves. The steady-shear rheological measurements of catalyst ink samples are shown in Figure 4.8.

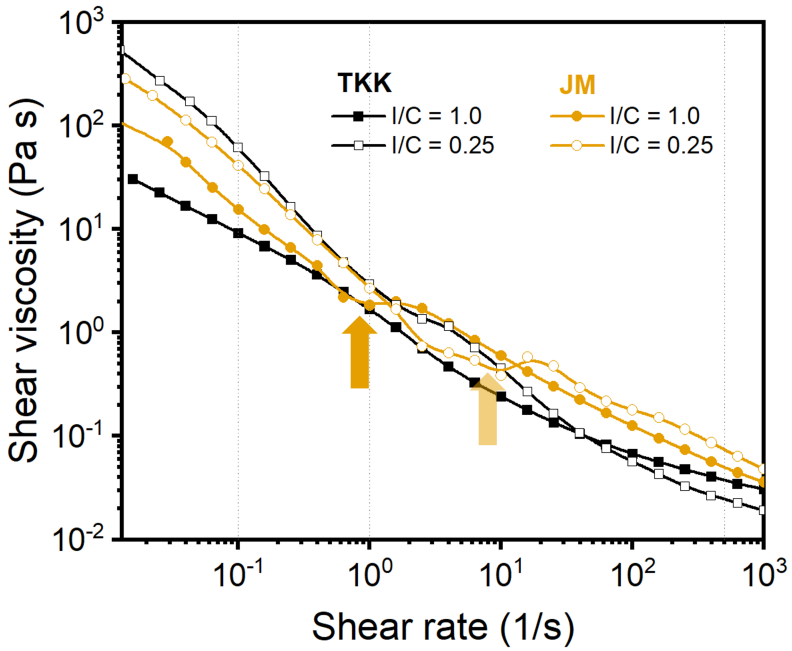

Figure 4.8: Flow curves of catalyst inks with TKK and JM Pt/C using I/C = 0.25 and I/C = 1.0. The arrow denotes shear-thickening region.

All the Pt/C ink samples studied exhibited shear-thinning behavior (an increase in shear rate reduces the viscosity under shear stress) which is expected for agglomerating suspensions. The steep drop in viscosity at low shear rate region is due to the breakdown of weakly connected particle agglomerates and their alignment with flow direction [114]. Interestingly, there is an observed plateau (or shear-thickening) region at intermediate shear for JM Pt/C inks containing Vulcan carbon. This behavior has been observed in previous studies [108, 115, 116]. For JM Pt/C inks at intermediate shear rates, a further increase in shear rate results in carbon particles gaining sufficient velocity in the presence of hydrodynamic forces. This promotes collision among particles and results in reagglomeration. The onset of this shear-thickening occurs at a lower shear rate (about 0.8 s^{-1}) when I/C = 1.0 and shifts to a higher shear rate (about 10 s^{-1}) for I/C = 0.25. This result indicates that

increasing the ionomer facilitates the breakdown of agglomerates, thereby increasing the hydrodynamic volume and promoting further cluster formation [108]. For TKK Pt/C inks with KB, this shear thickening behavior is not apparent and weak. According to Youssry et al., this is due to the relatively small and monodisperse hydroclusters resulting in stronger particle interaction [115].

4.2.2.2 Rheo-EIS Measurement

A full frequency range EIS measurement was conducted on stationary samples to understand the Pt/C catalyst ink resistance before and after the application of high shear. The Nyquist plot generated from the impedance data for all samples is shown in Figure 4.9(a) and (b). The calculated electrical resistance using the equivalent circuit model in Figure 4.5 is also shown in Figure 4.9(c). Most of the samples showed an increase in electrical resistance after the application of high shear (500 s^{-1}) except for JM Pt/C with I/C = 0.25. This is consistent with the findings of Mehrazi et al. [108]. At this low ionomer-to-carbon (I/C) ratio, the Johnson Matthey (JM) Pt/C agglomerates form a robust percolated network after shear. For both TKK and JM Pt/C ink samples, the overall electrical resistance is higher at high I/C ratios compared to low I/C ratios due to increased ionomer coverage on the Pt/C. This increase in resistance is particularly significant for TKK Pt/C catalyst ink. Despite having similar Pt loading, JM Pt/C with Vulcan carbon support has more Pt on the external surface, as Vulcan has fewer internal pores than Ketjen black. Consequently, TKK Pt/C ink has a more exposed carbon surface. Additionally, a previous study [45] has shown that ionomers preferentially adsorb on carbon surfaces, resulting in greater ionomer coverage on TKK Pt/C inks at high I/C ratios.

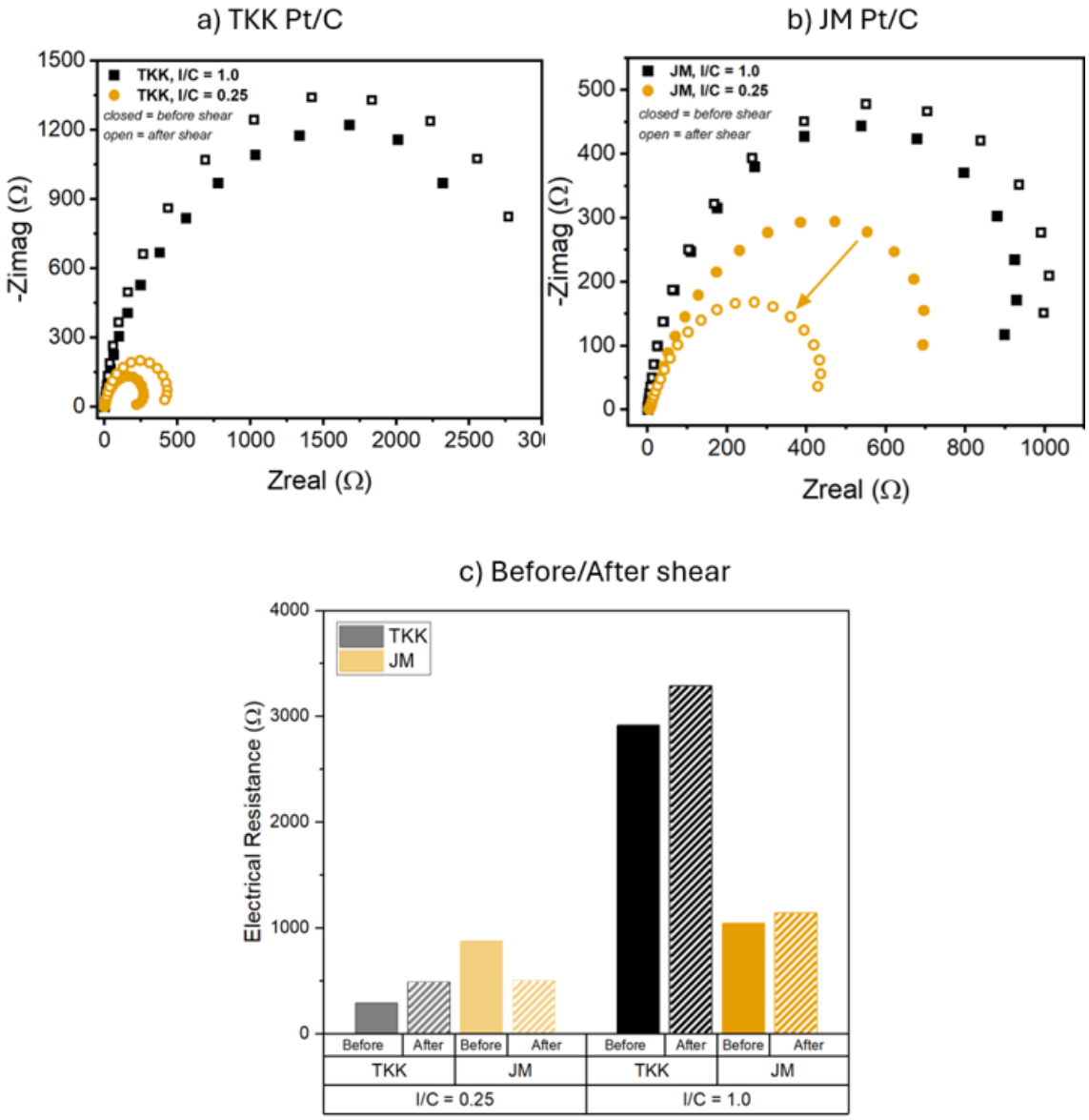

Figure 4.9: Nyquist plot from the EIS measurement from 0.01 Hz to 100 kHz before and after application of high shear for (a) TKK Pt/C ink and (b) JM Pt/C ink. (c) Estimated electrical resistance from EIS measurement.

In order to study the impedance behavior and thixotropy of ink during the coating process, a three-phase rebuilt test (3PRT) was conducted. Impedance characteristics of ink provide an insight into the evolution of microstructure, particularly Pt/C and ionomer interactions. On the other hand, thixotropy informs how the ink viscosity vary with time as a result of shear [74]. Selection of ink with suitable thixotropic properties is essential since it enables uniform thickness in the catalyst

layer (CL). In the 3PRT, it is assumed that formation of CL from catalyst ink consists of three steps: (1) ink is at static state under low shear, (2) ink undergoes high shear during coating process, and (3) ink is at recovery stage and returns to low shear after coating. Results from the tests are shown in Figure 4.10.

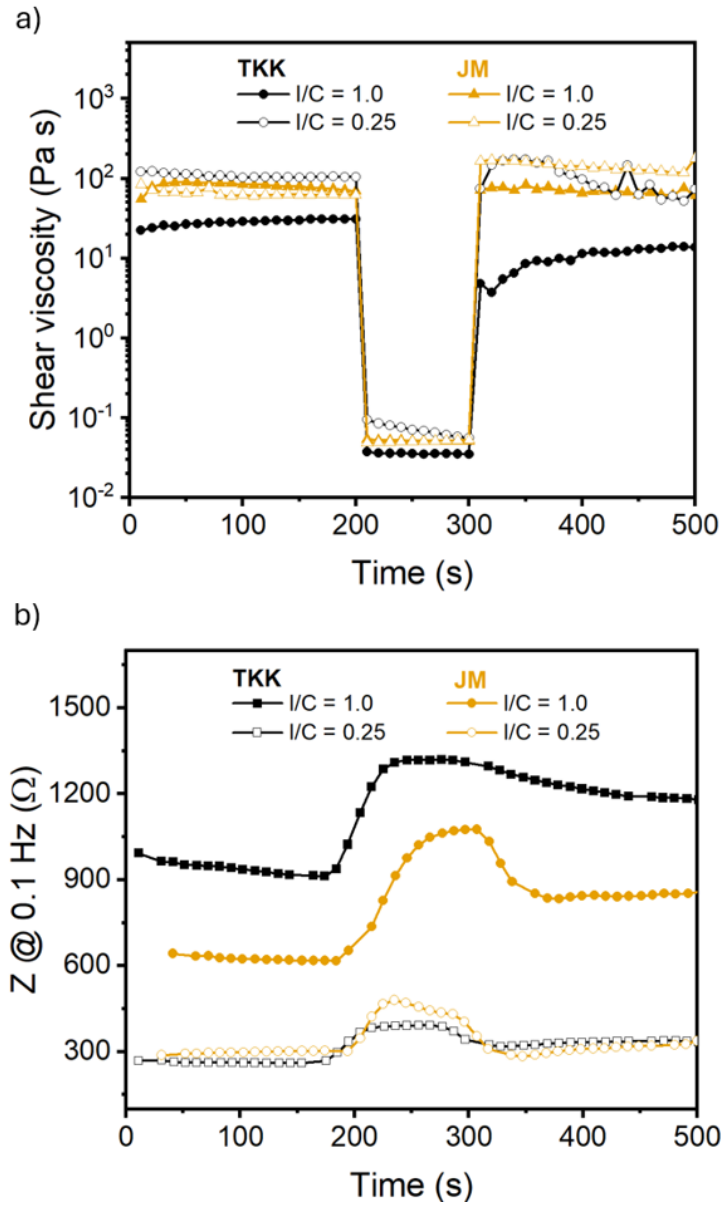

Figure 4.10: Three-phase rebuilt measurement showing the (a) thixotropy and (b) impedance behavior of Pt/C inks with different ionomers.

The trend of viscosity measurements during the first and second phases was

consistent with the flow curves in Figure 4.8. Similarly, the trend of impedance measurement during the first and third phases was consistent with the (static) before and after measurements shown in Figure 4.9. Note that for the 3PRT, impedance measurements were taken during shear, albeit at a low shear rate (0.1 s^{-1}). In contrast, for the before and after shear tests, the impedance measurement was taken after shear, when the sample was at rest. Without shear, particle interactions through Brownian movement are mostly random and isotropic. However, with shear, this motion becomes aligned with the direction of the shear. At high I/C ratios, this directional motion promotes ionomer coverage on the carbon surface hence the pronounced increase in impedance at the third phase in Figure 4.10(b) for I/C = 1.0 for both samples. During high shear, the ink internal structure is destroyed and the sample viscosity decreases. At this stage, shear force is greater than the attractive forces between agglomerates in the inks (i.e., van der Waals, polar bonds, and hydrogen bonds) which caused the drastic drop in viscosity [117]. This is also evident in the increase in the measured impedance for all samples during the second phase. During the third phase, all JM Pt/C ink samples not only fully recover the original microstructure but even formed a more compact agglomerate structure. For TKK Pt/C ink with I/C = 1.0, it can be seen that the increase in ionomer loading significantly hindered the carbon-carbon particle interaction. This was evident in the viscosity and impedance measurement during third phase.

4.3 Impact of Solvent Formulation on Pt/C Ink Properties

The primary role of solvents in Pt/C catalyst inks is to create dispersion of the catalyst nanoparticles and ionomer. Although solvent evaporates completely and is not present in the final CL microstructure, it has a significant impact on the microstructure and macroproperties of ink and thus the CL microstructure. Solvent properties such as viscosity, dielectric constant (ε), boiling point, etc. control the deposition process and inform how the ionomer and catalyst particles interact with each other. In particular, the amount of ionomer adsorbed onto Pt/C particles and their morphology depend on the type and formulation of solvent. In water-rich environment, Nafion presents as rod-like colloidal clusters with their PTFE backbone as core and the sulfonate groups as shell and Nafion backbone tends to adsorb onto carbon surface because of the hydrophobic interactions [118]. In alcohol-rich solvents, Nafion has a reverse micelle structure, and the ionomer backbone is preferentially oriented toward the bulk solvent [71].

Mixtures of water with IPA or NPA are the most common although the formulation is not standardized. Depending on the composition, properties such as dielectric constant can vary. The dielectric constant of the solvent is related to its polarity and its ability to separate opposite charges.

4.3.1 Experimental Methods

4.3.1.1 Catalyst Ink Sample Preparation

The catalyst ink preparation was similar to Section 4.2.1.1. Specifically, 46.4 wt% Pt/C (TKK, TEC10E50E) catalyst powder and Nafion ionomer (20 wt%, D2020) were dispersed in a mixture of IPA and deionized (DI) water (IPA/W). To study the effect of solvent formulation, IPA/W ratio is varied from 1/3, 1.0, and 3.0. The prepared catalyst inks both have fixed ionomer to carbon (I/C) mass ratio of 1.0 and carbon to solvent (C/S) mass ratio of 0.06. The liquid and solid components were mixed in a container with eight 5-mm diameter Zirconia beads and loaded to a centrifugal mixer (AR-100 Thinky) at 2000 rpm for 3 minutes. The catalyst ink samples studied in this work is listed in Table 4.2.

Table 4.2: Pt/C catalyst ink samples with different solvent formulation. Sample names (Low, Medium, High) denote level of IPA/W ratios.

Sample name	DI water (g)	IPA (g)	IPA/W
Low	3.20	1.07	1/3
Medium	2.13	2.13	1.0
High	1.07	3.20	3.0

The resulting ε of the solvent was calculated according to Equation 4.2 and Equation 4.3 using the ε of pure substances listed in Table 4.3.

Table 4.3: Dielectric constant of pure substances

Component	Dielectric constant, ε	Ref.
H_2O	78.4	[119]
IPA	18.3	[120]

Note that the ε of the resulting solvent should take into account the existing solvent in Nafion solution. The total mass of each is listed in Table 4.2. The mixed solvent ε was calculated according to Equation 4.2 [74].

$$\varepsilon_m = \left[\frac{\rho_m}{(\sum x_i M_i)}\right]^2 \tag{4.2}$$

where ε_m is the dielectric constant of the mixed solvent, x_i is the molar fraction of component i, M_i is the molecular weight of component i, and ρ_m is the molar

dielectric polarization of the mixed solvent, which is calculated using Equation 4.3 [74].

$$\rho_m = \sum x_i \rho_i = x_i \varepsilon_i^{1/2} M_i \tag{4.3}$$

where ρ_i is the molar dielectric constant of solvent i.

4.3.1.2 Rheology and Rheo-EIS Measurement

Standard rheological and simultaneous rheo-EIS measurements were conducted to evaluate the macroscopic properties and get insights on the microstructure of the catalyst ink. The detailed procedure is outlined in Section 4.1.3. The measurements were conducted as soon as possible after preparing the catalyst inks to minimize measurement uncertainties due to the mechanical and colloidal instability of the inks.

4.3.1.3 Dynamic Light Scattering and Zeta Potential Measurement

Dynamic light scattering (DLS) and zeta potential measurements were performed using a Malvern Zetasizer Nano ZS (Malvern Panalytical Ltd). The catalyst inks were diluted to 0.01 wt% using the same solvent formulation as the original ink samples and sonicated before analysis to avoid multiple scattering and improve the quality of DLS measurements. A small portion of the diluted catalyst ink was transferred into a dip cell (ZEN1002) for analysis. All tests were done at 25°C. At least three readings were taken to ensure the repeatability of the measurements.

4.3.2 Results and Discussion

4.3.2.1 Zeta-Potential and DLS

The ζ-potential of different ink samples was measured to understand the relative electrostatic stability of Pt/C particles with different solvent formulations. The calculated ε values of the mixed solvent are 29, 43, and 59 for IPA/W of 3.0, 1.0, and 1/3, respectively. The dielectric constant increases with increasing water content since water is the more polar solvent compared to IPA. Results of the ζ-potential measurement presented in Figure 4.11(a) show that all samples have large negative ζ-potential, indicating strong electrostatic repulsion. Dissociation of the sulfonate group (-SO_3H) of the Nafion side chain is influenced by the solvent's dielectric constant, ε. A solvent with high ε (i.e., water-rich) promotes -SO_3H dissociation and increases charge density on the surface of the ionomer particles, thereby leading to more negative ζ-potential [119]. This is clearly evident by the large negative ζ-potential of the Low IPA/W sample with water-rich solvent. The

trend is consistent with High and Medium samples - with increasing solvent ε, the magnitude of ζ-potential increases.

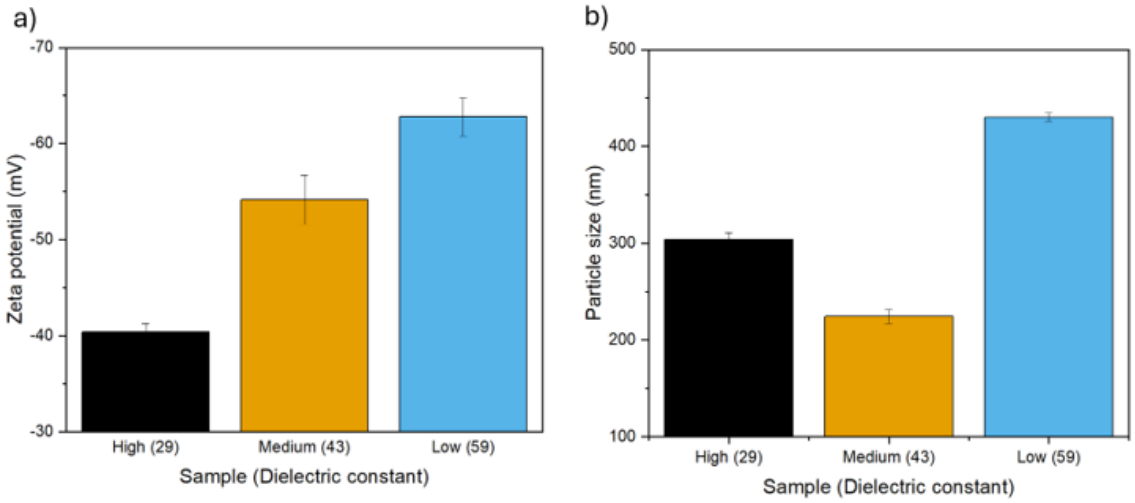

Figure 4.11: (a) Zeta Potential and (b) particle size measurement of Pt/C ink samples with different solvent formulations. The dielectric constant is listed inside the parenthesis following the sample name.

Meanwhile, there is no noticeable trend in particle or aggregate size measurement as shown in Figure 4.11(b). Previous studies have shown that an increase in the dielectric constant of solvent causes the ionomer molecules to dissociate the negatively charged -SO_3^- groups from -SO_3H groups [59] and increase in the negative charge on the catalyst agglomerates [74]. Consequently, the increase in electrostatic repulsion between particles reduces the size of the catalyst agglomerate. This is the trend for the High and Medium samples. However, the particle size measured for the water-rich (Low) sample significantly increased relative to the other two. Further increase in the water content of the solvent may tend to promote larger Pt/C aggregates, hence the shift to larger particle size. In this case, secondary aggregates form through interconnected primary aggregates as evidenced by the bimodal peak in the particle size distribution (Figure B.1). This is also observed in a previous study [121].

4.3.2.2 Catalyst Ink Viscosity

Results in the variations in viscosity with shear rate are presented in Figure 4.12. The Pt/C ink samples across all three solvents showed shear-thinning behavior. This indicates that agglomerates were broken down with increasing shear rates. At low shear rates (<0.1 s^{-1}), there is small variation in viscosities. However, at high

shear rates (>10 s^{-1}), the variation is noticeable, particularly for the water-rich sample. Notably, the trend in viscosity measurement across all three samples is similar to the trend observed from the measured particle size from DLS as seen in Figure 4.11(b). This implies that smaller particles promote a higher surface area that leads to an increase in viscosity due to enhanced particle-solvent interaction [119, 122]. We also found evidence of shear-thickening behavior at intermediate shear rates. This is more pronounced with IPA-rich solvent and weaker with increasing water content in the solvent.

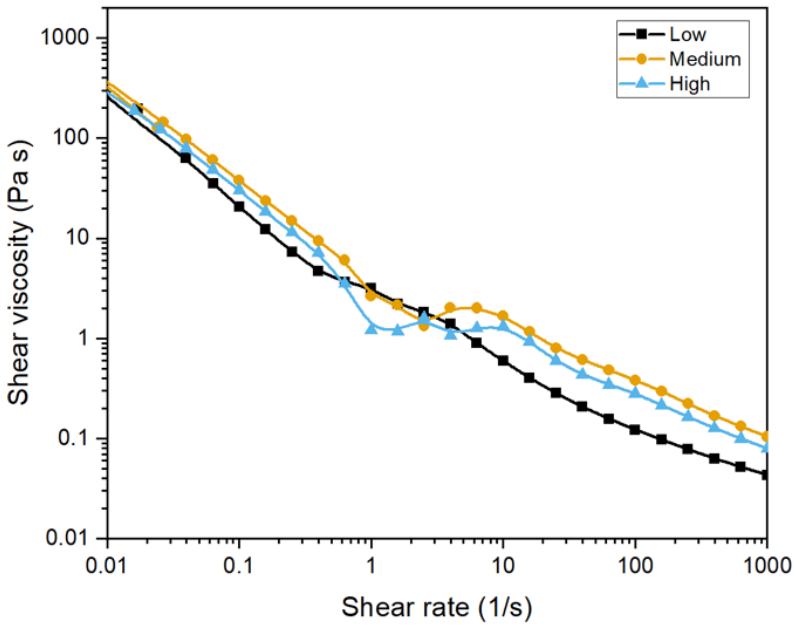

Figure 4.12: Flow curve of Pt/C ink samples with different solvent formulations.

4.3.2.3 Rheo-EIS Measurement

To be able to study how microstructure in Pt/C catalyst ink evolves with shear, rheo-EIS measurement is conducted. The impedance measurement before and after high shear application is shown in Figure 4.13(a) and the estimated electrical and ionic resistances based on the ECM (Figure 4.5) fitting are presented in Figure 4.13(b) and (c), respectively. Comparing Figures 4.13(b) and (c), we see that the Pt/C catalyst ink is predominantly ionic conductive and that ionic resistance measurements are relatively the same for all samples. Meanwhile, the electrical resistance measurements before and after the application of high shear follow the same trend, i.e., Medium < High < Low. Electrical resistance is controlled by the network structure established from carbon-carbon contacts. Conformation of adsorbed ionomer can either increase or decrease electrical resistance depending on the type

of surface interaction it promotes. At water-rich solvents, Nafion presents as rod-like particles with the hydrophilic groups preferentially oriented at the bulk solvent. With alcohol-rich solvent, Nafion exists as coil-like particles with the hydrophobic backbone oriented toward the bulk solvent [59, 71].

The rod-like micelle Nafion configuration present in a water-rich environment provides more surface area coverage onto the Pt/C surface thereby disrupting carbon-to-carbon contacts and increasing the electrical resistance as evident in Low sample before and after applying high shear. Compared with Low sample, there is less electrical resistance for High sample before shear. However, after the application of high shear, their electrical resistance values are about the same. With shear, the coil-like conformation of Nafion at IPA-rich solvent changes such that the coil unravels to cover more of the carbon surface effectively providing as much surface area coverage as that of rod-like micelle Nafion conformation. For the intermediate sample, Medium, the electrical resistance values measured before and after shear are small indicating that there is a strong carbon-carbon network formed. This is supported by the high viscosity measurement from the steady shear flow curve (Figure 4.12) indicating strong particle interaction that provides resistance to flow.

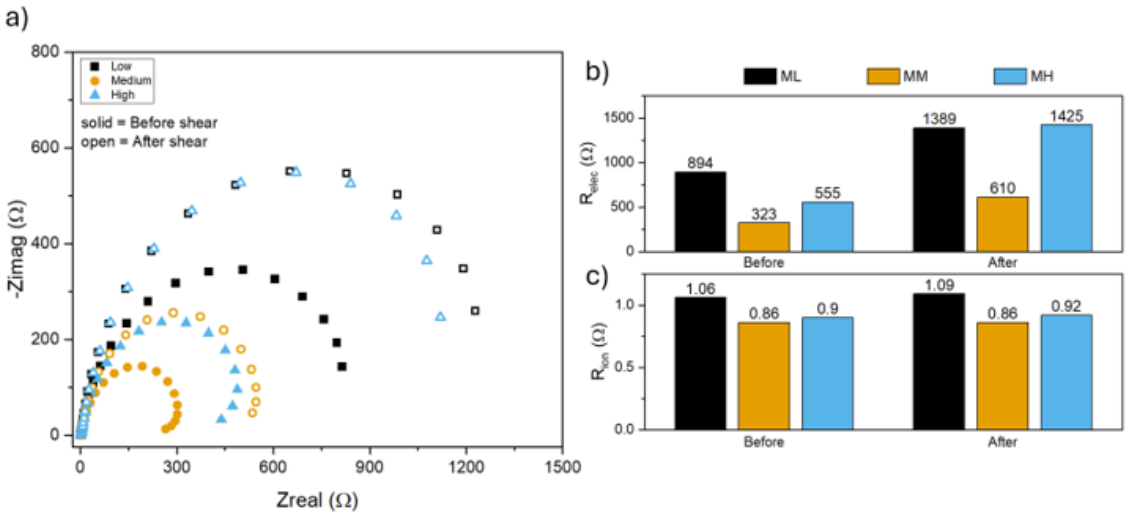

Figure 4.13: Before and after shear impedance measurement of Pt/C inks with different solvent formulations. (a) Nyquist plot, (b) electrical resistance, and (c) ionic resistance measurements.

In addition, the ink properties and microstructure evolution are studied using rheo-EIS measurement under transient conditions by applying the three-phase rebuilt measurement (3PRT). This measurement allows for probing ink conditions that simulate the rod coating process. In the first phase, ink is kept at 'storage'

conditions. The second phase provides conditions in which ink undergoes an actual high-shear coating process. Finally, during the third phase, the recovery period, the ink returns to stationary condition. The measured viscosity and impedance values from simultaneous three-phase rebuilt are shown in Figure 4.14(a) and (b), respectively.

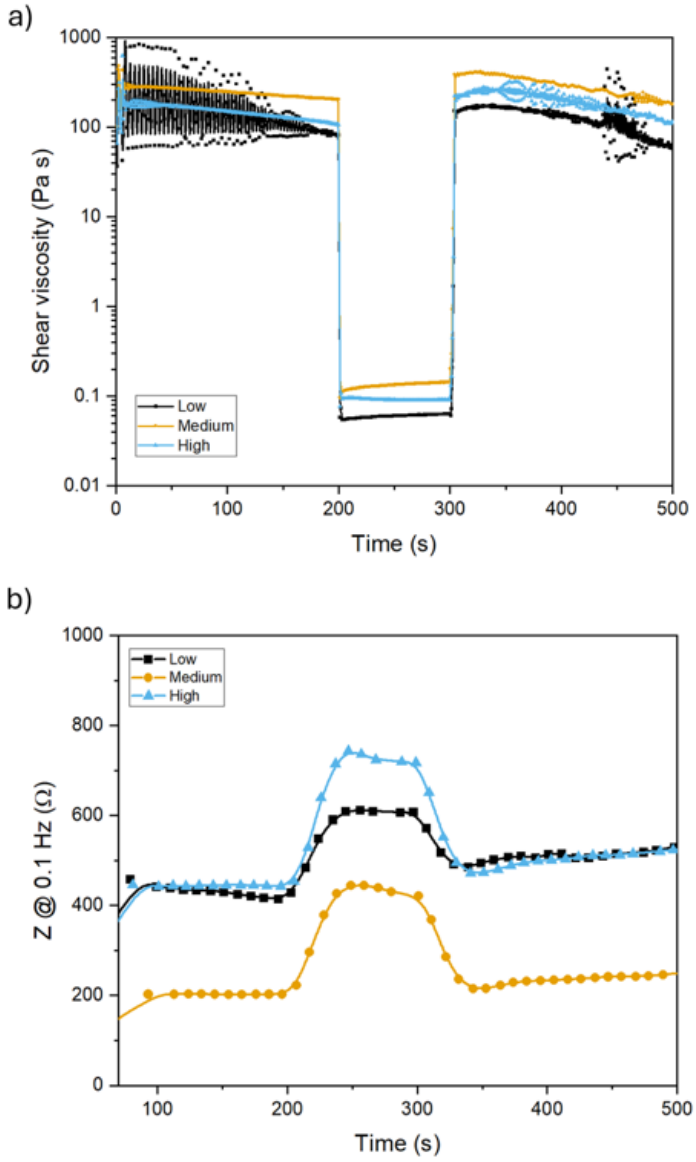

Figure 4.14: Simultaneous three-phase rebuilt measurement of Pt/C catalyst inks with different solvent formulations: (a) Viscosity measurement, and (b) impedance measurement at 0.1 Hz.

Comparing viscosity values from the flow curve in Figure 4.12, the measured viscosity trends at the first and second phases were consistent with that of Figure 4.12. Although there were fluctuations in the measured viscosity of Low sample in the first phase, it generally remained the least viscous sample owing to its highest hydrodynamic particle size from DLS measurement. The Medium sample remained the most vicious among all three samples during all three phases. Notably, all samples have recovered their microstructure and have even formed a stronger carbon-carbon particle interaction as their viscosities at the third phase after cessation of high shear were even higher than their viscosities at the first phase [108].

Consistent with the stationary impedance measurement from the before and after shear test (Figure 4.13), the Medium sample has the lowest impedance measured at 0.1 Hz which mainly probes electrical resistance. Upon application of high shear, agglomerates break into primary aggregate which results in a drop in viscosity and a rise in impedance measurement since the electron conducting network is essentially disrupted. Across all samples, there is an increase in measured impedance from the first phase to the third phase measurement. This is consistent with the trend in the before and after shear measurements. While there is a noticeable difference in the impedance values between Low and High samples before applying shear (Figure 4.13(b), during 3PRT, the measured impedance at the first phase for Low and High samples are relatively similar. This is because the sample was under shear during impedance measurement at 3PRT, albeit low at the first phase. The applied shear at this stage was enough to modify the ionomer-catalyst interaction, particularly in unraveling the coil-like Nafion ionomer conformation in an IPA-rich environment for the High sample.

4.4 Summary

In summary, we developed an in-house measurement tool to study Pt/C catalyst ink properties and microstructure evolution with shear. This tool utilizes simultaneous measurement of rheology and impedance to be able to provide insight into the component interaction present in catalyst ink samples on a given condition and using different ink formulations. We also designed a measurement protocol that elucidates steady state and dynamic properties that are critical in understanding structure breakdown and recovery during the ink coating process.

The rheo-EIS measurement technique was demonstrated in the study of the impact of carbon support type, ionomer loading, and solvent formulation on the macroproperties and microstructure of Pt/C catalyst ink. When combined with other ink characterization tools such as DLS for ζ-potential and particle size measurement, catalyst component interaction can be studied more closely. The effect

of carbon support type has been demonstrated to be significant in terms of catalyst ink viscosity and microstructure as informed by impedance value for high ionomer loading (I/C = 1.0). This is particularly important when tailoring ink properties for a specific coating condition to attain good leveling and enough wet film thickness. The study also showed that solvent formulation affects agglomerate size and therefore viscosity and impedance measurement. The most common solvent type for the Pt/C catalyst ink system is a mixture of water and alcohol (i.e., IPA in this study). Equal parts water and IPA have resulted in ink that provides a strong carbon agglomerate network and stable and good recovery after coating.

Chapter 5

EFFECT OF HIGH OXYGEN PERMEABILITY IONOMER ON INK PROPERTIES AND ELECTRODE STRUCTURE AND PERFORMANCE

5.1 Introduction

The ionomer is a critical component of a catalyst layer. It promotes proton conductivity, binds the Pt/C particles together, and provides mechanical stability during CL processing and MEA operation. Recently, there have been several studies on high oxygen permeability ionomer (HOPI) for PEMFC application with evidence of improved performance [62, 123, 124]. Most of these studies have concentrated on the performance of the MEA during operation with improvements owing to the promotion of the local oxygen and proton transport properties. However, to advance the design of CL, further understanding of the role of HOPI in overall catalyst ink property and processing is necessary. In this work, we investigate the influence of HOPI ionomer on the Pt/C catalyst ink property and microstructure and compare it with the benchmark D2020 ionomer.

5.2 Experimental Methods

5.2.1 Sample preparation

Catalyst inks were prepared using previously reported procedure [1]. Specifically, 46.4 wt% Pt/C (TKK, TEC10E50E) catalyst powder and ionomer were dispersed in a mixture of alcohol and deionized (DI) water (alcohol:DI = 0.923). Two different ionomers were investigated: Nafion (20 wt%, D2020) and HOPI (10 wt%, Chemours). For inks with Nafion, 2-propanol is used as alcohol solvent, whereas 1-propanol is used for HOPI similar to their respective stock solutions. The prepared catalyst inks both have fixed ionomer to carbon (I/C) mass ratio of 0.8 and carbon to solvent (C/S) mass ratio of 0.06. To study the effect of carbon-solvent interaction, another ink with Nafion ionomer is prepared with C/S of 0.08. The liquid and solid components were mixed in a container with eight 5-mm diameter Zirconia beads and loaded to a centrifugal mixer (AR-100 Thinky) at 2000 rpm for 3 minutes.

Table 5.1: Catalyst ink formulation using D2020 and HOPI ionomer for rheo-EIS measurement

Sample name	C/S	Pt (g)	Carbon (g)
D2020 (6%)	0.06	0.483	0.26
D2020 (8%)	0.08	0.615	0.33
HOPI (6%)	0.06	0.483	0.26

5.2.2 DLS and zeta potential measurements

Dynamic light scattering (DLS) and zeta potential measurements were performed using a Malvern Zetasizer Nano ZS (Malvern Panalytical Ltd). The catalyst inks were diluted to 0.01 wt% using solvent (alcohol:DI = 0.923) and sonicated prior to analysis to avoid multiple scattering and improve the quality of DLS measurements. A small portion of the diluted catalyst ink was transferred into a dip cell (ZEN1002) for analysis. All tests were done at 25°C. At least three readings were taken to ensure the repeatability of the measurements.

5.2.3 Rheology and rheo-EIS measurement

Rheology and rheo-EIS measurements were performed using a rotational rheometer equipped with temperature controller (Kinexus Prime ultra+, NETZSCH) with some modifications as described in Chapter 4. Notably, for conducting simultaneous rheology and impedance measurements, the roughened top and bottom plate geometries were electrically insulated from the rest of the rheometer body. The electrical connection between top and bottom plate was established through a stainless-steel needle dipped in liquid metal (Gallium Indium Eutectic, EGaIn, Sigma Aldrich) contained in the solvent trap at the top plate and wires connected to the bottom plate. A potentiostat (CH Instrument 750E) was used to measure impedance. All samples were tested at 25°C. The detailed measurement protocol is discussed in Chapter 4.

5.2.4 Scanning electron microscopy

The morphology of the catalyst layer on the catalyst-coated membrane (CCM) was characterized using a scanning electron microscope (Zeiss Gemini). The imaging was performed on the side of the PTFE decal, i.e., after hot pressing the decal against Nafion membrane such that the images represent the surface facing the membrane in the cell assembly.

5.2.5 MEA preparation and fuel cell test

Pt/C catalyst ink samples with different ionomers were used as cathode in a membrane electrode assembly (MEA). The inks were coated onto a virgin PTFE substrate with the desired loading and thickness using a Mayer rod coater. For anodes, a standard catalyst ink recipe was used with D2020 as ionomer and Pt loading of 0.10 mg_{Pt} cm^{-2}. The coated CLs were dried under ambient conditions before the decal transfer. Using the hot-press method, the CLs were transferred onto Nafion NC700 membrane (Chemours, USA) under 130 °C and 300 psi for 5 mins.

Table 5.2: Catalyst ink formulation using D2020 and HOPI ionomer for MEA testing

Sample name	I/C	C/S	alcohol/W[a]	Pt loading[b]
D2020	0.85	0.06	1.5	0.214
HOPI	0.80	0.06	0.92	0.221

[a] For alcohol, IPA is used for D2020 while nPA is used for HOPI ink sample.
[b] in mg_{Pt} cm^{-2}

For the fuel cell assembly, Toray TGP-H-060 was used as gas diffusion layer (GDL) with PTFE gasket for sealing and compression stop, yielding a GDL strain of approximately 20%. The performance of the fabricated MEAs were evaluated using a cell with straight parallel flow channels and an active area of 2 cm^2 in an automated Greenlight G20 fuel cell test station. To evaluate the ohmic resistance of the cell, high frequency resistance (HFR) was measured via EIS using Gamry Reference 3000 coupled with a Gamry 30k booster.

To measure the electrochemically active surface area (ECSA), cyclic voltammetry (CV) was performed under H_2/N_2 environment using 50 mV/s scan rate. Break-in protocol was conducted to activate the CLs by cycling the voltage between open circuit voltage (OCV), 0.40, 0.60, 0.70, and 0.85 V for 16 cycles. After break-in, a series of tests listed in Table 6.2 were conducted to evaluate performance under dry and wet conditions. Limiting current tests were used to evaluate oxygen transport resistance under dry and wet conditions. Proton transport resistance in the membrane and cathode CL was evaluated via EIS under H_2/N_2 environment at different RH.

Table 5.3: Fuel cell test protocol for MEA with different ionomer types (D2020 and HOPI)

Test	Temp. (°C)	RH (%)	Press. (kPaa)	Voltage (V)
CV	30	100	100	0.05 - 1.2
Break-in	70	100	150	OCV - 0.40
Dry lim. i	80	64	100 - 300	0.30 - 0.09
Wet lim. i	70	80	300	0.30 - 0.09
Dry i-V	70	60	100	OCV - 0.20
Wet i-V	70	100	300	OCV - 0.20
Sheet resistance	70	40 - 100	300	0.20 (10mV AC)

5.3 Results and Discussion

5.3.1 Zeta-potential and DLS

The ζ-potentials of different catalyst ink samples are measured to understand the relative electrostatic stability of Pt/C particles with different ionomers. Results of the ζ-potential and agglomerate size measured by DLS (Figure 5.1) showed that all samples have large (negative) ζ-potentials indicating strong electrostatic repulsion. Both Nafion and HOPI ionomers have (negative) charged sulfonic groups. However, HOPI has a shorter side chain length and an additional ring-structure attached to the polymer backbone that could alter ionomer adsorption. The catalyst inks with Nafion ionomer (both with C/S of 6% and 8%) have slightly larger ζ-potential compared to ink with HOPI which resulted to smaller agglomerate size. This is indicative of a more stable particle and increased electrostatic repulsion following the adsorption of the ionomer [47]. On the other hand, catalyst ink with HOPI ionomer measured a slightly higher agglomerate size than Nafion counterpart. According to previous studies, ionomers adsorbed on the agglomerates can increase the agglomerate size through the combined effect of the Debye length and the thickness of the adsorbed ionomer [125]. The ring-structured matrix present in HOPI ionomer could have reduced the electrostatic repulsion and in turn promoted particles to aggregate.

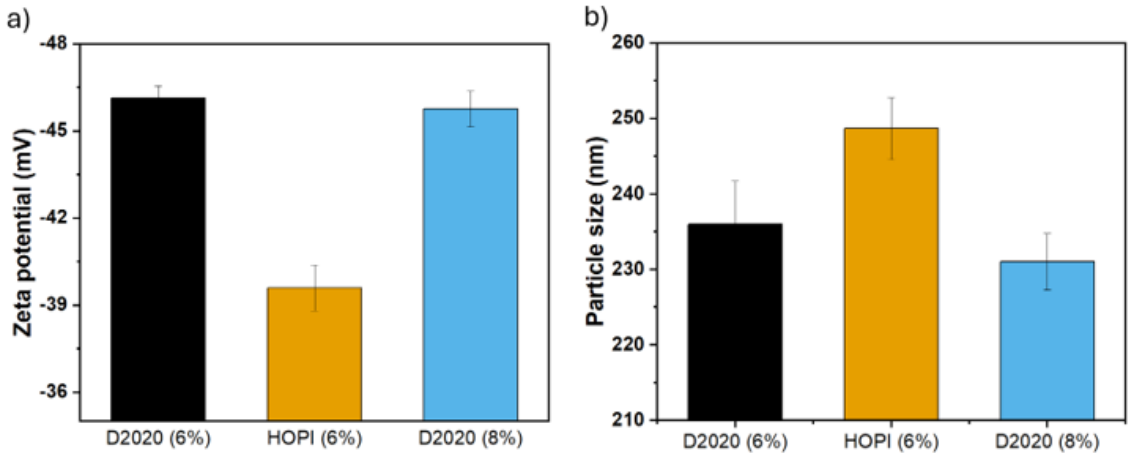

Figure 5.1: (a) Zeta-potential and (b) particle size measurement for Pt/C catalyst ink samples with different ionomers.

5.3.2 Catalyst ink viscosity

The steady-shear rheological measurements of catalyst ink samples are shown in Figure 5.2. All the Pt/C ink samples studied exhibited shear-thinning behavior (an increase in shear rate reduces the viscosity under shear stress) with plateau (or shear-thickening) at intermediate and high shear regions. For similar solid content (C/S = 6%), HOPI shows higher viscosity at low shear rate (<1 s^{-1}) which is likely to due to HOPI's ring-structured matrix. The steep drop in viscosity at low shear rate region is due to the breakdown of weakly connected particle agglomerates and their alignment with flow direction [114]. The increase in viscosity at intermediate shear rates is attributed to transient particle growth and the dominance of hydrodynamic shear forces [108]. The onset of this behavior is earlier for inks with Nafion than inks with HOPI. In addition, this shear thickening behavior is less pronounced with the increased in C/S from 6% to 8% for Nafion samples. HOPI and Nafion sample with 8% were also observed to contain two transient shear-thickening regions. From these observations, it can be considered that increased in carbon content from 6% to 8% and the ring-structured backbone of ionomer have significant effect in transient growth of agglomerates resulting in shear-thickening behavior. Finally, for shear rates greater than 0.1 s^{-1}, viscosity of ink sample with Nafion and C/S of 8% is always largest, indicating that the ink viscosity is mostly dominated by carbon concentration.

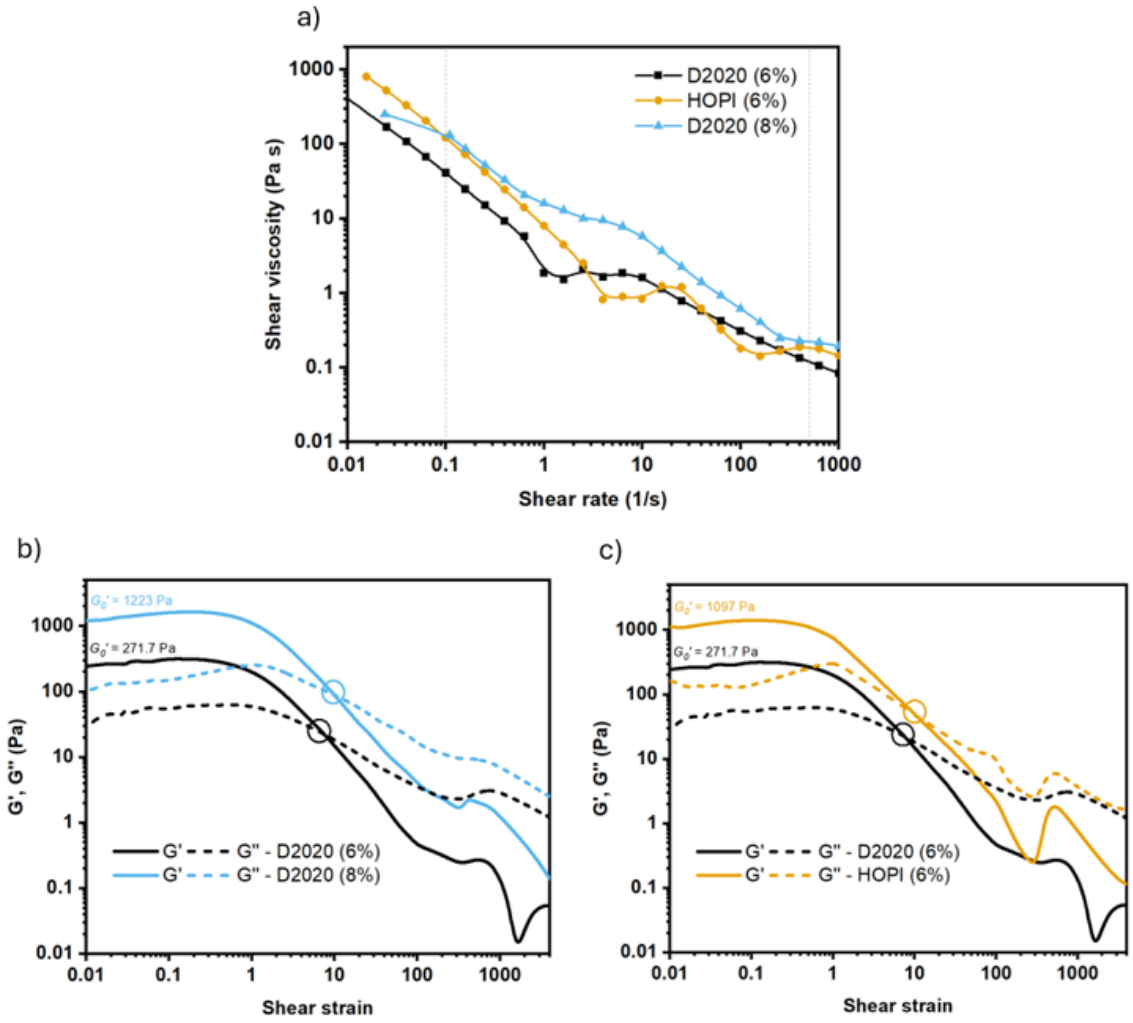

Figure 5.2: (a) Flow curve and amplitude sweep tests of Pt/C catalyst ink using different ionomers. (b) Amplitude sweep data for Pt/C inks with D2020 ionomer using different C/S; (c) Amplitude sweep data for Pt/C inks comparing HOPI and D2020. The encircled region denotes the transition point from solid-like to liquid-like.

The amplitude scan characterizes the viscoelasticity of the inks. At low strain, the region where G' and G" remain constant is defined as the linear viscoelastic region (LVER). The LVER is evident in the inks tested where G' and G" do not vary with strain at low strain. The measurement also showed that G' >G", indicating all tested ink samples have elastic behavior. A larger G' corresponds to stronger particle network strength, denoting higher resistance to separation [117]. At intermediate to high strain, G' and G" generally decrease with an increase in strain, indicating that the agglomerate network structure is broken down. At the high strain region,

transient increase in G' and G" is observed for all inks indicating some rearrangement of the agglomerate network. After the intersection of G' and G" and with increasing strain, G" of the inks are greater than G', and the inks show liquid viscous behavior. The volume fraction of particles in the ink affects the plateau storage modulus (G_0'). The high G_0' of Pt/C ink with Nafion and C/S of 8% is due to its high solid volume fraction. Interestingly, the G_0' (1097 Pa) of Pt/C ink with HOPI is somewhat similar to this value while the G_0' (271.7 Pa) of ink with Nafion with C/S of 6% is the smallest. It can also be observed that the transition from solid-like to liquid-like shifts to a marginally higher strain when C/S is increased to 8% or when HOPI ionomer is used instead of D2020.

5.3.3 Rheo-EIS measurement

A full frequency range EIS measurement was conducted on stationary samples to understand the Pt/C catalyst ink resistance before and after the application of high shear. By conducting a full frequency range EIS, the electrical resistance attributed to the carbon network can be differentiated from the sample's ionic resistance formed by the ionomer matrix. The Nyquist plot generated from the impedance data for all samples is shown in Figure 5.3. An equivalent circuit model (ECM) presented in Figure 4.5 was used to fit the EIS data and estimate the resistance of the elements. The ECM is composed of a resistor element (R_e) in parallel with a series connection of another resistor (R_i) and an imperfect capacitor (CPE). In particular, at low frequencies, the impedance of the capacitor becomes so large that current travels through the resistor element. In this case, the impedance of the sample is dominated by electrical resistance. In the same manner, high frequency measurements are used to probe the ionic resistance of the sample.

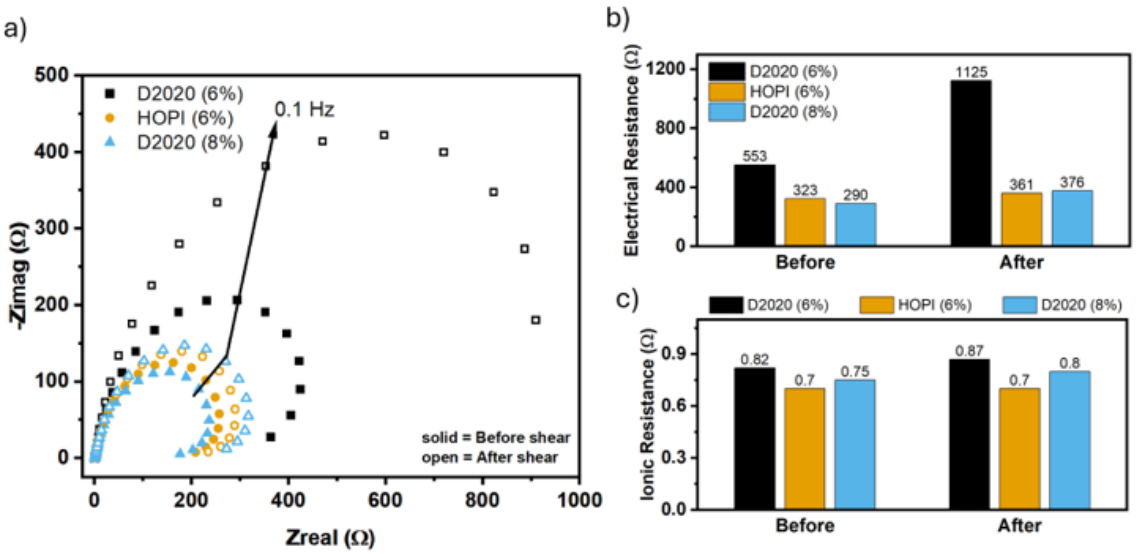

Figure 5.3: (a) Nyquist plot from the EIS measurement from 0.01 Hz to 100 kHz before and after high shear and the estimated (b) electrical and (c) ionic resistances of the Pt/C ink samples with different ionomer.

From the results, electrical resistance dominates the impedance of the catalyst inks with ionic resistance values all measuring below 1 Ω. In addition, all samples showed an increase in electrical resistance after application of high shear (500 s^{-1}). At C/S of 6%, the electrical resistance of samples with HOPI is less than that of ink with Nafion. This can be attributed to less catalyst surface coverage with HOPI ionomer because of its shorter side chains. The increase in electrical resistance after shear is also significantly less with HOPI ionomer than that of ink with Nafion (C/S of 6%). With the application of high shear, the polymer strands are expected to rearrange along the shear direction and provide greater surface coverage on the catalyst increasing the electrical resistance. The HOPI material contains a ring-structured backbone which minimizes polymer folding around the catalyst surface. As a result, there is less catalyst surface coverage increase after shear compared to Nafion (6%). The measured increase in electrical resistance with Nafion (6%) is 103% while that in HOPI is only 12%. Increasing the carbon concentration provides more carbon-to-carbon interaction and electrical pathways to the sample. This is evident in the smaller electrical resistance of samples with Nafion (8%) than that of Nafion (6%). The increase in electrical resistance after shearing of the sample with Nafion (8%) is 30%, significantly less than Nafion (6%) but greater than HOPI samples.

In order to study the impedance behavior and thixotropy of ink during the coating process, a 3PRT was conducted. Impedance characteristics of ink provide

an insight into the evolution of microstructure, particularly Pt/C and ionomer interactions. On the other hand, thixotropy informs how the ink viscosity vary with time as a result of shear [58]. Selection of ink with suitable thixotropic properties is essential since it enables uniform thickness in the catalyst layer (CL). In the 3PRT, it is assumed that formation of CL from catalyst ink consists of three steps: (1) ink is at static state under low shear, (2) ink undergoes high shear during coating process, and (3) ink is at recovery stage and returns to low shear after coating. Results from the tests are shown in Figure 5.4. Viscosity trend measured during the first and second phase were consistent with the flow curves in Figure 5.2 denoted by a vertical dotted line at 0.1 s^{-1} and 500 s^{-1}, respectively. HOPI and Nafion (8%) have similar viscosities and are larger than that of Nafion (6%). The impedance measured at 0.1 Hz during first phase is also consistent with the steady state test before applying shear confirming that HOPI's short side chain minimizes extent of catalyst surface coverage and increasing carbon content for ink with Nafion provides more electrical pathways due to more carbon-to-carbon interaction. During high shear, the ink internal structure is destroyed and the sample viscosity decreases. At this stage, shear force is greater than the attractive forces between agglomerates in the inks (i.e., van der Waals, polar bonds, and hydrogen bonds) which caused the drastic drop in viscosity [117]. This is also evident in the increase in the measured impedance for all samples during the second phase. In addition, inks with Nafion ionomer were observed to have higher increase in impedance than ink with HOPI ionomer implying that folding of polymer backbone on catalyst surface is a major factor in the increase of resistance and that HOPI's ring structure minimized the dense folding of ionomer. During the third phase, all Pt/C ink samples not only fully recover the original microstructure but even formed a more compact agglomerate structure which is more evident in samples with Nafion ionomer as denoted by the increase in viscosity. This implies that original interaction formed in the carbon/HOPI agglomerate is more difficult to breakdown than carbon/Nafion agglomerates. From the impedance measured at the third phase, it can be observed that resistance values were gradually increasing from the initial cessation of high shear. Comparing the measured values at the end of the test, it can be seen that there is significant increase in resistance for Nafion (6%) from first phase to third phase measurements. This is consistent with the result from steady state impedance test. Meanwhile, the least increase in resistance is observed for HOPI samples consistent with earlier observations during steady state measurements.

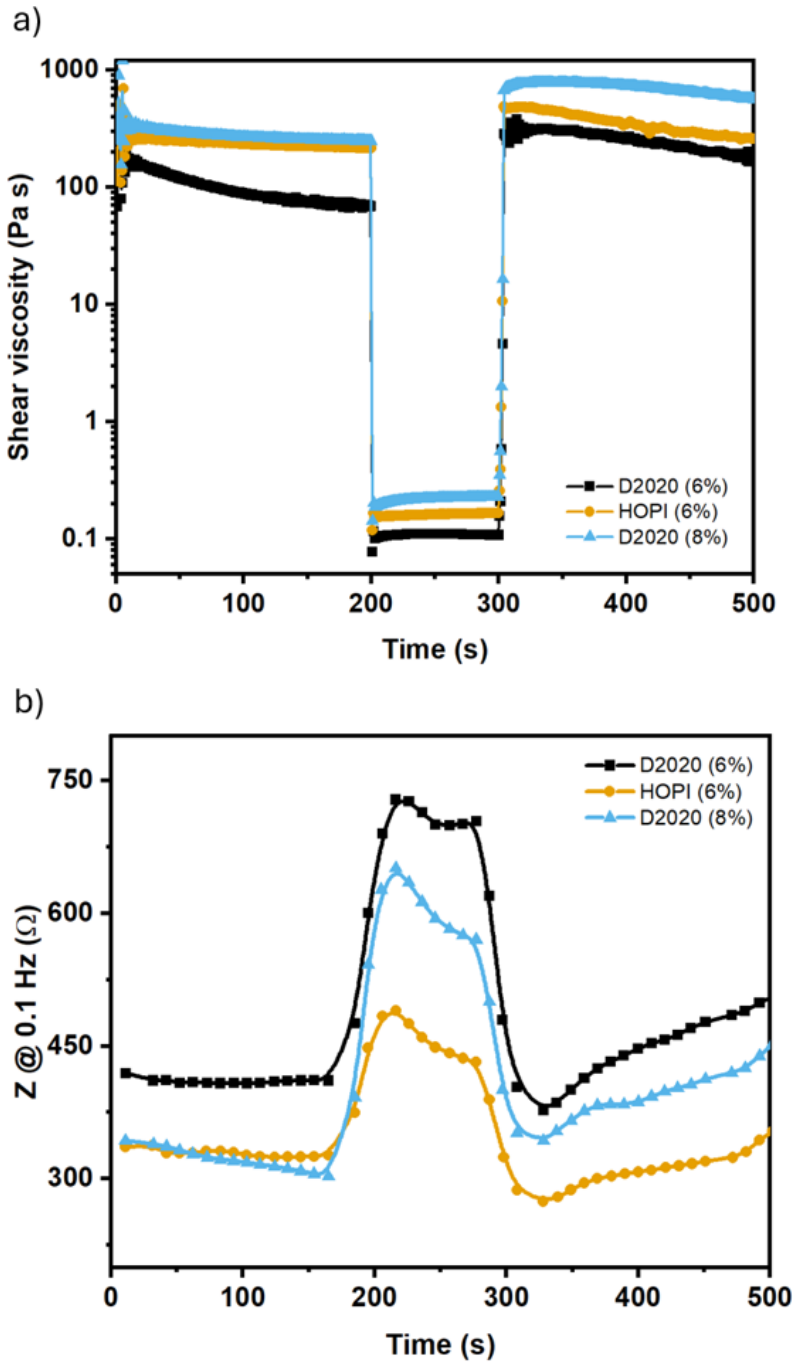

Figure 5.4: 3PRT measurements showing the (a) thixotropy and (b) impedance behavior of Pt/C inks with different ionomers.

In the coating process, it is important to match the thixotropy of the ink. The slow structure recovery is advantageous to the self-levelling of wet film, resulting

in a more even CL. If the structure recovery is too quick, it is not conducive to good leveling. However, if the ink structure recovery is too slow, there may not be enough wet film thickness [58, 117]. Therefore, it is essential to regulate ink thixotropy by adjusting the carbon content or type of ionomer to improve the structure of the CL.

5.3.4 CL microstructure and MEA performance

CL morphology

We performed SEM analysis of the fabricated cathode CLs using HOPI to examine the morphology and the size of the formed Pt/C agglomerates. The SEM images for the HOPI-based CL are shown in Figure 5.5. The macroscopic surface of the prepared CL showed significant mud-cracking for the HOPI. Examining the microscopic structure, we can see that HOPI CL has a uniform carbon agglomerate size and pore structure. These observations are similarly observed from a previous study [123]. Additionally, we observed patches on the microstructure with ionomer bridging features.

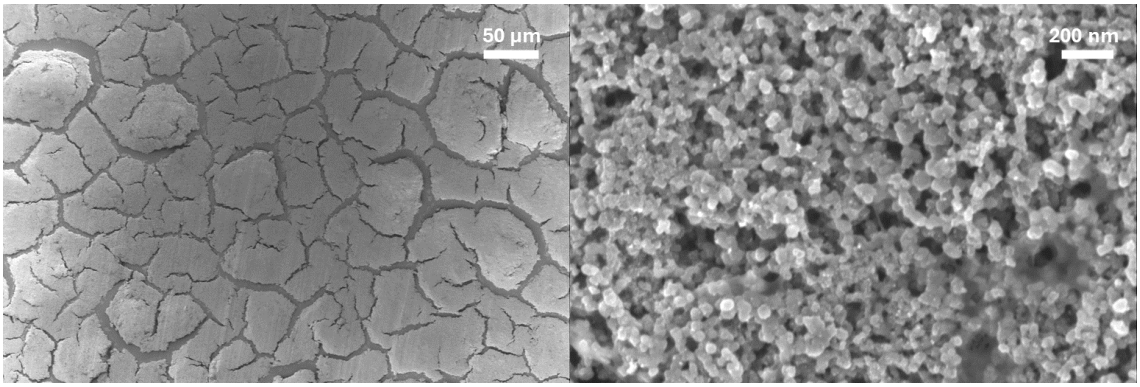

Figure 5.5: SEM images of the CL surface using HOPI at 200x and 50,000x magnifications.

Oxygen transport resistance

Oxygen transport resistance (OTR) in the cell was measured by conducting *in situ* limiting current experiments. The procedure differentiates the pressure-dependent and pressure-independent OTR components in the cell. The detailed theory underlining the procedure can be found in Ref. [80] and Ref. [10]. Limiting current measurements under dry conditions provide the total OTR of the catalyst layer and gas diffusion media in the absence of liquid water. From the dry limiting

current data provided in Figure 5.6(a), it can be seen that HOPI and D2020 cells have similar diffusion transport resistance, with HOPI being only marginally higher. OTR under wet conditions was also evaluated and presented in Figure 5.6(b). Both curves show the transition from dry to wet conditions in the gas diffusion layer. The HOPI cell has higher OTR denoting that it can retain more water than the D2020 cell.

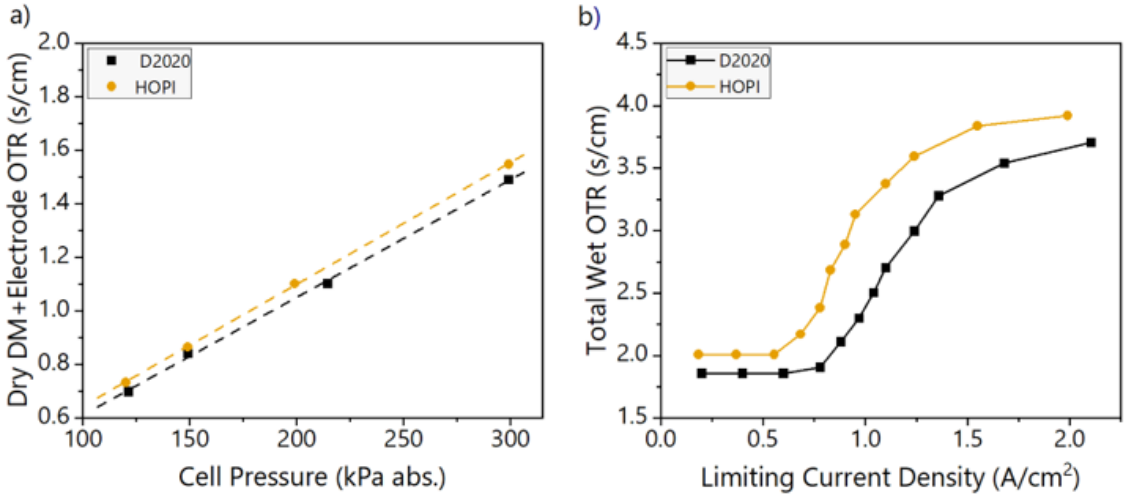

Figure 5.6: Oxygen mass transport resistance for D2020 and HOPI cells under (a) dry and (b) wet limiting current conditions.

Membrane and CL proton transport resistance

The proton transport resistance, also referred to as sheet resistance, in the cell was evaluated at three different RH conditions (100%, 70%, and 40% RH) using EIS measurements under H_2/N_2 flow. The result of the test is presented in Figure 5.7(a) and Figure 5.7(b) for high-frequency resistance (HFR) and sheet resistance, respectively.

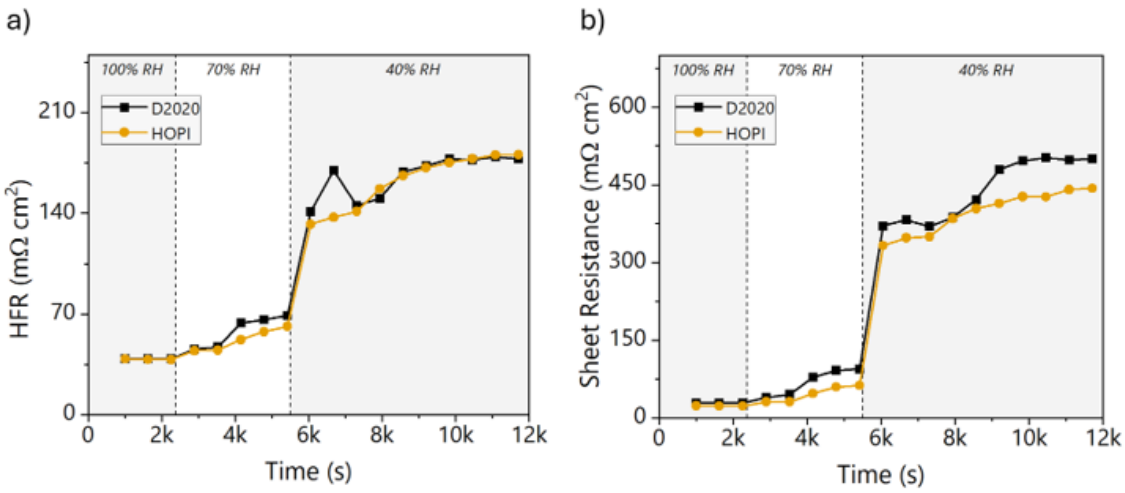

Figure 5.7: (a) HFR measurement and (b) cathode CL proton transport resistance measurement for HOPI and D2020 cells.

HFR measurements primarily denote the extent of membrane hydration. Despite using a similar membrane, the cell with HOPI has slightly lower HFR values than the cell with D2020. This observation suggests that HOPI has enhanced water retention capacity at the catalyst layer that could facilitate more efficient proton transport from the membrane to the cathode CL. From Figure 5.7(b), cathode proton transport resistance across various RH levels for the HOPI cell is lower than that of D2020 cell. This signifies that HOPI has superior proton conductivity than D2020 within the CL that is mainly due to the low EW of the HOPI compared with D2020 (925 vs 1000). With lower EWs, more sulfonate groups are available per unit volume, and in sum, to conduct protons, enhancing the overall conductivity. This improvement is particularly advantageous under dry operation where CL proton transport resistance is exacerbated.

MEA performance

The ECSA of both cells was measured using HAD method [80] and was found to be around 50 m^2 g^{-1}, denoting that the cells were in relatively good condition. After activating the catalyst, fuel cell performance was assessed by comparing the i-V polarization curve under dry and wet operating conditions. The H_2/air polarization curves along with HFR measurements for both the HOPI and D2020 cells are shown in Figure 5.8(a) and Figure 5.8(b) for dry and wet operating conditions, respectively.

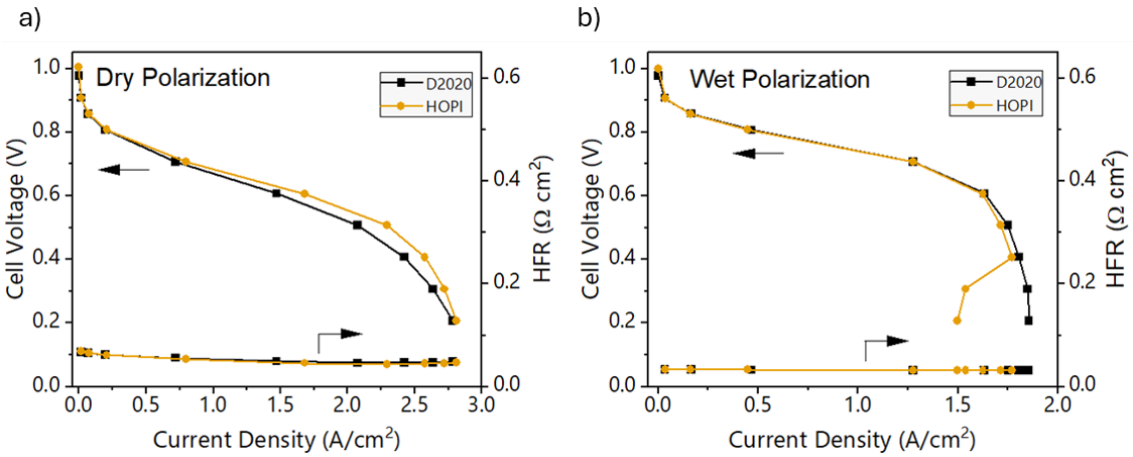

Figure 5.8: Performance and HFR curves for HOPI and D2020 cells under (a) dry and (b) wet conditions.

Under low relative humidity conditions, the HOPI cell shows a slightly superior performance. Additionally, the HFR is slightly lower for the HOPI cell than the D2020 cell. Under wet conditions, the HOPI cell shows comparable performance levels to the D2020 cell until reaching the mass transport region, at which point pronounced flooding occurs at elevated current density conditions. This might have been caused by the higher water retention capacity of HOPI, as inferred from sheet resistance measurement in Figure 5.7(b). It should be noted that flooding at high current densities can also be attributed to the high oxygen transport resistance for the gas diffusion media used in the HOPI cell observed in Figure 5.6.

5.4 Summary

In this work, we performed comparison of catalyst ink properties and microstructure using different ionomer, i.e. Nafion 1000 EW D2020 and 925 EW HOPI. In our investigation, we determined that HOPI-based ink structure is similar to D2020-based ink structure with higher C/S content (8%). Our study also suggests that for D2020, increasing C/S ratios leads to stronger viscoelastic properties. In addition, HOPI-based ink, despite having the largest measured particle size, shows higher viscosity than D2020-based ink with similar C/S. This denotes that there is increased particle-particle interactions in HOPI ink due to the different ionomer property.

The performance of HOPI-based CL was compared with that of benchmarked D2020-based CL by conducting MEA *in situ* measurements. It was observed that while both CL have relatively similar performance, HOPI-based CL experienced

flooding under wet conditions at high current densities. At this operating condition, mass transport limitation becomes dominant, and the CL microstructure of HOPI-based CL having significant mud-cracking on the surface as observed in the morphology proved to be susceptible to flooding.

Chapter 6

STUDY OF CATALYST INK MULTICOMPONENT INTERACTION USING RHEO-IMPEDANCE MEASUREMENTS

The complex interactions between catalyst ink components influence the macroscopic properties and microstructure of the ink. These, in turn, dictate the fabricated CL microstructure and resulting MEA performance. Most of the studies on catalyst ink have been focused on the relationship between CL structure and performance [28, 60, 66, 67, 72, 118, 121, 126]. As a result, catalyst ink and CL fabrication have been mostly empirical in nature. Understanding how CL microstructure is formed is necessary to advance CL design.

Different catalyst ink parameters (i.e., ionomer type and loading, solvent formulation, carbon loading, etc.) influence various ink component interactions. These interactions, as a result, modulate CL microstructure and MEA performance. For example, ionomer/solvent interactions affect the conformation of ionomer in the solution, ionomer/carbon interactions influence how the ionomer adsorbed onto the Pt/C catalyst particles in the ink, and the interactions among the three components determine the overall agglomerate sizes and pore structures in the fabricated CL [45].

In this study, we provide a systematic method and design of experiment to provide insight and bridge the gap between the relation of catalyst ink parameters and cell performance. We utilize different techniques to characterize catalyst ink properties and elucidate the evolution of microstructure on catalyst ink that simulates the CL fabrication process.

6.1 Experimental Methods

6.1.1 Catalyst Ink Preparation and Design of Experiment

The tested catalyst ink samples have varying I/C ratio and 2-propanol (IPA) to water (W) ratio. Meanwhile, the carbon-to-solvent ratio is fixed at 0.08. The catalyst ink is prepared using 46.8% Pt/C (TKK, TEC10E50E) and 20 wt% ionomer dispersion (D2020, Ion Power). The samples tested are labeled according to the level

of IPA/W and I/C ratios (e.g., 'HL' corresponds to high IPA/W and low I/C, 'MM' corresponds to medium levels for both parameters, and so on). The complete design of the experiment is presented in Table 6.1.

Table 6.1: Sample formulation and design of experiment

Sample name	IPA/W	I/C
LL	0.5	0.25
LH	0.5	1.25
MM	1.0	0.75
HL	2.0	0.25
HH	2.0	1.25

The samples are prepared by mixing the ionomer dispersion and solvent in a vial, sonicating the vial, and adding them to a plastic container containing the catalyst powder with eight (8) Zirconia beads (5 mm diameter) for mixing. Mixing of catalyst ink is conducted using a high-energy centrifugal mixer (AR-100 Thinky mixer) at 2000 rpm for 3 minutes followed by defoaming for 10 seconds. The samples are immediately subjected to a series of rheo-EIS measurements after preparation to ensure minimal disparity brought by colloidal instability with prolonged storage time. In parallel, inks were coated onto a PTFE decal to further process into MEA.

6.1.2 MEA preparation and fuel cell test

Pt/C catalyst ink samples were used as cathodes in a membrane electrode assembly (MEA). The inks were coated onto a virgin PTFE substrate with the desired loading and thickness using a Mayer rod coater. For anodes, a standard catalyst ink recipe was used with D2020 as ionomer and Pt loading of 0.13 mg_{Pt} cm^{-2}. The coated CLs were dried under ambient conditions before the decal transfer. Using the hot-press method, the CLs were transferred onto NRE211 membrane under 130 °C and 300 psi for 5 mins.

For the fuel cell assembly, Freudenberg H23I5C8 was used as gas diffusion layer (GDL) with PTFE gasket for sealing and compression stop, yielding a GDL strain of approximately 17%. The performance of the fabricated MEAs were evaluated using a cell with straight parallel flow channels and an active area of 2 cm^2 in an automated Greenlight G20 fuel cell test station. To evaluate the ohmic resistance of the cell, high frequency resistance (HFR) was measured via EIS using Gamry Reference 3000 coupled with a Gamry 30k booster.

To measure the electrochemically active surface area (ECSA), cyclic voltammetry (CV) was performed under H_2/N_2 environment using 50 mV/s scan rate. Break-in protocol was conducted to activate the CLs by cycling the voltage between open circuit voltage (OCV), 0.40, 0.60, 0.70, and 0.85 V for 16 cycles. After break-in, a series of tests listed in Table 6.2 were conducted to evaluate performance under dry and wet conditions. Limiting current tests were used to evaluate oxygen transport resistance under dry conditions. Proton transport resistance in the membrane and cathode CL was evaluated via EIS under H_2/N_2 environment at different RH.

Table 6.2: Fuel cell test protocol for MEA with different ionomer types (D2020 and HOPI)

Test	Temp. (°C)	RH (%)	Press. (kPaa)	Voltage (V)
CV	30	100	100	0.05 - 1.2
Break-in	70	100	150	OCV - 0.40
Dry i-V	70	60	100	OCV - 0.20
Wet i-V	70	100	300	OCV - 0.20
Dry lim. i	80	64	100 - 300	0.30 - 0.09
Sheet resistance	70	40 - 100	300	0.20 (10mV AC)

6.1.3 DLS and zeta potential measurements

Dynamic light scattering (DLS) and zeta potential measurements were performed using a Malvern Zetasizer Nano ZS (Malvern Panalytical Ltd). The catalyst inks were diluted to 0.01 wt% using solvent (alcohol:DI = 0.923) and sonicated prior to analysis to avoid multiple scattering and improve the quality of DLS measurements. A small portion of the diluted catalyst ink was transferred into a dip cell (ZEN1002) for analysis. All tests were done at 25°C. At least three readings were taken to ensure the repeatability of the measurements.

6.1.4 Rheology and rheo-EIS measurement

Rheology and rheo-EIS measurements were performed using a rotational rheometer equipped with temperature controller (Kinexus Prime ultra+, NETZSCH) with some modifications as described in Chapter 4. Notably, for conducting simultaneous rheology and impedance measurements, the roughened top and bottom plate geometries were electrically insulated from the rest of the rheometer body. The electrical connection between top and bottom plate was established through a stainless-steel needle dipped in liquid metal (Gallium Indium Eutectic, EGaIn, Sigma Aldrich) contained in the solvent trap at the top plate and wires connected

to the bottom plate. A potentiostat (CH Instrument 750E) was used to measure impedance. All samples were tested at 25°C. The detailed measurement protocol is discussed in Chapter 4.

6.1.5 Surface Roughness Measurement

Surface roughness of catalyst ink-coated PTFE decal was performed using Bruker Dektak XT Stylus profilometer equipped with a 2 μm probe traced over a total distance of 5 mm. Measurement was performed at various locations throughout the samples. The average (Ra) and root mean square (Rq) roughness measurements illustrate the overall height variability. In addition, Rq is analogous to the standard deviation of the surface height distribution about the mean height datum.

3D surface images of the cathode CL on the prepared MEA were obtained using a white light interferometer. Surface roughness was measured from 2D profiles taken at different positions throughout the samples using the image processing software Gwyddion. Similar to the catalyst ink-coated PTFE decal, Ra and Rq measurements of CL from MEA samples were reported.

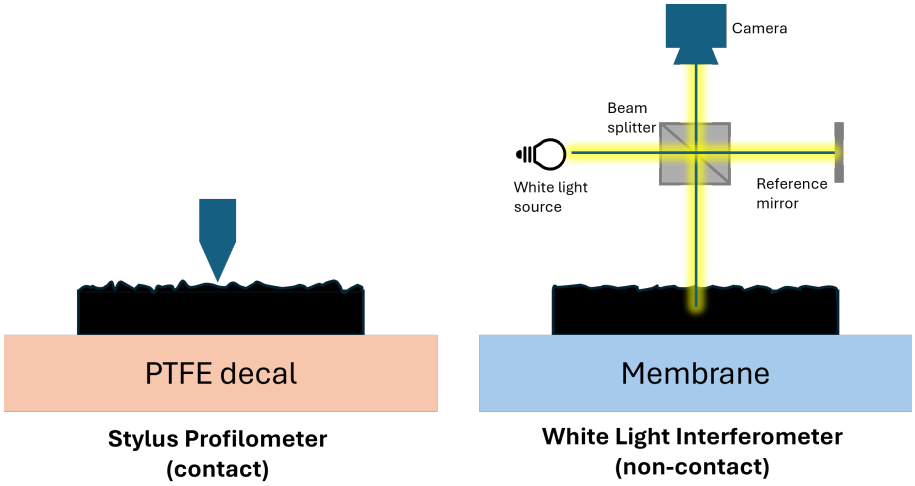

Figure 6.1: Schematic of surface roughness measurements using stylus profilometer and white light interferometer for ink-coated PTFE decal and catalyst coated membrane, respectively.

6.1.6 Scanning electron microscopy

The morphology of the catalyst layer on the ink-coated PTFE decal and on the catalyst-coated membrane (CCM) was characterized using a scanning electron microscope (Zeiss Gemini). The imaging was performed on the side of the PTFE

decal, i.e., after hot pressing the decal against Nafion membrane such that the images represent the surface facing the membrane in the cell assembly.

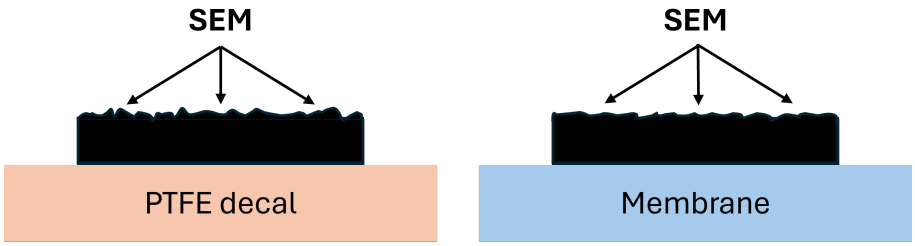

Figure 6.2: Schematic of SEM measurements for ink-coated PTFE decal and catalyst coated membrane.

6.2 Results and Discussion

6.2.1 Catalyst Ink Property and Microstructure

The ζ-potentials of different catalyst ink samples are measured to understand the relative electrostatic stability of Pt/C particles for all samples. Results of the ζ-potential and agglomerate size measured by DLS (Figure 6.3) showed that all samples have large (negative) ζ-potentials indicating strong electrostatic repulsion. From Figure 6.3(a), it can be seen that solvent with high ε (i.e., water-rich) promotes -SO_3H dissociation and increases charge density on the surface of the ionomer particles, thereby leading to more negative ζ-potential [119]. The effect is also more significant for sample with high ionomer loading. This is clearly evident by the large negative ζ-potential of the LH sample with water-rich solvent.

From Figure 6.3(b), particle size generally increases with increasing IPA/W ratio for a given I/C, except at the highest I/C where it decreases slightly at the highest IPA/W. The measured polydispersity index (PDI) signifies more heterogeneous particle distribution at high ionomer loading (Figure 6.3(c)). Lowest PDI is observed at the lowest I/C and IPA/W, indicating a more uniform particle size distribution. High IPA/W generally results in higher PDI, except at the highest I/C where the PDI slightly decreases.

In general, high ionomer loading increases particle size and PDI, suggesting more aggregation and heterogeneity. Additionally, it significantly increases particle stability (more negative zeta potential). On the other hand. high IPA/W ratios tend to increase particle size and PDI, indicating more aggregation and size distribution heterogeneity. However, it reduces particle stability (less negative zeta potential). These findings suggest that high ionomer loading and a balanced IPA/W ratio would be optimal to ensure stable suspension with uniform particles.

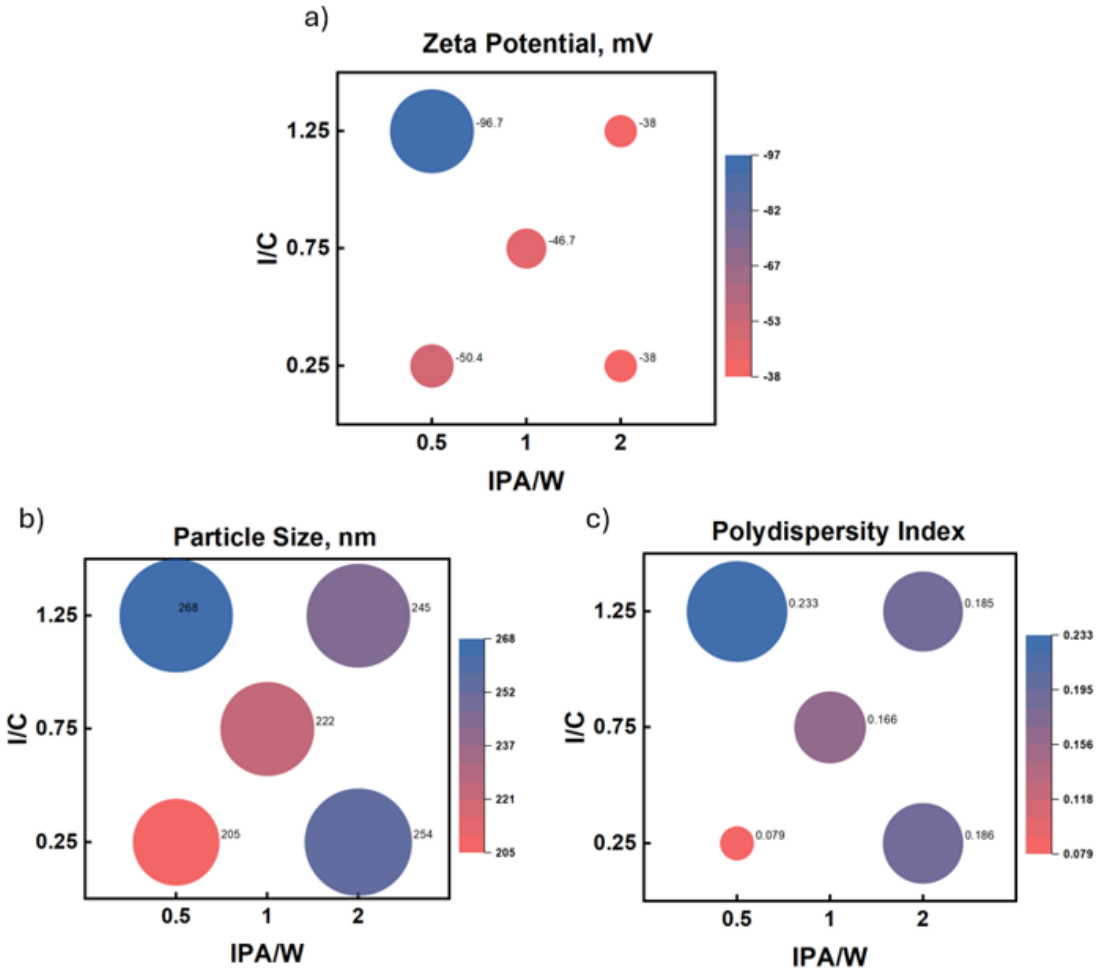

Figure 6.3: (a) Zeta-potential, (b) particle size, and (c) polydispersity index measurements for all samples.

A full frequency range EIS measurement was conducted on stationary samples to understand the Pt/C catalyst ink resistance before and after the application of high shear. The estimated electrical and ionic resistances based on the ECM (Figure 4.5) fitting are presented in Figure 6.4. From the measurement, we see that the Pt/C catalyst ink is predominantly ionic conductive and that ionic resistance measurements are relatively the same for all samples. From Figure 6.4(a) and (b), we can observe that the effect of I/C in increasing electrical resistance is more significant than decreasing IPA/W (an order of magnitude difference). The high ionomer loading provides more carbon surface coverage that contributes to the electrical resistance. In addition, increasing water content enhances polarity and allows the ionomer side chains to swell and open up resulting in more area coverage and

greater electrical resistance. Shearing the ink breaks down and realigns the carbon network structure and at low ionomer, carbon percolation is stronger.

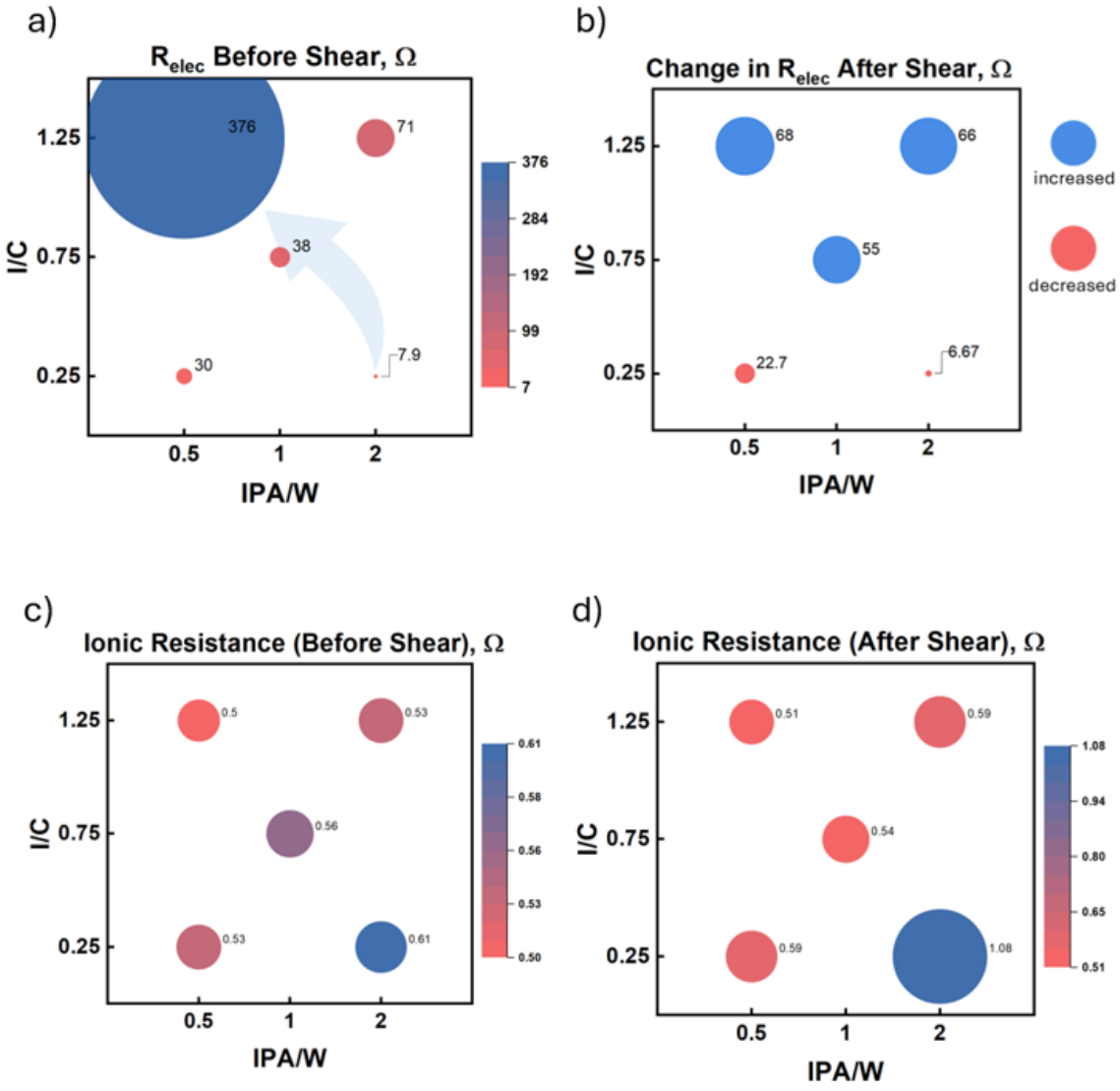

Figure 6.4: (Electrical resistance (a) before and (b) change in electrical resistance after application of high shear. Ionic resistance (c) before and (d) after application of high shear.

In order to study the impedance behavior and thixotropy of ink during the coating process, a 3PRT was conducted. Impedance characteristics of ink provide an insight into the evolution of microstructure, particularly Pt/C and ionomer interactions. On the other hand, thixotropy informs how the ink viscosity vary with time as a result of shear [58]. Selection of ink with suitable thixotropic properties is

essential since it enables uniform thickness in the catalyst layer (CL). In the 3PRT, it is assumed that formation of CL from catalyst ink consists of three steps: (1) ink is at static state under low shear, (2) ink undergoes high shear during coating process, and (3) ink is at recovery stage and returns to low shear after coating. Results from the tests are shown in Figure 6.5. LL and HL show higher initial viscosities (phase 1) compared to LH, HH, and MM. This suggests that LL and HL are more resistant to initial flow. During high shear (phase 2), the ink internal structure is destroyed and the viscosity decreases for all samples. At this stage, shear force is greater than the attractive forces between agglomerates in the inks (i.e., van der Waals, polar bonds, and hydrogen bonds) which caused the drastic drop in viscosity [117]. Interestingly, for LL and LH samples, thixotropic and rheopectic behaviors are observed, respectively. In the third phase, it can be seen that all samples have recovered their microstructure. The impedance measurement at 0.1 Hz follows the same trend as observed during the steady-state before and after shear tests. High electrical resistance is measured with increasing ionomer loading and with water-rich solvent. At high shear, the ink internal structure is destroyed which explains the increase in impedance.

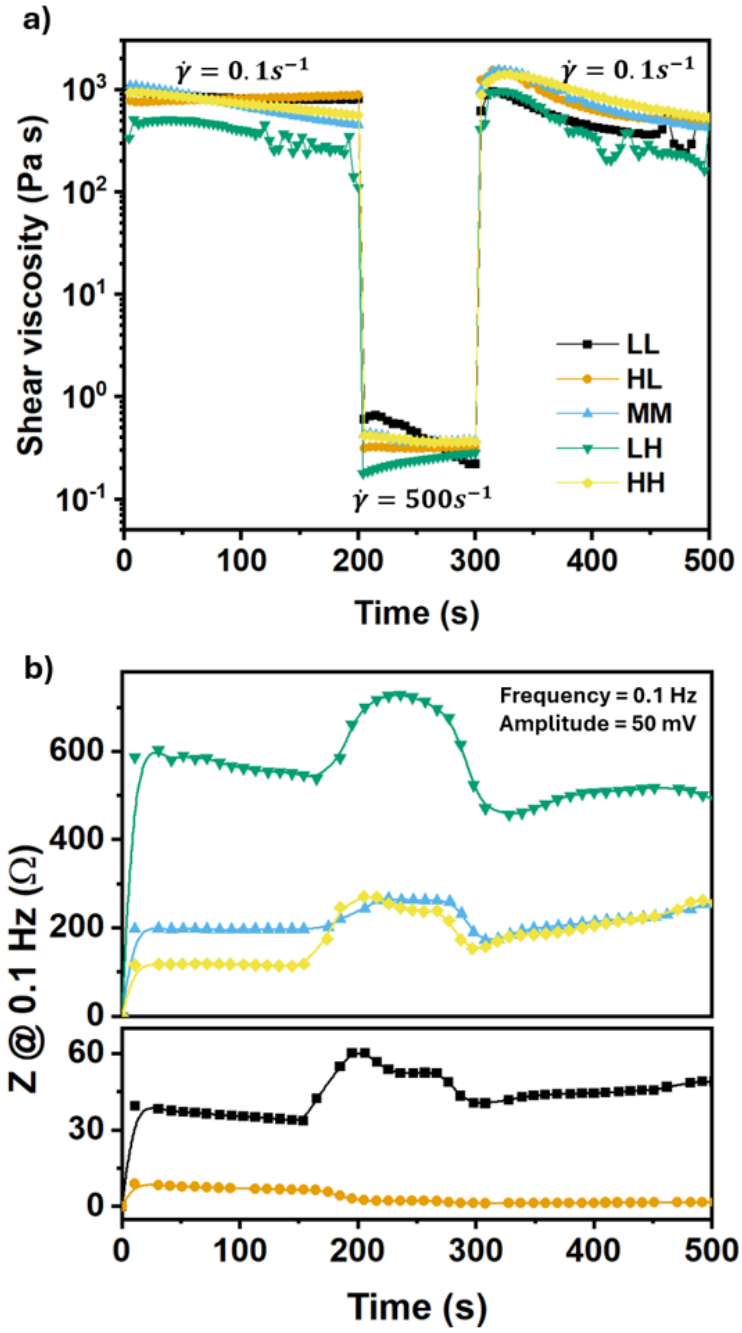

Figure 6.5: Three-phase rebuilt measurement showing the (a) thixotropy and (b) impedance behavior of Pt/C inks samples.

The steady-shear rheological measurements of catalyst ink samples are shown in Figure 6.6. All the Pt/C ink samples studied exhibited shear-thinning behavior (an increase in shear rate reduces the viscosity under shear stress) with plateau (or

shear-thickening) at intermediate and high shear regions. Similar to the 3PRT, LL and HL show higher viscosities at low shear rates compared to LH, HH, and MM. This suggests that LL and HL are more resistant to initial flow. LH sample appears to have the lowest viscosity at low and high shear rates.

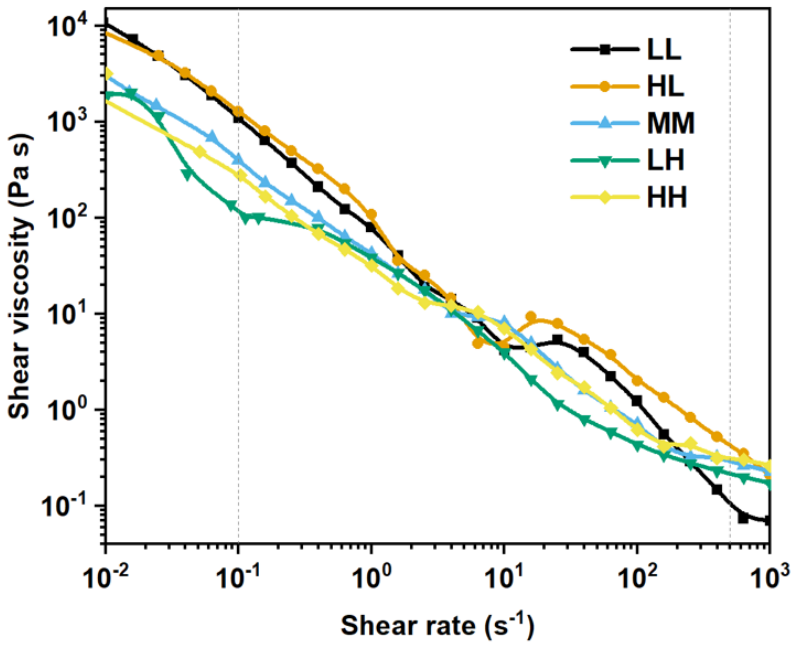

Figure 6.6: Flow curve of different Pt/C catalyst ink samples.

The amplitude scan characterizes the viscoelasticity of the inks. At low strain, the region where G' and G" remain constant is defined as the linear viscoelastic region (LVER). The LVER is evident in the inks tested where G' and G" do not vary with strain at low strain. At low strain, the measurement also showed that G' >G", indicating all tested ink samples have elastic behavior. A larger G' corresponds to stronger particle network strength, denoting higher resistance to separation [117]. LL and HL start with high G' values indicating strong elastic behavior at low shear strain. HH and MM have lower initial G' values, indicating weaker elastic behavior while LH has the lowest initial G' denoting weakest elastic behavior. At intermediate to high strain, G' and G" generally decrease with an increase in strain, indicating that the agglomerate network structure is broken down. At the high strain region, transient increase in G' and G" is observed for all inks indicating some rearrangement of the agglomerate network. After the intersection of G' and G" and with increasing strain, G" of the inks are greater than G', and the inks show liquid viscous behavior.

Low ionomer samples (LL and HL) have higher G' and G" values compared to the rest of the samples. This denotes that LL and HL are more resistant to structural breakdown under shear. Additionally, the phase angle (Eq. 6.1) for LL and HL samples has a more gradual increase compared to the others, suggesting that they have more stable transition from solid-like to liquid-like state.

$$\delta = \tan^{-1}\left(\frac{G''}{G'}\right) \tag{6.1}$$

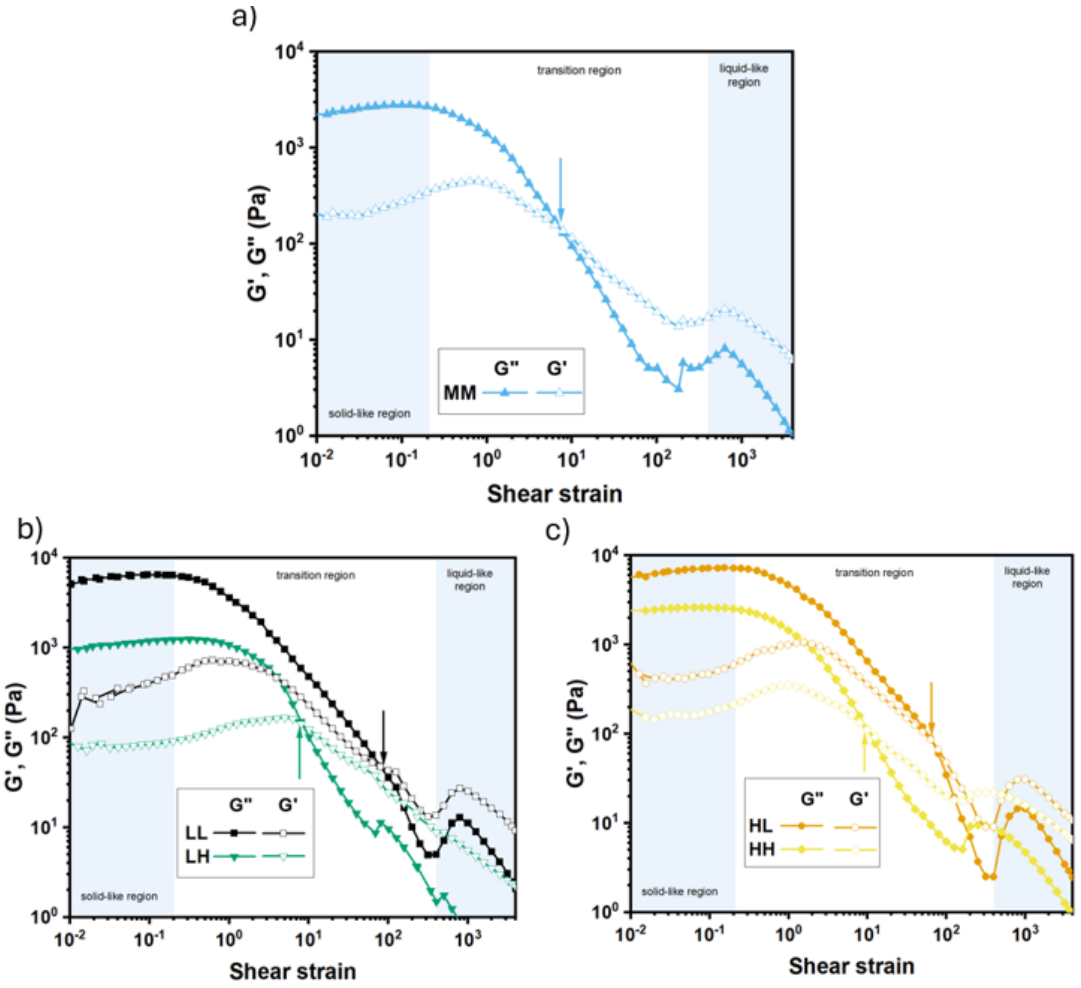

Figure 6.7: Amplitude sweep measurement for Pt/C catalyst ink samples: (a) MM, (b) water-rich (LL and LH), and (c) IPA-rich (HL and HH) samples. The arrows indicate the transition from solid-like to liquid-like. Solid symbol, G': storage modulus; open symbol, G": loss modulus.

It can also be observed from Figure 6.7(b) and 6.7(c) that the transition from solid-like to liquid-like state shifts to higher strain as ionomer loading (I/C) is decreased for inks with the same solvent formulation. The transition point also does not seem to differ between samples having the same ionomer loading regardless of solvent formulation. The plateau of storage modulus (G_0') is also observed to increase with IPA-rich solvent (and low I/C) inks which is indicative of an agglomerated structure.

6.2.2 Catalyst Layer Structure

Catalyst layer properties and microstructure are affected by ink properties, CL fabrication, and MEA preparation. After catalyst ink formulation, significant structural changes occur, more so, during ink processing on decal substrate followed by hot press transfer that is commonly used for membrane electrode assembly preparation. The schematic of the process is shown in Figure 6.8. The hot press transfer conditions with the elevated temperature (130 °C) and pressure (300 psi) have been observed to improve the surface properties, homogeneity, and structural durability of MEAs. The increase in temperature and pressure enhances the adhesion and contact between electrode and membrane. This is critical when aiming for a more durable and stable MEA as delamination is minimized. The process also minimizes the defects or cracks in the catalyst layer which results in better performance and more durable material.

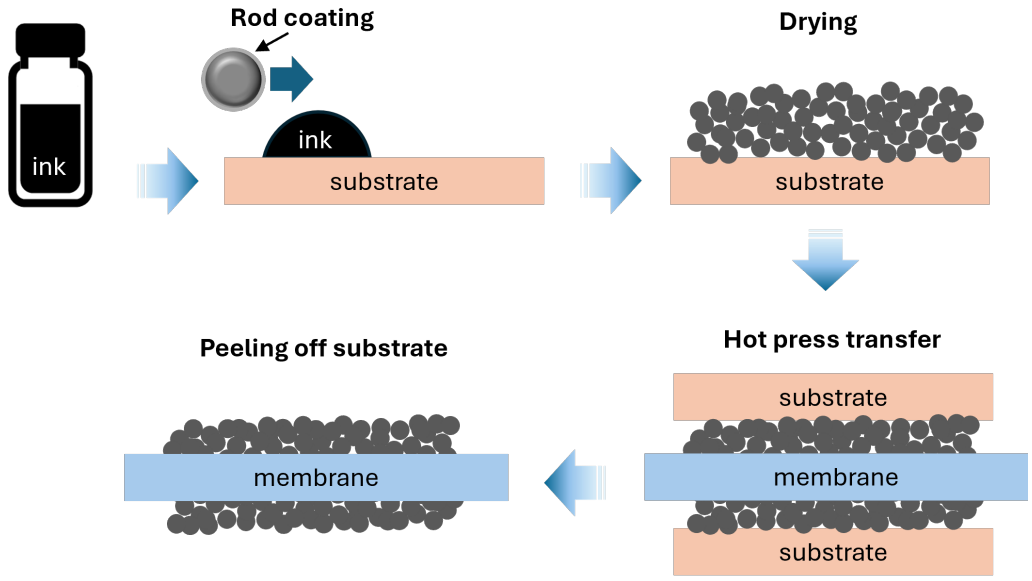

Figure 6.8: Schematic of MEA fabrication using hot press transfer method from ink-coated decal substrate.

The morphology of the catalyst layer formed was examined using SEM. The SEM images of ink-coated PTFE decals are shown in Figure 6.9. From the figure, the LL sample shows significant cracking and a rough surface structure. There also appear aggregated particle clusters. HL sample appears to have fewer cracks and a more uniform texture than LL sample. Similar to LL, the LH sample shows a less uniform surface than HH. Among the samples, MM appears to have a moderate improvement in surface structure. In general, increasing ionomer improves adhesion between ink particles and reduces CL cracking which leads to a more uniform surface. A higher IPA/W ratio also appears to contribute to a finer particle distribution and smoother surface morphology, reducing the aggregation and large-scale cracking seen at lower ratios. This is also supported by the surface roughness measurements shown in Figure 6.10.

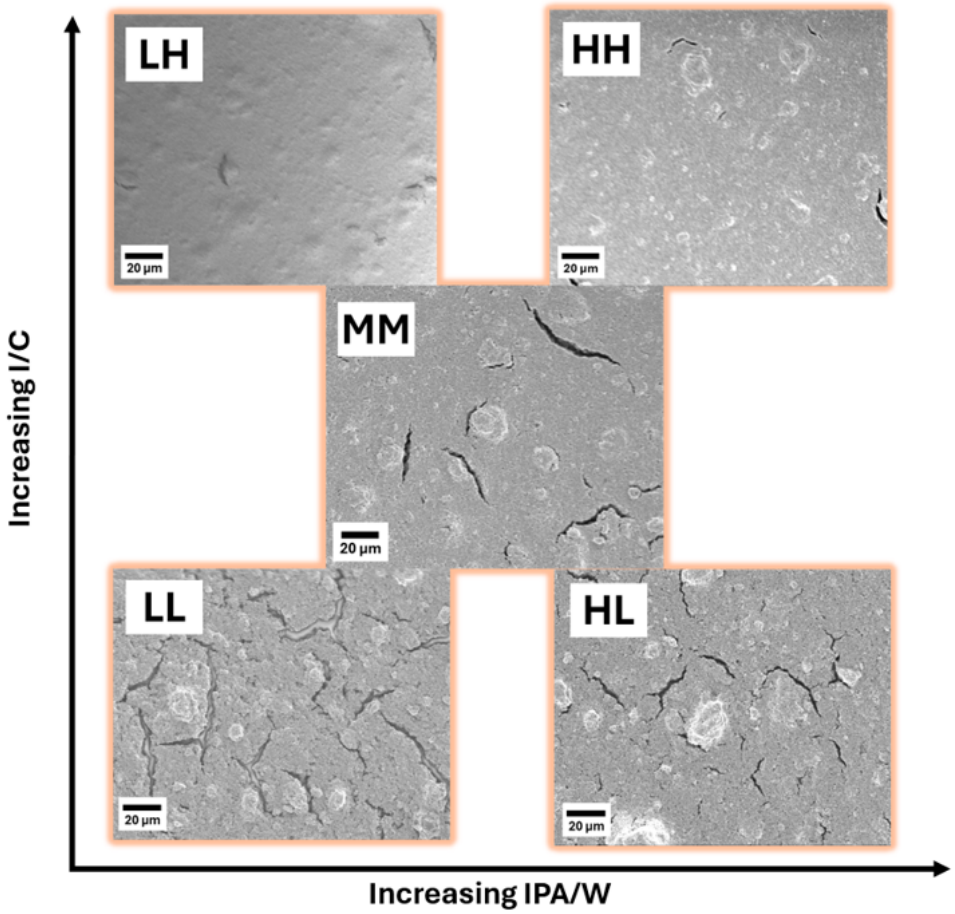

Figure 6.9: SEM surface images of the catalyst ink-coated PTFE decal. The scale bar represents 20 μm.

The surface roughness was measured using a stylus profilometer. In a stylus profilometer, a stylus connected to a cantilever arm moves across the surface in a controlled manner on a preset path. As it moves, the vertical movements of the stylus are converted to create a detailed surface profile. The measured surface profile for each sample is presented in Figure B.2. In our measurements, we get the average surface roughness (Ra) to illustrate the overall height variability and the root mean square roughness (Rq) which is analogous to the standard deviation of the surface height distribution about the mean height datum. These data (Ra and Rq) are shown in Figure 6.10(a) and Figure 6.10(b), respectively.

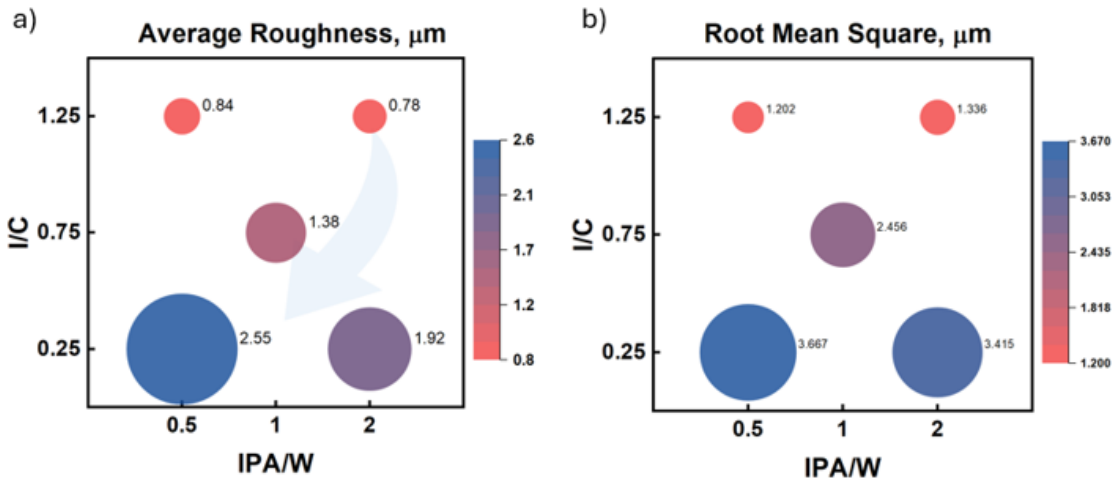

Figure 6.10: (a) Mean surface roughness (Ra) and (b) root mean square roughness (Rq) measurements of the ink-coated PTFE decal surface.

From Figure 6.10(a), increasing I/C significantly reduces the average surface roughness. This trend is observed consistently across different IPA/W ratios. The highest I/C (1.25) shows the lowest surface roughness (0.84 µm for LH and 0.78 μm for HH). At a low I/C (0.25), increasing the IPA/W ratio reduces surface roughness (2.55 μm for LL and 1.92 μm for HL). At the highest I/C (1.25), the influence of IPA/W on roughness is less pronounced, with both LH and HH showing similar low roughness values. The trend is consistent for the root mean square roughness (Rq) as well as shown in Figure 6.10(b).

Additionally, the morphology of the MEA surface is also examined by SEM. The images show an overall reduction in small cracks after the hot press transfer to make the MEA although bigger cracks still remain. The MEA surfaces also appear to be smoother since this is the side originally in contact with the decal substrate.

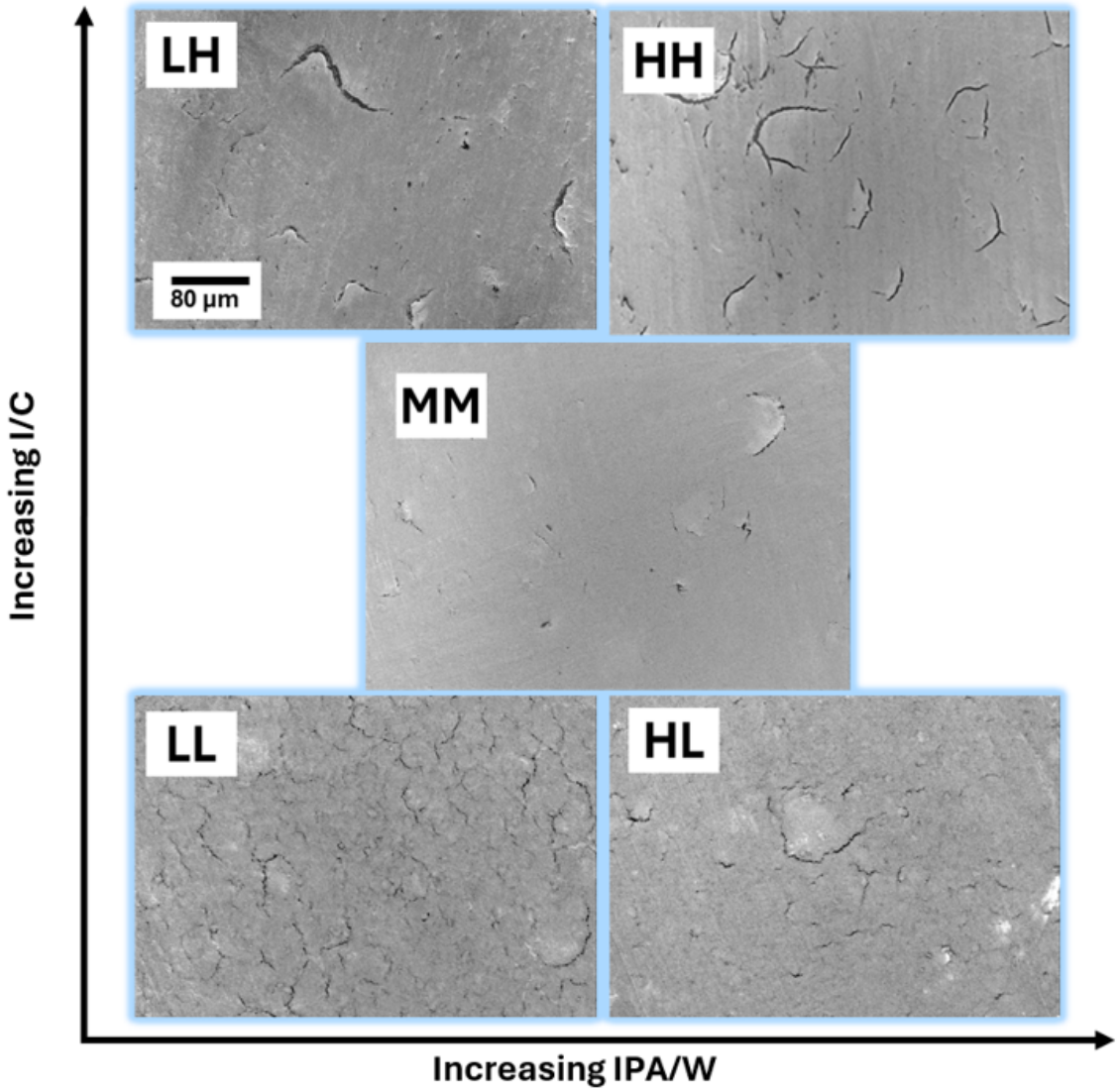

Figure 6.11: SEM images of the cathode side of MEA surface. The scale bar represents 80 μm.

To quantitatively assess the surface roughness of the MEA surface, white light interferometry (WLI) is performed. Unlike the ink-coated PTFE decal surface, the MEA surfaces are sufficiently reflective to allow for accurate WLI measurements. The obtained surface topography images and 3D profiles are presented in Figure B.3. The images are processed using Gwyddion software to obtain the desired surface properties. From the measurements presented in Figure 6.12, it can be seen that MEA surfaces are generally smoother than catalyst ink-coated decal surfaces. Among the samples, MM appears to be the smoothest with the least apparent cracks

as supported by SEM and WLI measurement results.

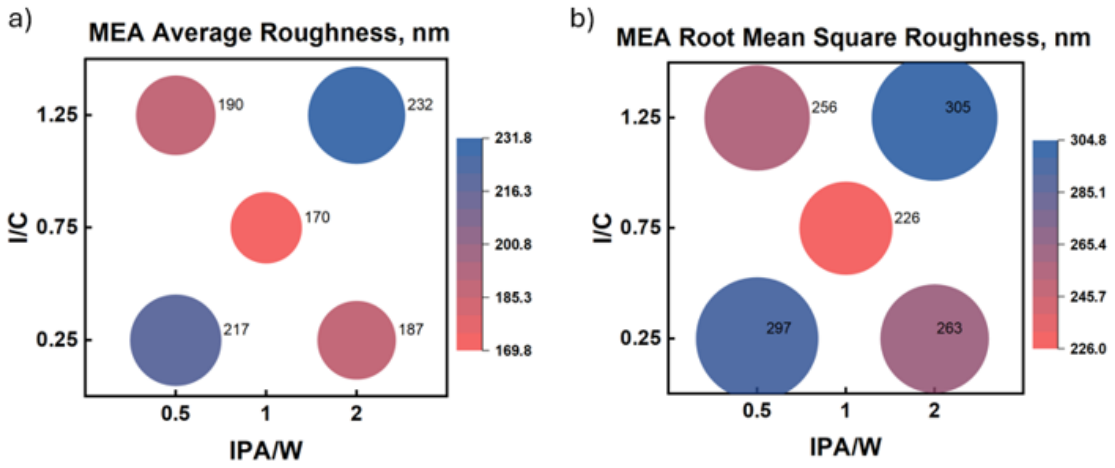

Figure 6.12: (a) Mean surface roughness and (b) root mean square roughness measurements from white light interferometer measurements.

To investigate the catalyst layer microstructure formed from different ink formulations more closely, the pore structure and agglomeration are examined using SEM at 100,000x magnification. The SEM images are presented in Figure 6.13. High I/C samples, LH and HH, show significant ionomer bridging flocculation and patches, denoted by red ovals in the micrographs. These ionomer bridges and patches are significantly less prevalent in the MM sample and are not observed in the LL and HL samples. These ionomer bridges and patches can make the MEA susceptible to flooding, which increases mass transport losses under wet operating conditions. In addition, IPA-rich samples (HL and HH) appear to have a more agglomerated and compact structure compared to their water-rich counterparts. The representative agglomerates from each sample are outlined and indicated with arrows.

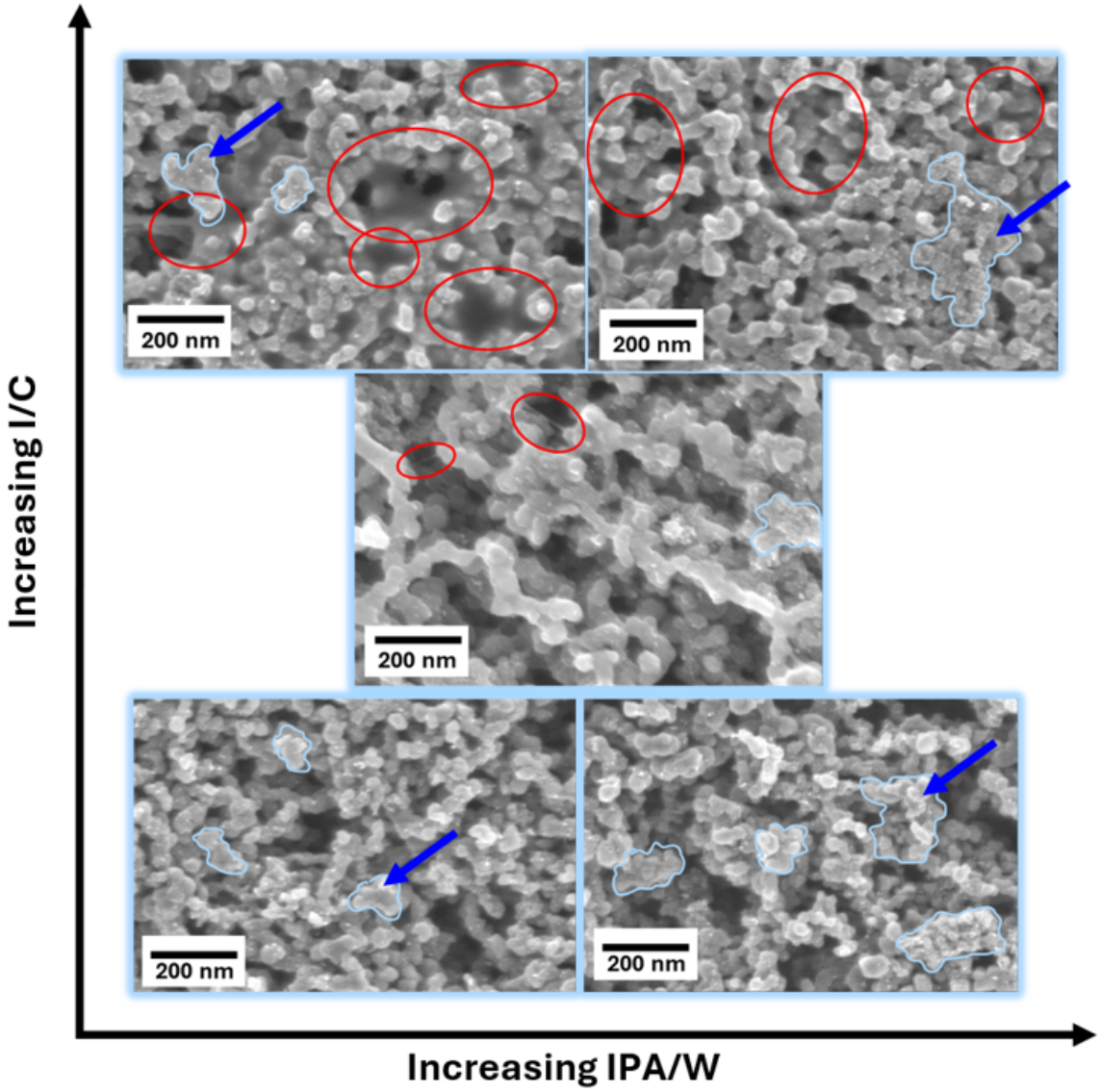

Figure 6.13: SEM images of the cathode side of MEA surface at 100k X magnification. The red ovals highlight the ionomer bridges and patches. The blue arrows point to the representative agglomerate sizes. The scale bar represents 200 nm.

6.2.3 Fuel Cell Performance

In dry conditions, high ionomer loading samples (HH, LH) generally show improved performance compared to lower I/C samples (LL, HL). It is also observed that MM exhibits the best overall performance, with the highest cell voltage and lowest HFR, indicating an optimal balance between ionomer loading and IPA/W

ratio. In general, high ionomer loading contributes to improved conductivity of protons across the catalyst layer thickness. This is especially important in dry conditions, where a severe lack of a proton-conducting network contributes to high ionic losses in the CL.

In wet conditions, MM continues to exhibit the best performance, indicating the robustness of the medium I/C and IPA/W ratio under varying conditions. The performance of low I/C samples (LL and HL) improves under wet conditions and is better than that of high I/C samples. Interestingly, for IPA-rich samples (HH and HL), there is a performance reduction at high current density, indicative of flooding in the CL. This contrasts with the findings from Ref. [127], where no significant link was found between ink solvent composition and cell performance. This signifies that in regions where mass transport loss due to flooding is dominant, the structure of the CL is of utmost importance. From the SEM investigation, we observe that agglomerates are less even and more compact in IPA-rich samples, which hinders the transport of species and can increase mass transport losses.

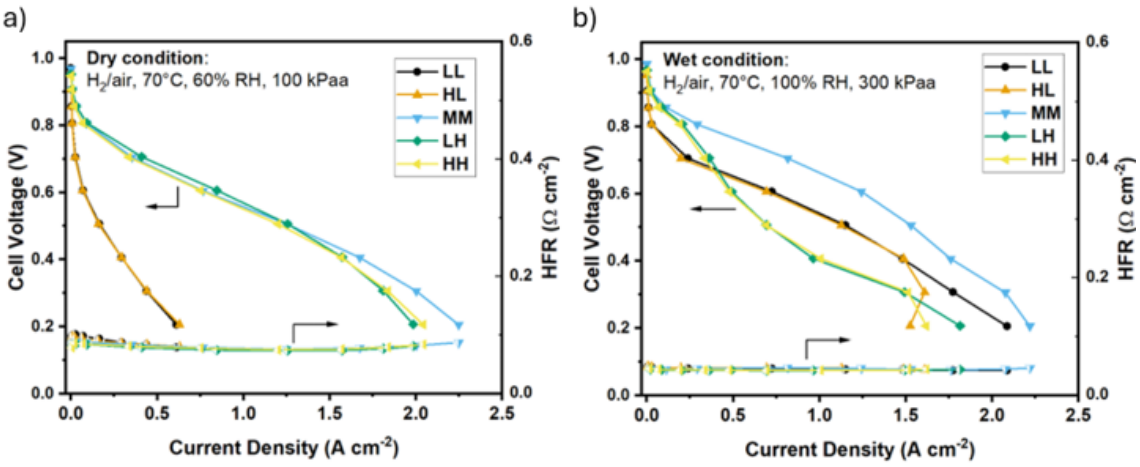

Figure 6.14: (a) Dry polarization and (b) wet polarization curves for all samples

To evaluate oxygen transport resistance within the cell, *in situ* limiting current measurements are conducted. Detailed theory and discussion of the method can be found in Ref. [10, 80, 81]. In the catalyst layer, transport resistance is largely independent of pressure. The mechanisms for mass transport in the catalyst layer include Knudsen diffusion, permeation through a film, and diffusion through the liquid water/ionomer interface [81]. These mechanisms account for the pressure-independent mass transport resistance R_{others}. From Figure 6.15, R_{others} are higher for CL made from low I/C inks. Based on previous discussions about the rheology and internal structure of catalyst inks, low I/C samples exhibit stronger particle network strength and a denser or more highly-entangled microstructure compared

to high I/C samples. These characteristics likely contribute to the resulting catalyst layer microstructure. The MM sample exhibits the minimum R_{others}, which contributes to its overall best performance.

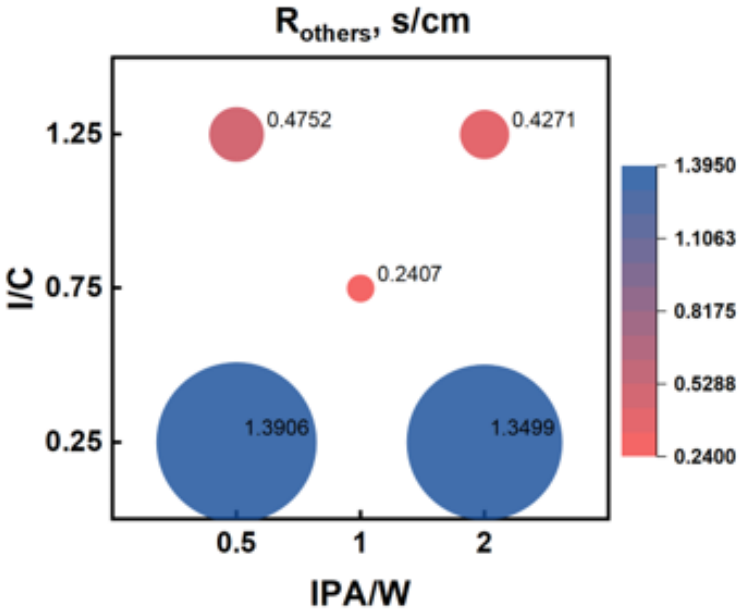

Figure 6.15: Calculated R_{others} based on limiting current test [81] under dry condition.

The proton transport resistance in the catalyst layer is evaluated under different humidification levels. EIS measurements are conducted at fixed intervals to investigate how proton conductivity in the catalyst layer responds to changes in RH. The obtained data is presented in Figure 6.16. The impedance data for the LL and HL samples show high fluctuations and are therefore excluded in the analysis. It is worth noting that the ionic resistance for the low I/C samples (LL and HL) is expected to be high due to the limited ionic pathways. From Figure 6.16, The MM sample has the highest resistance across all relative humidity levels compared to the LH and HH samples, which is understandable due to its lower ionomer content. The LH and HH samples exhibit relatively similar behavior with only a slight increase in resistance under dry conditions. In contrast, the MM sample shows a significant increase in catalyst layer ionic resistance when dry.

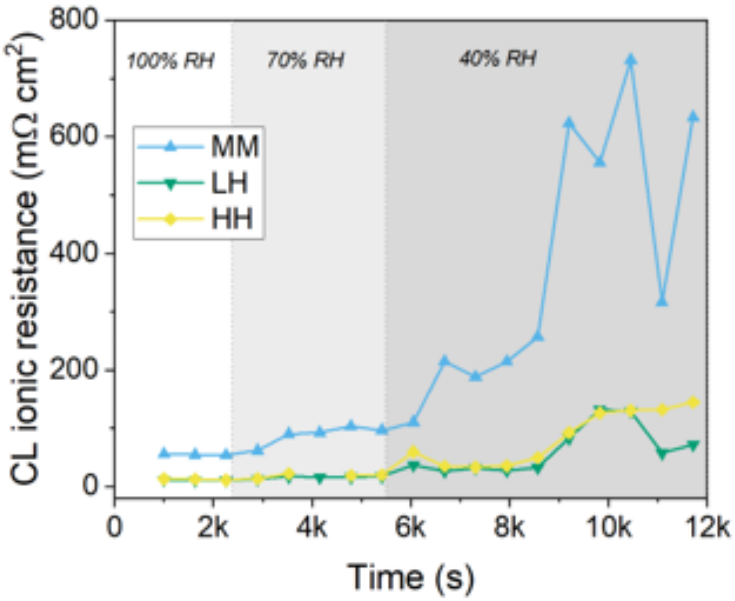

Figure 6.16: Cathode catalyst layer proton resistance measurement across different RH.

6.3 Summary

In this work, a preliminary investigation of the effect of catalyst ink components and processing was conducted. From the results, it was observed that ionomer/catalyst/solvent interaction plays a significant role in the overall properties of the catalyst ink. It was also proven that rheological and electrical responses vary from each catalyst ink formulation tested. Significant differences between electrical and ionic resistance before and after shear can be measured using sequential and simultaneous rheological and impedance measurements. The rheo-EIS tool has been proven to effectively measure the desired properties of materials thereby providing support into the possible microstructure of catalyst ink.

The study explored the impact of ionomer loading (I/C) and solvent formulation (IPA/W) on the CL microstructure and MEA performance. Rheo-EIS measurements revealed that the electrical resistance of ink samples increases with higher ionomer loading and is also influenced by the solvent formulation. In particular, a water-rich solvent helps to open up the ionomer strands, enhancing their surface coverage on Pt/carbon particles and improving the uniformity of the catalyst ink.

The surface morphologies of ink-coated decals and hot-pressed MEA samples were analyzed, revealing that the hot-pressing step effectively mitigates small cracks

and generally results in a smoother surface. However, larger cracks can still persist, potentially affecting the mechanical stability and durability of the MEA.

MEA performance was evaluated under both dry and wet conditions. It was observed that samples with high I/C performed poorly under wet conditions due to excessive swelling, which can lead to flooding and hinder mass transport. Conversely, samples prepared with a water-rich solvent formulation demonstrated improved performance, especially during flooding at high current densities, owing to the formed pore structure of the CL.

These findings underscore the importance of optimizing ionomer loading and solvent composition to achieve a balanced CL microstructure, which is crucial for enhancing MEA performance, particularly in terms of stability and efficiency under varying operational conditions.

Chapter 7

CONCLUSION AND FUTURE WORK

Conclusion for the AEMFC modeling study

The developed one-dimensional (1-D) analytical model for Anion Exchange Membrane Fuel Cells (AEMFC) effectively captures all the essential physics, resulting in model predictions that align well with experimental results. The model's accuracy is particularly sensitive to the material properties, especially the membrane's water transport properties and the diffusion media characteristics. This modeling approach can be adapted for different materials by incorporating a new set of properties, allowing it to effectively address mass transport limitations and overall performance reductions due to flooding in the catalyst layer (CL) and gas diffusion layer (GDL).

The multilayer discretization approach used in the model enables the prediction of local conditions, such as temperature, relative humidity (RH), and concentration, within the CL and GDL. This method is beneficial for semi-empirical modeling of two-phase transport, as it avoids the need for complex phase change and two-phase flow calculations while still providing a reasonable estimate of fuel cell performance.

Furthermore, the sensitivity analyses conducted using the developed 1-D model offer valuable insights into the critical parameters for designing and operating an AEMFC. This model serves as a universal platform and a useful tool for optimizing material properties and fine-tuning operating conditions to achieve robust AEMFC performance. By identifying key factors that influence efficiency and stability, the model aids in advancing the development of more effective and reliable fuel cell technologies.

Conclusion for the catalyst ink study using rheo-EIS measurement

The developed rheo-EIS measurement technique and protocol are invaluable tools for gaining insights into the microstructure and macroproperties of catalyst ink. By enabling the simultaneous measurement of rheological and electrical properties of the catalyst ink slurry, this method allows for the investigation of interactions

between different components of the catalyst ink without relying on complex and costly characterization tools.

Rheo-EIS measurement provides a comprehensive analysis of the catalyst ink by integrating rheological data, which reveals the flow and deformation behavior of the ink, with electrochemical impedance measurements that offer information on its electrical conductivity and charge transfer characteristics. This dual approach, when used alongside other established characterization tools, facilitates a deeper understanding of how the microstructure of the catalyst ink influences catalyst layer performance. By integrating rheo-EIS measurements with established characterization methods such as dynamic light scattering, zeta-potential measurement, profilometry, and SEM, researchers can gain comprehensive insights into the dispersion, particle size distribution, morphology, and interfacial interactions within the ink. These insights are crucial for optimizing the catalyst layer's homogeneity, adhesion, and electrochemical activity, ultimately enhancing the efficiency and durability of fuel cells.

While the parameter space for ink formulation and processing is vast, this dissertation has made significant progress in understanding the impact of ionomer loading and solvent formulation on ink macroproperties, ink structure, CL microstructure, and MEA performance. By systematically investigating these variables, the research provides valuable insights into optimizing the balance between ionomer distribution and solvent composition, which are critical for achieving desired viscosity, stability, and uniformity in the ink. This, in turn, enhances the structural integrity and electrochemical activity of the CL, leading to improved performance of the MEA.

Proposed plan for future study

From Chapter 4.2, carbon supports significantly affect various properties of Pt/C catalyst inks. In particular, the interaction between the ionomer and particles, as measured using the rheo-EIS tool, provides valuable insights into ionomer adsorption on the surfaces of both platinum (Pt) and carbon particles. This adsorption behavior is crucial for understanding how the ionomer facilitates effective proton conduction and catalytic activity. By examining the ionomer-particle interactions, researchers can optimize the ink formulation to ensure uniform and adequate ionomer coverage.

To investigate and deconvolute the interactions of platinum (Pt) and carbon with other catalyst ink components, it is essential to prepare and characterize ink samples containing only carbon supports, such as Vulcan and Ketjen black, instead of Pt/C. These samples should be analyzed using rheo-EIS measurements, following established protocols, in conjunction with traditional characterization techniques.

This approach allows for a focused study of the carbon-ionomer interactions and provides insights into the role of carbon support in influencing the ink's rheological properties and electrochemical behavior.

It will also be of interest to study how Pt loading affects interactions among catalyst ink components. As demonstrated, different carbon supports influence how the ionomer is adsorbed on Pt/C particles, impacting the distribution and accessibility of active sites. Investigating the effects of varying Pt loading can provide valuable insights into optimizing the CL structure. By understanding these interactions, researchers can design a more economical and robust CL that maximizes catalytic efficiency while minimizing the use of costly Pt. This research could lead to improved fuel cell performance and durability, as well as reduced production costs by identifying optimal Pt loading levels that balance performance with material usage.

In terms of modeling efforts, the analytical modeling approach presented in this dissertation can be enhanced by incorporating CL microstructure descriptors such as pore structure, aggregate size, and compactness. Including these descriptors will provide a more comprehensive understanding of how microstructural characteristics influence mass transport and overall performance. This enhanced modeling approach applies to both AEMFC and PEMFC systems, allowing for a more accurate prediction of fuel cell behavior across different technologies. By accounting for these microstructural features, the model can help optimize the design and operation of fuel cells, leading to improved efficiency, durability, and performance.

APPENDIX A
AEMFC MODELING

A.1 Supplementary materials for the AEMFC modeling study

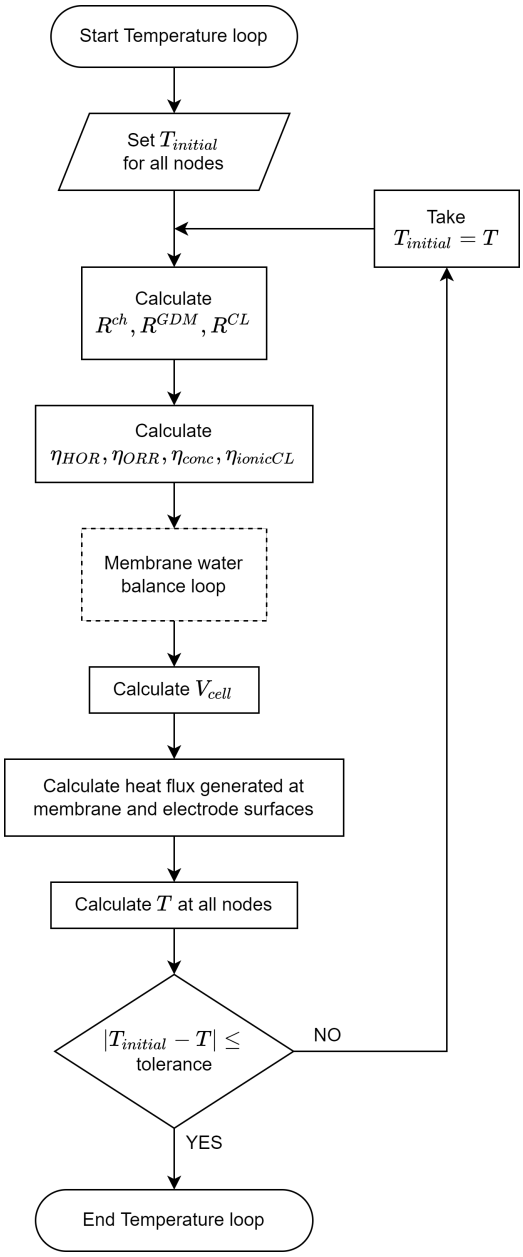

Figure A.1: Temperature distribution calculation algorithm.

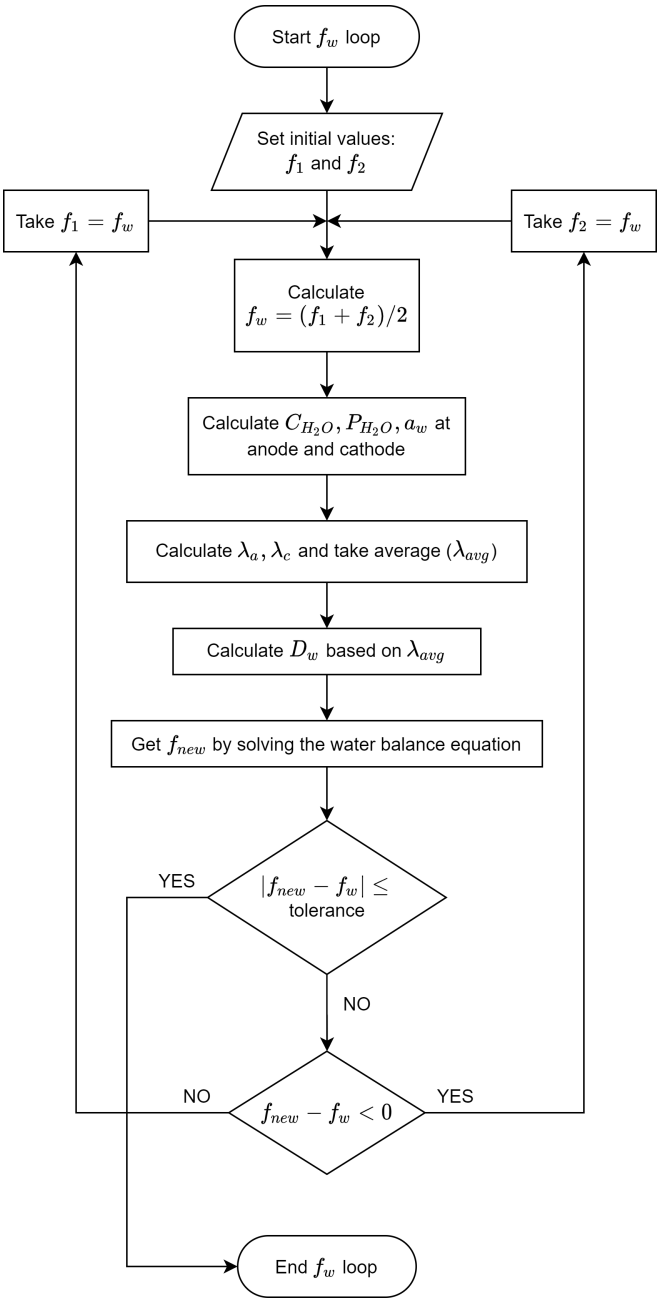

Figure A.2: Water balance calculation algorithm.

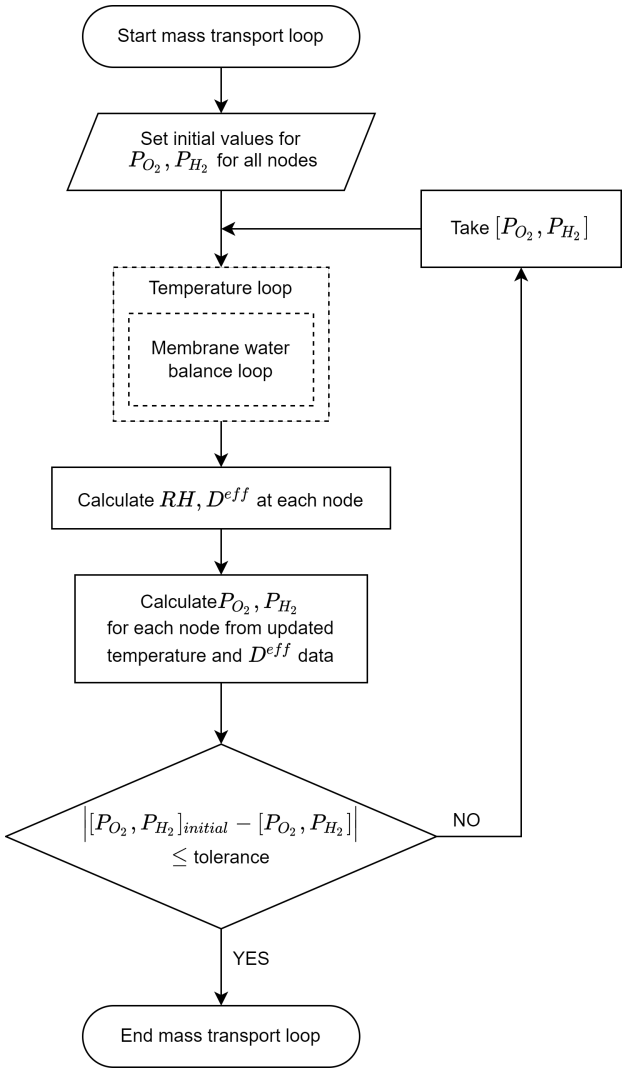

Figure A.3: Mass balance calculation algorithm.

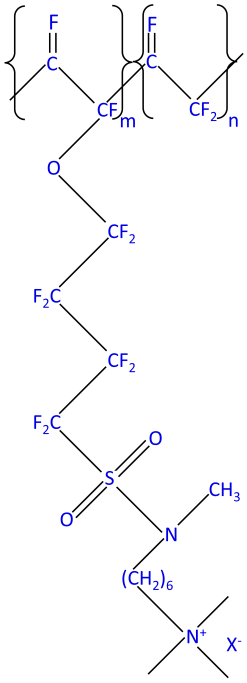

Figure A.4: Gen 2 membrane structure from Divekar et al.
Source: Ref. [91].

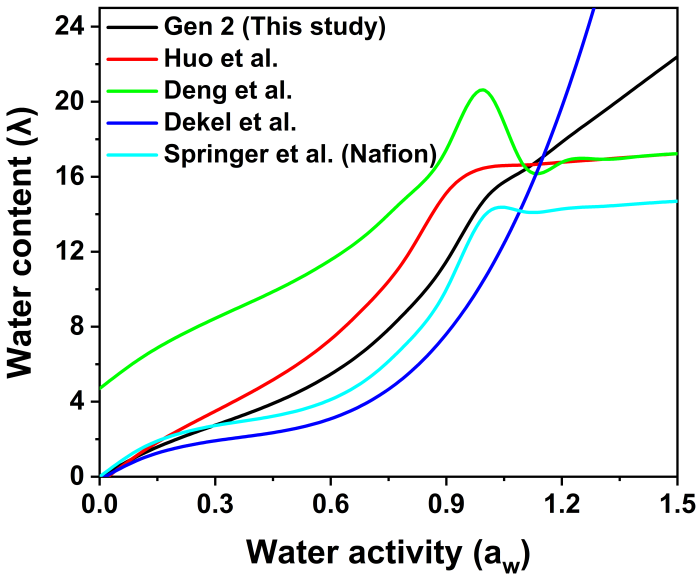

Figure A.5: Water content as a function of water activity for different correlations.

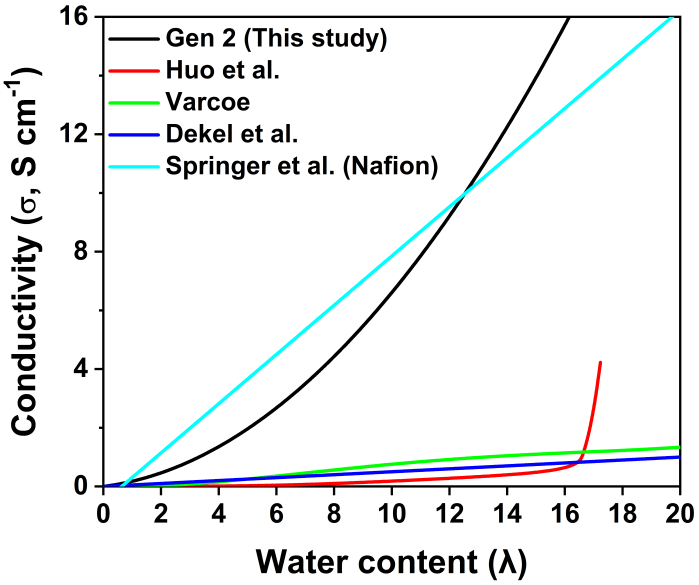

Figure A.6: Membrane conductivity as a function of water content for different correlations.

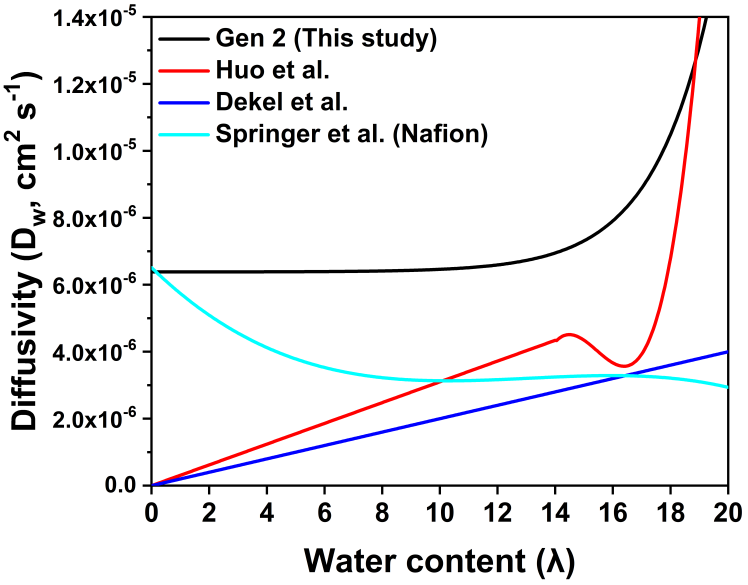

Figure A.7: Membrane water diffusivity as a function of water content for different correlations.

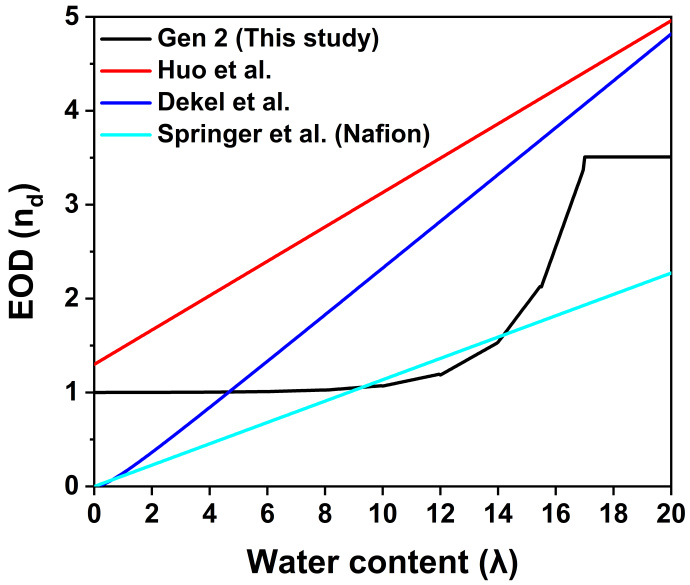

Figure A.8: Electro-osmotic drag coefficient as a function of water content for different correlations.

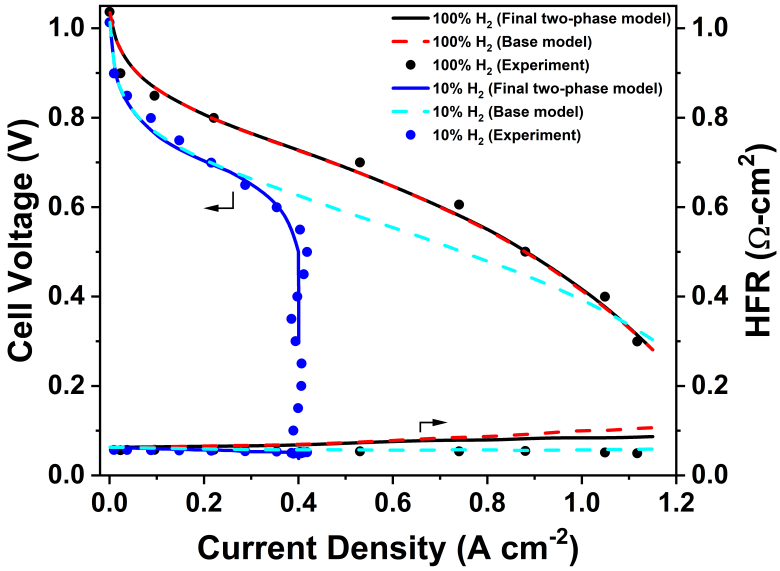

Figure A.9: Performance curve comparison using the Base and Final two-phase models for both 10% and 100% H_2.

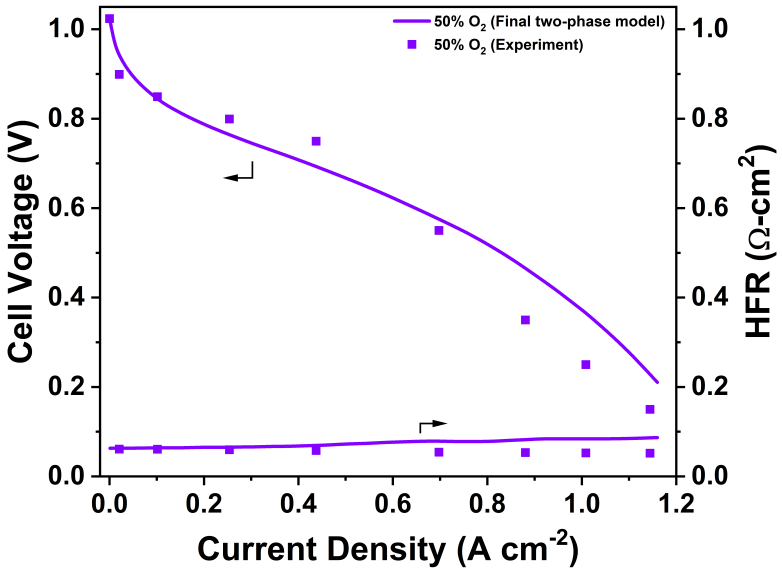

Figure A.10: Comparison of experimental data and simulations results from the final two-phase model for 50% oxygen concentration.

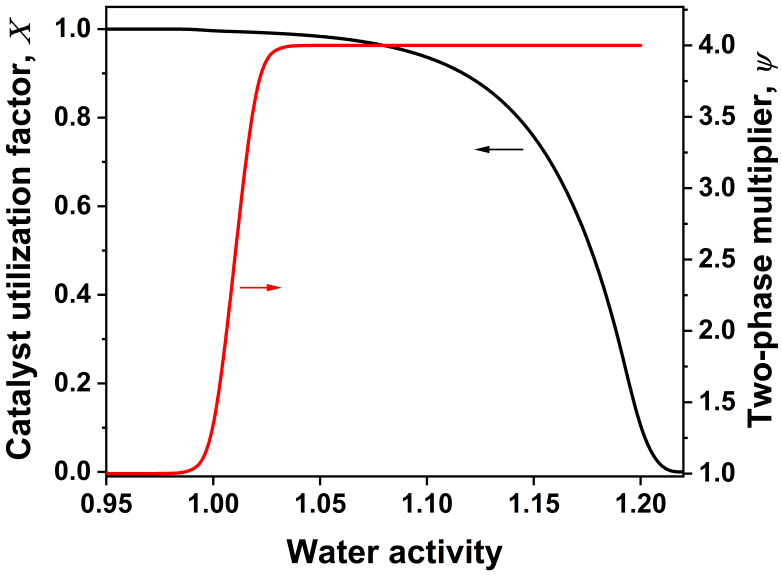

Figure A.11: Multipliers for the catalyst utilization in CL and two-phase condition in GDE as a function of water activity.

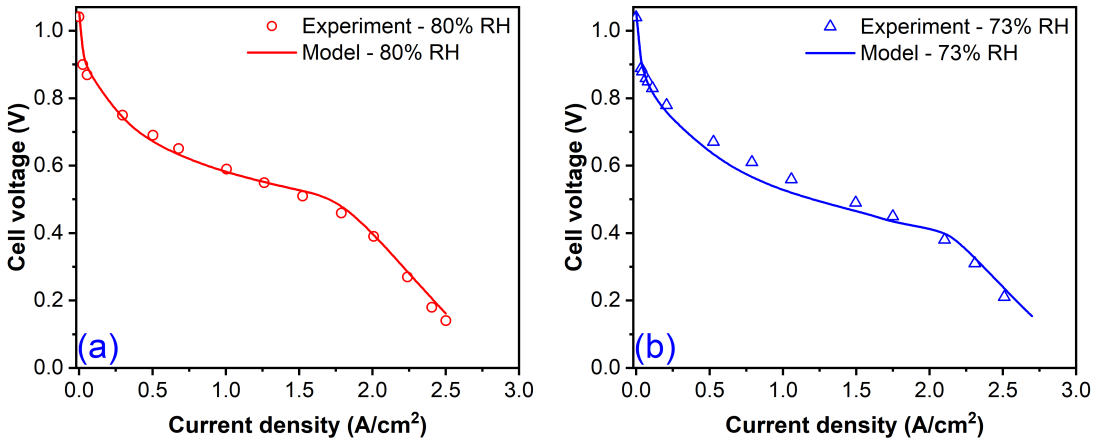

Figure A.12: Comparison of experimental and modeling results for (a) 80% RH and (b) 73% RH at 70°C, 131 kPa, and 100% H_2/100% O_2.

Table A.1: Estimated parameters used in determining catalyst utilization at different inlet RH conditions.

Parameters	Inlet RH		
	92%	80%	73%
K	1.08	1.22	1.14
G	-13.4	-22.2	-17.6
x_m	1.18	1.01	0.96
Wet condition	$a_w \geq 1.0$	$a_w \geq 1.0$	$a_w \geq 0.9$

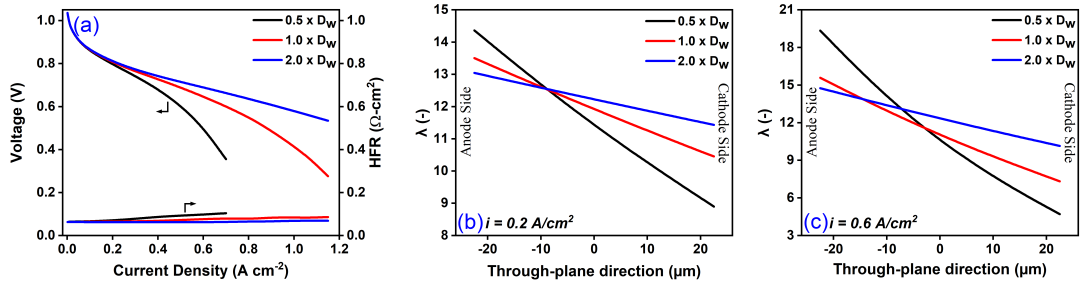

Figure A.13: (a) Cell performance predicted by the final two-phase model of three scale factors for water diffusivity and the calculated membrane water content at a current density of (b) 0.2 A cm^{-2} and (c) 0.6 A cm^{-2}. Cell conditions: 100% H_2/100% O_2, 70°C, 131 kPa, and 92% RH.

APPENDIX B

CATALYST INK STUDY

B.1 Supplementary materials for the catalyst ink-performance study

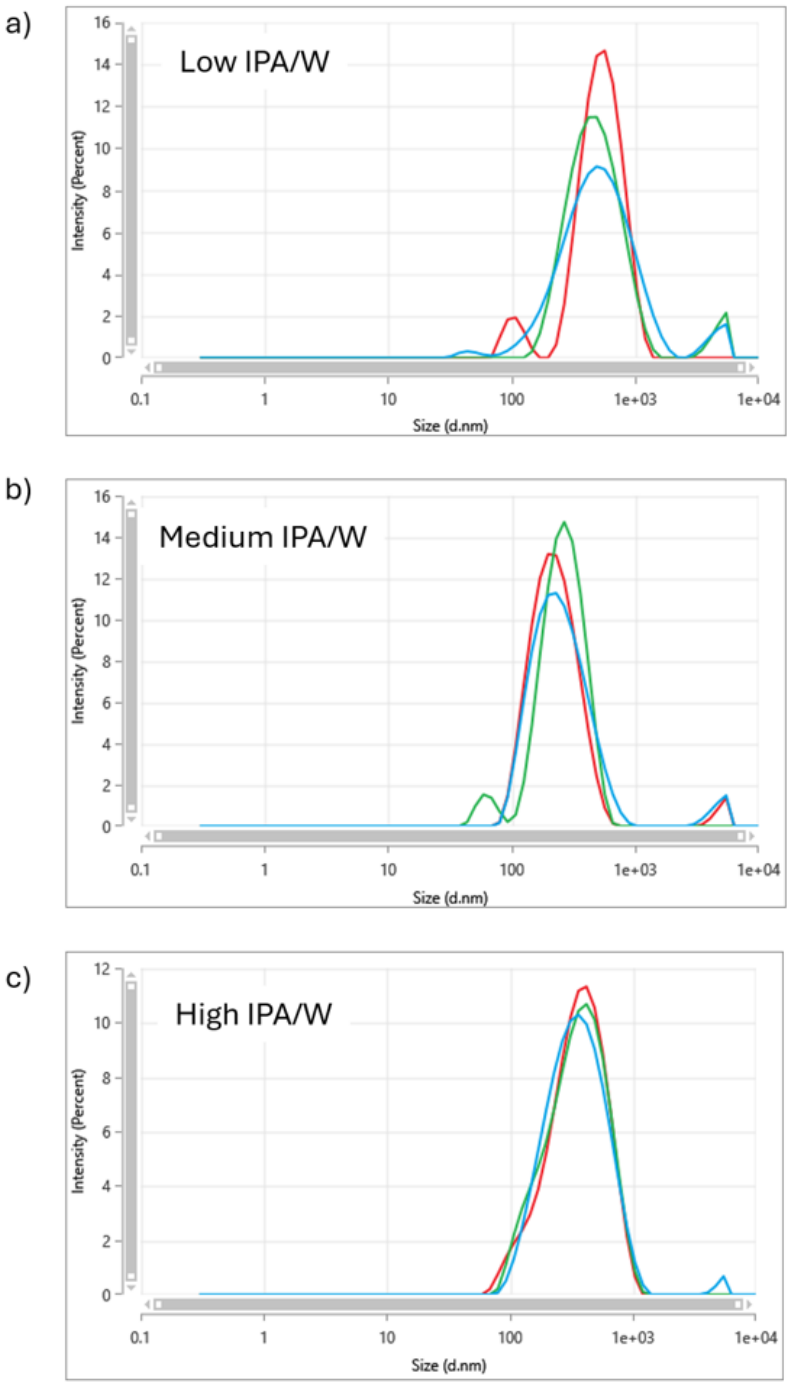

Figure B.1: Particle size distribution for (a) Low, (b) Medium, and (c) High IPA/W samples. Three measurements were conducted.

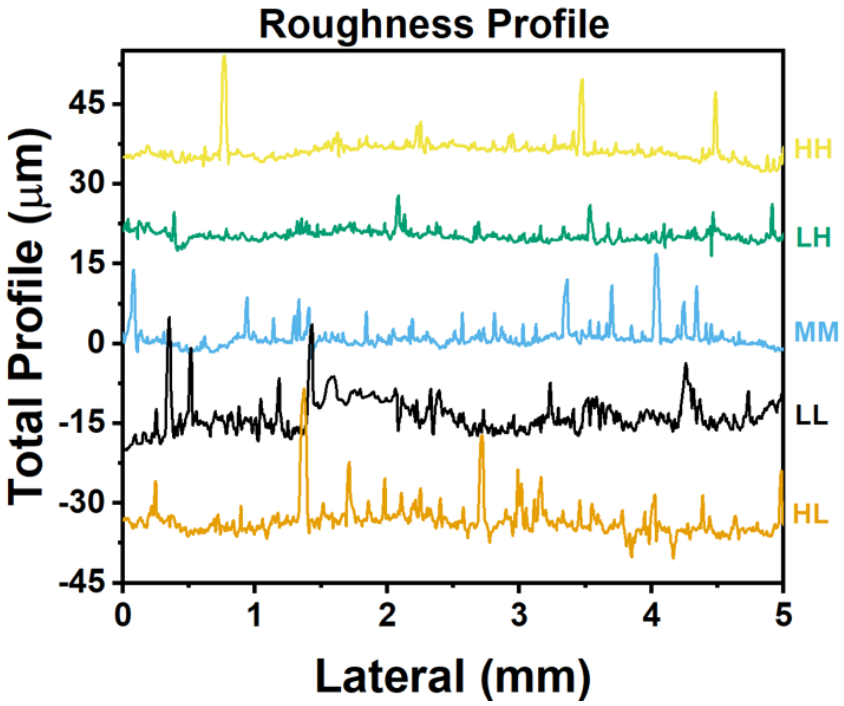

Figure B.2: Roughness profile of catalyst ink-coated PTFE decal samples.

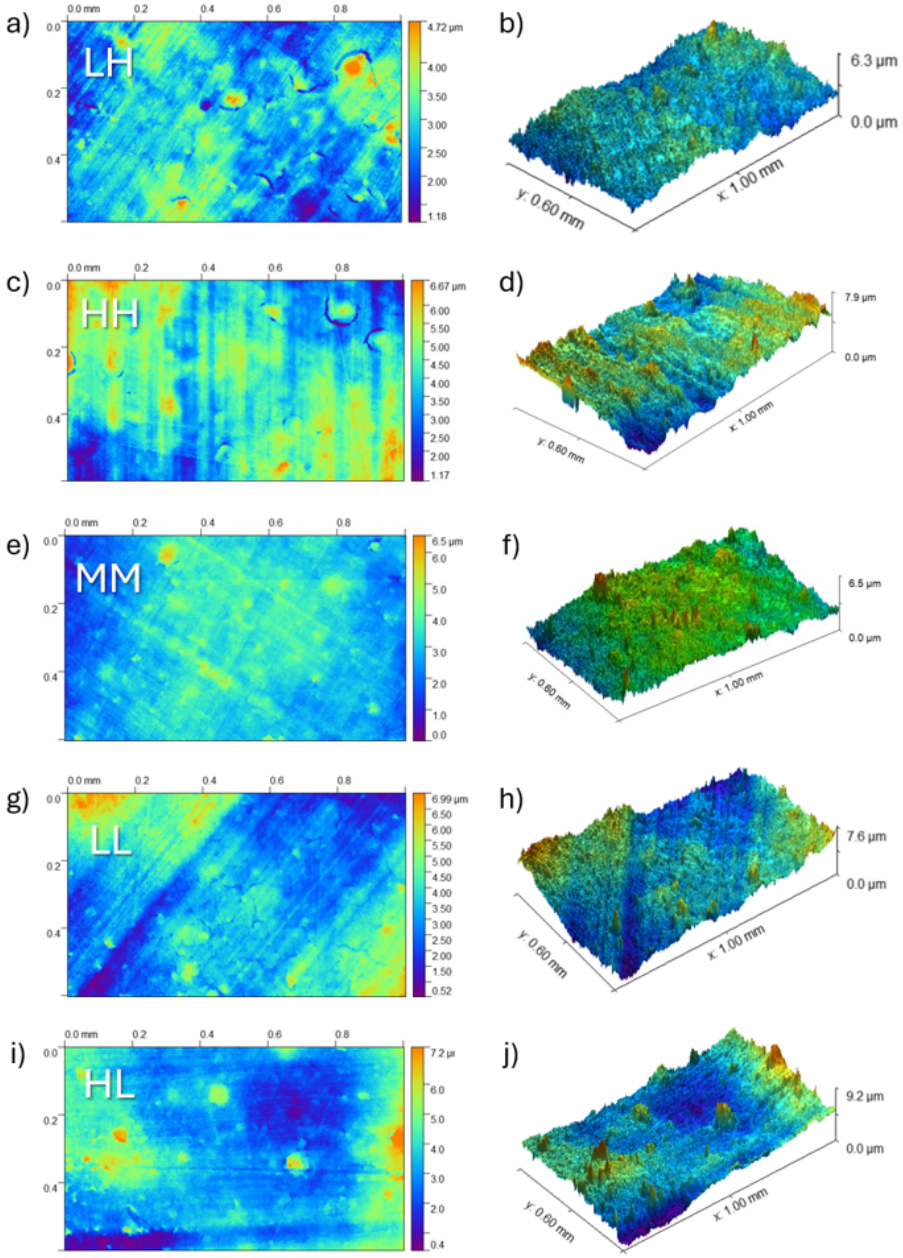

Figure B.3: (a, c, e, g, i) Surface topography and (b, d, f, h, j) 3D image of samples measured using white light interferometry. Images processed using Gwyddion software.

Bibliography

[1] D. Wallace-Wells. "Beyond Catastrophe: A New Climate Reality Is Coming Into View". In: *The New York Times* (2022).

[2] Hannah Ritchie and Pablo Rosado. "Fossil fuels". In: *Our World in Data* (2017). https://ourworldindata.org/fossil-fuels. [Accessed 22-05-2024].

[3] Edward Ring. "How Much Fossil Fuel is Left?" In: *California Policy Center* (2022). https://californiapolicycenter.org/how-much-fossil-fuel-is-left. [Accessed 22-05-2024].

[4] Christian Doh Dinga and Zongguo Wen. "China's green deal: can China's cement industry achieve carbon neutral emissions by 2060?" In: *Renewable and Sustainable Energy Reviews* 155 (2022), p. 111931.

[5] Sarah Wolf et al. "The European Green Deal—more than climate neutrality". In: *Intereconomics* 56 (2021), pp. 99–107.

[6] Emily Cochrane and Lisa Friedman. "What's in the climate, tax, and health-care package". In: *New York Times* (2022).

[7] N. Popovich and B. Plumer. "How the New Climate Bill Would Reduce Emissions". In: *The New York Times* (2022).

[8] Lewis Fulton et al. "California Hydrogen Analysis Project: The Future Role of Hydrogen in a Carbon-Neutral California: Final Synthesis Modeling Report". In: (2023).

[9] Rodney L Borup et al. *M2FCT: million mile fuel cell truck consortium*. Tech. rep. Los Alamos National Lab.(LANL), Los Alamos, NM (United States), 2021.

[10] Felipe Mojica et al. "Study of converging-diverging channel induced convective mass transport in a proton exchange membrane fuel cell". In: *Energy Conversion and Management* 237 (2021), p. 114095.

[11] F Mojica et al. "Experimental study of three channel designs with model comparison in a PEM fuel cell". In: *Fuel Cells* 20.5 (2020), pp. 547–557.

[12] Heng Zhang et al. "Microstructure reconstruction of the gas diffusion layer and analyses of the anisotropic transport properties". In: *Energy Conversion and Management* 241 (2021), p. 114293.

[13] Young-Jun Sohn, Jung-Il CHOI, and Kyoungyoun Kim. "Numerical analysis on water transport in alkaline anion exchange membrane fuel cells". In: *Electrochemistry* 83.2 (2015), pp. 80–83.

[14] Dario R Dekel et al. "Steady state and transient simulation of anion exchange membrane fuel cells". In: *Journal of Power Sources* 375 (2018), pp. 191–204.

[15] Dario R Dekel, Igal G Rasin, and Simon Brandon. "Predicting performance stability of anion exchange membrane fuel cells". In: *Journal of Power Sources* 420 (2019), pp. 118–123.

[16] Travis J Omasta et al. "Beyond catalysis and membranes: visualizing and solving the challenge of electrode water accumulation and flooding in AEMFCs". In: *Energy & Environmental Science* 11.3 (2018), pp. 551–558.

[17] Torsten Berning et al. *Method for optimizing diffusion media with spatially varying mass transport resistance*. US Patent 7,829,230. Nov. 2010.

[18] Md Azimur Rahman et al. "Development of 1-D multiphysics PEMFC model with dry limiting current experimental validation". In: *Electrochimica Acta* 320 (2019), p. 134601.

[19] Joy Marie Mora et al. "Analytical-based simulation approach for an anion exchange membrane fuel cell". In: *Energy Conversion and Management* 273 (2022), p. 116382.

[20] Horie Adabi Firouzjaie and William E Mustain. *Catalytic advantages, challenges, and priorities in alkaline membrane fuel cells*. 2019.

[21] Marc Francis Labata et al. "Insights on platinum-carbon catalyst degradation mechanism for oxygen reduction reaction in acidic and alkaline media". In: *Journal of Power Sources* 487 (2021), p. 229356.

[22] Yiwei Zheng et al. "Quantifying and elucidating the effect of CO 2 on the thermodynamics, kinetics and charge transport of AEMFCs". In: *Energy & Environmental Science* 12.9 (2019), pp. 2806–2819.

[23] Heng Zhang et al. "Coupled stress–strain and transport in proton exchange membrane fuel cell with metallic bipolar plates". In: *Applied Energy* 251 (2019), p. 113316.

[24] H Cruz-Martínez et al. "Current progress of Pt-based ORR electrocatalysts for PEMFCs: An integrated view combining theory and experiment". In: *Materials Today Physics* 19 (2021), p. 100406.

[25] ChungHyuk Lee et al. "Grooved electrodes for high-power-density fuel cells". In: *Nature Energy* 8.7 (2023), pp. 685–694.

[26] ChungHyuk Lee et al. “Effect of Engineered Cracks in Catalyst Layers on PEMFC Catalyst Layer Durability”. In: *Journal of the Electrochemical Society* 171.1 (2024), p. 014502.

[27] André J Spears et al. “Investigation of membrane chemical degradation as a function of catalyst platinum loading”. In: *Journal of the Electrochemical Society* 168.6 (2021), p. 064503.

[28] Leiming Hu et al. “Electrochemical characterization of evolving ionomer/-electrocatalyst interactions throughout accelerated stress tests”. In: *Journal of Power Sources* 556 (2023), p. 232490.

[29] David A Cullen et al. “New roads and challenges for fuel cells in heavy-duty transportation”. In: *Nature energy* 6.5 (2021), pp. 462–474.

[30] Huai-Suen Shiau, Iryna V Zenyuk, and Adam Z Weber. “Elucidating performance limitations in alkaline-exchange-membrane fuel cells”. In: *Journal of The Electrochemical Society* 164.11 (2017), E3583.

[31] Sikan Peng et al. “Numerical and experimental analyses on deviated concentration loss with alkaline anion-exchange membrane fuel cells”. In: *The Journal of Physical Chemistry C* 119.43 (2015), pp. 24276–24281.

[32] Dang Saebea, Chakkrapong Chaiburi, and Suthida Authayanun. “Model based evaluation of alkaline anion exchange membrane fuel cells with water management”. In: *Chemical Engineering Journal* 374 (2019), pp. 721–729.

[33] Jasmin Müller et al. “Practical ex-situ technique to measure the chemical stability of anion-exchange membranes under conditions simulating the fuel cell environment”. In: *ACS Materials Letters* 2.2 (2020), pp. 168–173.

[34] Avital Zhegur et al. “Changes of anion exchange membrane properties during chemical degradation”. In: *ACS Applied Polymer Materials* 2.2 (2020), pp. 360–367.

[35] Pietro Giovanni Santori et al. “High performance FeNC and Mn-oxide/FeNC layers for AEMFC cathodes”. In: *Journal of The Electrochemical Society* 167.13 (2020), p. 134505.

[36] Noor Ul Hassan et al. “Achieving high-performance and 2000 h stability in anion exchange membrane fuel cells by manipulating ionomer properties and electrode optimization”. In: *Advanced Energy Materials* 10.40 (2020), p. 2001986.

[37] Travis J Omasta et al. “Beyond 1.0 W cm^{-2} performance without platinum: The beginning of a new era in anion exchange membrane fuel cells”. In: *Journal of The Electrochemical Society* 165.15 (2018), J3039.

[38] Hao Deng et al. “Effect of electrode design and operating condition on performance of hydrogen alkaline membrane fuel cell”. In: *Applied Energy* 183 (2016), pp. 1272–1278.

[39] Dario R Dekel. “Review of cell performance in anion exchange membrane fuel cells”. In: *Journal of Power Sources* 375 (2018), pp. 158–169.

[40] Sen Huo et al. “Experimental and analytical analysis of polarization and water transport behaviors of hydrogen alkaline membrane fuel cell”. In: *Journal of Power Sources* 382 (2018), pp. 1–12.

[41] Zhiwen Ma et al. “A comprehensive modeling method for proton exchange membrane electrolyzer development”. In: *International Journal of Hydrogen Energy* 46.34 (2021), pp. 17627–17643.

[42] Stefanos Tzelepis et al. “A review study on proton exchange membrane fuel cell electrochemical performance focusing on anode and cathode catalyst layer modelling at macroscopic level”. In: *Renewable and Sustainable Energy Reviews* 151 (2021), p. 111543.

[43] Rambabu Gutru et al. “A comprehensive review on water management strategies and developments in anion exchange membrane fuel cells”. In: *International Journal of Hydrogen Energy* 45.38 (2020), pp. 19642–19663.

[44] Ze Liu et al. “Durability estimation and short-term voltage degradation forecasting of vehicle PEMFC system: Development and evaluation of machine learning models”. In: *Applied Energy* 326 (2022), p. 119975.

[45] Sarah A Berlinger, Samay Garg, and Adam Z Weber. “Multicomponent, multiphase interactions in fuel-cell inks”. In: *Current Opinion in Electrochemistry* 29 (2021), p. 100744.

[46] Raghunandan Sharma and Shuang Ma Andersen. “Zoom in catalyst/ionomer interface in polymer electrolyte membrane fuel cell electrodes: Impact of catalyst/ionomer dispersion media/solvent”. In: *ACS applied materials & interfaces* 10.44 (2018), pp. 38125–38133.

[47] Tim Van Cleve et al. “Dictating Pt-based electrocatalyst performance in polymer electrolyte fuel cells, from formulation to application”. In: *ACS applied materials & interfaces* 11.50 (2019), pp. 46953–46964.

[48] Kui Jiao et al. “Three-dimensional multiphase modeling of alkaline anion exchange membrane fuel cell”. In: *International journal of hydrogen energy* 39.11 (2014), pp. 5981–5995.

[49] Sen Huo et al. “Water management in alkaline anion exchange membrane fuel cell anode”. In: *international journal of hydrogen energy* 37.23 (2012), pp. 18389–18402.

[50] Hao Deng et al. “Transient analysis of alkaline anion exchange membrane fuel cell anode”. In: *International journal of hydrogen energy* 38.15 (2013), pp. 6509–6525.

[51] Huai-Suen Shiau, Iryna V Zenyuk, and Adam Z Weber. “Water management in an alkaline-exchange-membrane fuel cell”. In: *ECS Transactions* 69.17 (2015), p. 985.

[52] Karam Yassin et al. “Elucidating the role of anion-exchange ionomer conductivity within the cathode catalytic layer of anion-exchange membrane fuel cells”. In: *Journal of Power Sources* 524 (2022), p. 231083.

[53] Karam Yassin et al. “The effect of membrane thickness on AEMFC Performance: An integrated theoretical and experimental study”. In: *Energy Conversion and Management* 270 (2022), p. 116203.

[54] Shahrir Abdullah et al. “Electrochemical kinetic and mass transfer model for direct ethanol alkaline fuel cell (DEAFC)”. In: *Journal of Power Sources* 320 (2016), pp. 111–119.

[55] Xiangyu Su et al. “Mathematical modeling of direct formate fuel cells incorporating the effect of ion migration”. In: *International Journal of Heat and Mass Transfer* 164 (2021), p. 120629.

[56] Sen Huo et al. “Analytical modeling of liquid saturation jump effect for hydrogen alkaline anion exchange membrane fuel cell”. In: *International Journal of Heat and Mass Transfer* 112 (2017), pp. 891–902.

[57] Kui Jiao et al. “An analytical model for hydrogen alkaline anion exchange membrane fuel cell”. In: *International Journal of Hydrogen Energy* 40.8 (2015), pp. 3300–3312.

[58] Yuqing Guo et al. “The controllable design of catalyst inks to enhance PEMFC performance: A review”. In: *Electrochemical Energy Reviews* 4 (2021), pp. 67–100.

[59] Qing Gong et al. “Effects of ink formulation on construction of catalyst layers for high-performance polymer electrolyte membrane fuel cells”. In: *ACS applied materials & interfaces* 13.31 (2021), pp. 37004–37013.

[60] Emmanuel Balogun et al. “Catalyst layers for fluorine-free hydrocarbon PEMFCs”. In: *Electrochimica Acta* 401 (2022), p. 139479.

[61] Huiyuan Liu et al. “Effect of catalyst ink and formation process on the multiscale structure of catalyst layers in PEM fuel cells”. In: *Applied Sciences* 12.8 (2022), p. 3776.

[62] Ryosuke Jinnouchi et al. “The role of oxygen-permeable ionomer for polymer electrolyte fuel cells”. In: *Nature communications* 12.1 (2021), p. 4956.

[63] Takeshi Hirai et al. “Effects of Humidity and Produced Water on Specific Adsorption of High Oxygen Permeability Ionomers Composed Entirely of Cyclic Monomers on Cathode Performance for Polymer Electrolyte Fuel Cells”. In: *ACS Applied Energy Materials* 7.9 (2024), pp. 3806–3823.

[64] Xiang Lyu et al. “Design of graded cathode catalyst layers with various ionomers for fuel cell application”. In: *Journal of Power Sources* 556 (2023), p. 232530.

[65] Wataru Yoshimune and Masashi Harada. “Impact of nonadsorbed ionomer on viscosity of catalyst inks for polymer electrolyte fuel cells”. In: *Bulletin of the Chemical Society of Japan* 93.2 (2020), pp. 302–307.

[66] Alin Orfanidi et al. “Ink solvent dependence of the ionomer distribution in the catalyst layer of a PEMFC”. In: *Journal of The Electrochemical Society* 165.14 (2018), F1254–F1263.

[67] Zarina Turtayeva et al. “The Influence of Ink Formulation and Preparation on the Performance of Proton-Exchange Membrane Fuel Cell”. In: *Energies* 16.22 (2023), p. 7519.

[68] Dhinesh Kumar Murugaiah and Samaneh Shahgaldi. “Recent progress in understanding the dispersion stability of catalyst ink for proton exchange membrane fuel cell and water electrolyzer”. In: *International Journal of Hydrogen Energy* 66 (2024), pp. 156–169.

[69] Jozsef Speder, Alessandro Zana, and Matthias Arenz. “The colloidal toolbox approach for fuel cell catalysts: Systematic study of perfluorosulfonate-ionomer impregnation and Pt loading”. In: *Catalysis today* 262 (2016), pp. 82–89.

[70] Donglei Yang et al. “The Formation–Structure–Functionality Relationship of Catalyst Layers in Proton Exchange Membrane Fuel Cells”. In: *Energies* 17.9 (2024), p. 2093.

[71] Sunilkumar Khandavalli et al. “Effect of dispersion medium composition and ionomer concentration on the microstructure and rheology of Fe–N–C platinum group metal-free catalyst inks for polymer electrolyte membrane fuel cells”. In: *Langmuir* 36.41 (2020), pp. 12247–12260.

[72] Sebastian Ott et al. “Ionomer distribution control in porous carbon-supported catalyst layers for high-power and low Pt-loaded proton exchange membrane fuel cells”. In: *Nature materials* 19.1 (2020), pp. 77–85.

[73] Shinichi Takahashi et al. “Analysis of the microstructure formation process and its influence on the performance of polymer electrolyte fuel-cell catalyst layers”. In: *ChemElectroChem* 2.10 (2015), pp. 1560–1567.

[74] Yuqing Guo et al. "Effect of dispersion solvents and ionomers on the rheology of catalyst inks and catalyst layer structure for proton exchange membrane fuel cells". In: *ACS Applied Materials & Interfaces* 13.23 (2021), pp. 27119–27128.

[75] Shirin Mehrazi and Po-Ya Abel Chuang. "Rheological Study of Micro Porous Layer and Its Effect on Transport Properties in a PEMFC". In: *ECS Meeting Abstracts*. 45. IOP Publishing. 2019, p. 2189.

[76] Shirin Mehrazi et al. "A rheological approach to studying process-induced structural evolution of the microporous layer in a proton exchange membrane fuel cell". In: *Electrochimica Acta* 389 (2021), p. 138690.

[77] Aditya Narayanan, Frieder Mugele, and Michael HG Duits. "Mechanical history dependence in carbon black suspensions for flow batteries: A rheo-impedance study". In: *Langmuir* 33.7 (2017), pp. 1629–1638.

[78] Ahmed Helal, Thibaut Divoux, and Gareth H McKinley. "Simultaneous rheo-electric measurements of strongly conductive complex fluids". In: *Physical Review Applied* 6.6 (2016), p. 064004.

[79] W Gu et al. *Handbook of fuel cells*. 2010.

[80] Mrittunjoy Sarker et al. "Experimental and computational study of the microporous layer and hydrophobic treatment in the gas diffusion layer of a proton exchange membrane fuel cell". In: *Journal of Power Sources* 509 (2021), p. 230350.

[81] Daniel R Baker et al. "Measurement of oxygen transport resistance in PEM fuel cells by limiting current methods". In: *Journal of The Electrochemical Society* 156.9 (2009), B991.

[82] Anusorn Kongkanand and Mark F Mathias. "The priority and challenge of high-power performance of low-platinum proton-exchange membrane fuel cells". In: *The journal of physical chemistry letters* 7.7 (2016), pp. 1127–1137.

[83] Po-Ya Abel Chuang et al. "The interactive effect of heat and mass transport on water condensation in the gas diffusion layer of a proton exchange membrane fuel cell". In: *Journal of Power Sources* 480 (2020), p. 229121.

[84] Thomas E Springer, TA Zawodzinski, and Shimshon Gottesfeld. "Polymer electrolyte fuel cell model". In: *Journal of the electrochemical society* 138.8 (1991), p. 2334.

[85] Qiongjuan Duan, Shanhai Ge, and Chao-Yang Wang. "Water uptake, ionic conductivity and swelling properties of anion-exchange membrane". In: *Journal of Power Sources* 243 (2013), pp. 773–778.

[86] KC Neyerlin et al. "Cathode catalyst utilization for the ORR in a PEMFC: Analytical model and experimental validation". In: *Journal of The Electrochemical Society* 154.2 (2007), B279.

[87] Eric L Thompson et al. "PEM fuel cell operation at- 20° C. II. Ice formation dynamics, current distribution, and voltage losses within electrodes". In: *Journal of the Electrochemical Society* 155.9 (2008), B887.

[88] Yuxiu Liu et al. "Proton conduction and oxygen reduction kinetics in PEM fuel cell cathodes: effects of ionomer-to-carbon ratio and relative humidity". In: *Journal of The Electrochemical Society* 156.8 (2009), B970.

[89] YS Li, TS Zhao, and WW Yang. "Measurements of water uptake and transport properties in anion-exchange membranes". In: *International Journal of Hydrogen Energy* 35.11 (2010), pp. 5656–5665.

[90] Andrew Michael Park et al. "Synthesis and characterization of perfluorinated anion exchange membranes". In: *ECS Transactions* 80.8 (2017), p. 957.

[91] Ashutosh G Divekar et al. "The impact of alkyl tri-methyl ammonium side chains on perfluorinated ionic membranes for electrochemical applications". In: *Journal of Polymer Science Part B: Polymer Physics* 57.11 (2019), pp. 700–712.

[92] Hyunchul Ju, Hua Meng, and Chao-Yang Wang. "A single-phase, non-isothermal model for PEM fuel cells". In: *International Journal of Heat and Mass Transfer* 48.7 (2005), pp. 1303–1315.

[93] Ryan O'hayre et al. *Fuel cell fundamentals*. John Wiley & Sons, 2016.

[94] CM Zalitis et al. "Properties of the hydrogen oxidation reaction on Pt/C catalysts at optimised high mass transport conditions and its relevance to the anode reaction in PEFCs and cathode reactions in electrolysers". In: *Electrochimica Acta* 176 (2015), pp. 763–776.

[95] Bilal Abderezzak. *Introduction to transfer phenomena in PEM fuel cells*. Elsevier, 2018.

[96] Manish Khandelwal and MM Mench. "Direct measurement of through-plane thermal conductivity and contact resistance in fuel cell materials". In: *Journal of Power Sources* 161.2 (2006), pp. 1106–1115.

[97] TJ Omasta et al. "Importance of balancing membrane and electrode water in anion exchange membrane fuel cells". In: *Journal of Power Sources* 375 (2018), pp. 205–213.

[98] Md Azimur Rahman et al. "A physics-based 1-D PEMFC model for simulating two-phase water transport in the electrode and gas diffusion media". In: *Applied Energy* 316 (2022), p. 119101.

[99] Jian Zhao et al. “Effect of catalyst deposition on electrode structure, mass transport and performance of polymer electrolyte membrane fuel cells”. In: *Applied Energy* 255 (2019), p. 113802.

[100] Shaojie Du et al. “Effect of Dispersion Method and Catalyst on the Crack Morphology and Performance of Catalyst Layer of PEMFC”. In: *Journal of The Electrochemical Society* 168.11 (2021), p. 114506.

[101] Shaojie Du et al. “Effects of ionomer and dispersion methods on rheological behavior of proton exchange membrane fuel cell catalyst layer ink”. In: *International Journal of Hydrogen Energy* 45.53 (2020), pp. 29430–29441.

[102] Jonghyun Hyun et al. “Tailoring catalyst layer structures for anion exchange membrane fuel cells by controlling the size of ionomer aggreates in dispersion”. In: *Chemical Engineering Journal* 427 (2022), p. 131737.

[103] Björn Eriksson et al. “Understanding the effects of operating conditions on the water management in anion exchange membrane fuel cells”. In: *Journal of Power Sources* 554 (2023), p. 232343.

[104] Saswati Pujari et al. “Shear-induced anisotropy of concentrated multiwalled carbon nanotube suspensions using x-ray scattering”. In: *Journal of Rheology* 55.5 (2011), pp. 1033–1058.

[105] Caidric Indaya Gupit et al. “Nanostructures and viscosities of nafion dispersions in water/ethanol from dilute to concentrated regimes”. In: *Macromolecules* 53.4 (2020), pp. 1464–1473.

[106] Jeffrey J Richards and John K Riley. “Dielectric RheoSANS: A mutual electrical and rheological characterization technique using small-angle neutron scattering”. In: *Current Opinion in Colloid & Interface Science* 42 (2019), pp. 110–120.

[107] Nan Lou et al. “Dielectric relaxation and rheological behavior of supramolecular polymeric liquid”. In: *Macromolecules* 46.8 (2013), pp. 3160–3166.

[108] Shirin Mehrazi et al. “A Rheo-Impedance investigation on the interparticle interactions in the catalyst ink and its impact on electrode network formation in a proton exchange membrane fuel cell”. In: *Applied Energy* 359 (2024), p. 122680.

[109] TA Instruments. In: (). https://www.tainstruments.com/rheo-impedance. [Accessed 22-05-2024].

[110] Jeffrey J Richards, Norman J Wagner, and Paul D Butler. “A strain-controlled RheoSANS instrument for the measurement of the microstructural, electrical, and mechanical properties of soft materials”. In: *Review of Scientific Instruments* 88.10 (2017), p. 105115.

[111] Leonard Jean Moriau et al. “Resolving the nanoparticles’ structure-property relationships at the atomic level: a study of Pt-based electrocatalysts”. In: *IScience* 24.2 (2021).

[112] Yannick Garsany et al. “Dual-layer catalyst layers for increased proton exchange membrane fuel cell performance”. In: *Journal of Power Sources* 514 (2021), p. 230574.

[113] Zheyu Zhang et al. “Cathode Catalyst Layer Design in PEM Water Electrolysis toward Reduced Pt Loading and Hydrogen Crossover”. In: *ACS Applied Materials & Interfaces* 16.18 (2024), pp. 23265–23277.

[114] Mohamed Youssry, Dominique Guyomard, and Bernard Lestriez. “Suspensions of carbon nanofibers in organic medium: Rheo-electrical properties”. In: *Physical Chemistry Chemical Physics* 17.48 (2015), pp. 32316–32327.

[115] Mohamed Youssry et al. “Non-aqueous carbon black suspensions for lithium-based redox flow batteries: rheology and simultaneous rheo-electrical behavior”. In: *Physical Chemistry Chemical Physics* 15.34 (2013), pp. 14476–14486.

[116] Bilen Akuzum et al. “Percolation characteristics of conductive additives for capacitive flowable (semi-solid) electrodes”. In: *ACS applied materials & interfaces* 12.5 (2020), pp. 5866–5875.

[117] Pengcheng Liu et al. “New insights on the agglomeration and sedimentation behaviours of catalyst ink of proton exchange membrane fuel cells affected by ionomers concentration”. In: *Journal of Power Sources* 556 (2023), p. 232427.

[118] Dan Wu et al. “Effect of alcohol content on the ionomer adsorption of polymer electrolyte membrane fuel cell catalysts”. In: *International Journal of Hydrogen Energy* 48.15 (2023), pp. 5915–5928.

[119] Yuqing Guo et al. “Solvent effects on the rheology of fuel cell catalyst ink and the adsorption of ionomers on the particles”. In: *Physics of Fluids* 34.10 (2022).

[120] Makoto Uchida et al. “New preparation method for polymer-electrolyte fuel cells”. In: *Journal of The Electrochemical Society* 142.2 (1995), p. 463.

[121] Chaoqi Han et al. “Solvent Effects on the Catalyst Ink and Layer Microstructure for Anion Exchange Membrane Fuel Cells”. In: *ACS Applied Materials & Interfaces* 16.4 (2024), pp. 4550–4560.

[122] Takahiro Suzuki, Shinya Okada, and Shohji Tsushima. “Characterization of catalyst inks by rheology and microscopic particle properties”. In: *ECS Transactions* 86.13 (2018), p. 193.

[123] Jonathan P Braaten et al. “Integration of a high oxygen permeability ionomer into polymer electrolyte membrane fuel cell cathodes for high efficiency and power density”. In: *Journal of Power Sources* 522 (2022), p. 230821.

[124] Shiqing Liu et al. “Engineering the catalyst layers towards enhanced local oxygen transport of Low-Pt proton exchange membrane fuel cells: Materials, designs, and methods”. In: *International Journal of Hydrogen Energy* 48.11 (2023), pp. 4389–4417.

[125] Sunilkumar Khandavalli et al. “Investigation of the microstructure and rheology of iridium oxide catalyst inks for low-temperature polymer electrolyte membrane water electrolyzers”. In: *ACS applied materials & interfaces* 11.48 (2019), pp. 45068–45079.

[126] Xu Xie et al. “Experimental investigation on the performance and durability of hydrogen AEMFC with electrochemical impedance spectroscopy”. In: *International Journal of Energy Research* 43.14 (2019), pp. 8522–8535.

[127] Masashi Harada et al. “Scattering investigations into the structures of polymer-electrolyte-fuel-cell catalyst layers exhibiting robust performance against varying water fractions of catalyst ink solvents”. In: *Colloids and Surfaces A: Physicochemical and Engineering Aspects* 665 (2023), p. 131183.